THE UNIVERSITY OF READING

Department of Meteorology

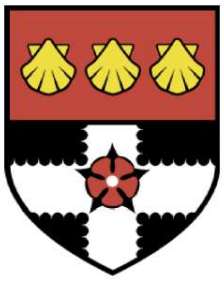

The Dynamic Response of the Global Atmosphere-Vegetation coupled system

John K. Hughes

A thesis submitted for the degree of Doctor of Philosophy

October 2003

’Declaration

I confirm that this is my own work and the use of all material from other sources has been properly and fully acknowledged’

John Hughes

Abstract

Concern about future changes in the carbon cycle have highlighted the importance of a dynamic representation of the carbon cycle in models, yet this has not been fully assessed. In this thesis, we investigate the dynamic carbon cycle model included within the Hadley Centre's model.

In order to understand the behaviour of the vegetation model a simplified model, describing the behaviour of a single plant functional type is derived. The ability of the simplified model to simulate vegetation dynamics is validated against the behaviour of the full complexity model. The dynamical properties of the simplified model are then investigated.

To further investigate the dynamic response of vegetation, a 300 year climate model simulation of terrestrial vegetation re-growth from global desert has been performed. Vegetation is shown to introduce large time lags in land surface properties. This large memory in the terrestrial carbon cycle is an important result for GCM simulations. The large timescale also affects the response of existing vegetation to climatic forcings. The behaviour of the land surface in terms of source-sink transitions of atmospheric CO_2 is discussed. It is found that the transitions between source and sink of CO_2 are dependant on the vegetation timescales.

The response of the atmosphere during the re-growth experiment is then investigated. It is shown that the atmosphere varies substantially in response to the vegetation perturbation. These changes in climate are then shown to alter the re-growth of vegetation. Major impacts are demonstrated for forest regions. Using an offline land surface model it is shown that changes in climatology slow the re-growth of vegetation, resulting in a timescale for recovery that is much longer than expected under a constant climatology. Land-climate feedbacks are sufficient to greatly increase the timescale.

Acknowledgements

Throughout this project I have been helped along by many people. Thanks to Paul and Richard, my supervisors, who have given me their time and their enthusiasm for this field. A special thanks to Julia, who shares my perspective on the world, and who continues to keep me sane. And to Val, David, Helen, and Jen, who have provided a much needed link to reality and support. Thanks also to Ros who supplied cookies and cake thoughout the last year (especially on Saturdays).

The value of having for a time rigorously pursued a rigorous science does not rest especially in its results: for in relation to the sea of worthy knowledge, these will be but a negligable little drop. But it brings forth an increase of energy, of deductive ability, of persistence; one has learned to gain one's purpose purposefully. To this extent, in respect to all one does later, it is very valuable to have once been a scientific man.

– Friedrich Nietzsche, **Human, all too Human.**

Contents

CHAPTER 1

Review of Background Theory

1.1 Introduction

In this chapter theory relevant to this thesis is reviewed. The importance of the global carbon cycle is discussed within a wider climatological context, highlighting the importance of the land surface in the climate. Methods for modelling the global terrestrial carbon cycle are also reviewed, covering ecological and climatological topics. Whilst this thesis does not aim to investigate either paleoclimate or modern climate change, a review of relevant components of both is necessary to understand the terrestrial carbon cycle.

1.2 The Carbon cycle

1.2.1 Carbon Cycle introduction

The carbon cycle is an important part of the climate system. In the atmosphere, carbon in the form of CO_2 alters the radiative budget. Changes in the amount of carbon stored in the terrestrial carbon cycle alters the atmospheric carbon budget, and is related to how much vegetation is available for consumption. The amount of carbon stored in the terrestrial carbon cycle also indirectly influences the physical properties of the land surface as carbon storage implies the presence of vegetation, which alter the land surface properties. Another store of carbon is in the ocean. Some of the carbon in oceans is incorporated into marine plants and forms the primary trophic level in the ocean ecosystem. Figure 1.1 summarises the present-day global scale carbon cycle pools, and the fluxes between them. We depend on the carbon cycle for our environment, food, building materials and fuel. We are even carbon-based ourselves; and to this vast network of interconnections we are making serious changes. Carbon previously stored in the Earth as

coal, oil, and natural gas are being extracted and rapidly injected into the atmosphere. This is pushing atmospheric carbon content to levels higher than at any time in the previous 420,000 years (Petit *et al.* (1999)). Changes to the land surface properties through deforestation and the spread of urban regions also results in the degradation of ecosystems and returns carbon to the atmosphere (*e.g.* Prentice (2001)). We also posses the potential to affect oceanic ecosystems (*e.g.* Boyd *et al.* (2000)).

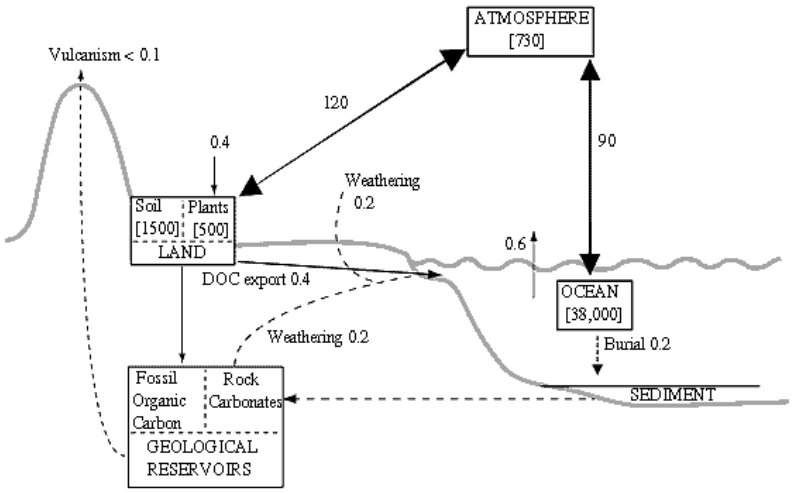

Figure 1.1 *Overview of the natural Carbon cycle. Carbon is stored in the ocean, the land surface and the atmosphere, and is redistributed within the carbon cycle depending on physical processes such as weathering. Carbon is removed from these three carbon pools into geological reservoirs of carbon, and re-enters the carbon cycle through vulcanism and weathering. Reproduced from Prentice (2001). Carbon pool contents are presented in PgC, fluxes are in PgC year^{-1}, and are estimated for 1980.*

Carbon exists in many different forms in the climate system. In the atmosphere carbon dioxide, CO_2, is the most abundant carbon compound. In the oceans carbon exists either as dissolved inorganic carbon, or as part of the ocean biology. In the terrestrial carbon cycle, carbon exists mainly as carbohydrates produced by vegetation, and as carbon stored in the soils. Carbon stored in these three pools makes up the 'fast' carbon cycle. On much longer timescales, vulcanism

increases the amount of carbon and weathering of silicates reduces it. Figure 1.1 shows the amount of carbon stored in the various carbon cycle components. The focus of this thesis is the fast carbon cycle, and from now on we will not explicitly state 'fast'. It is the fast carbon cycle components and its interaction with the rest of the Earth system that will determine the immediate magnitude of future climate change induced by our industrial activities.

1.2.2 Oceanic Carbon cycle

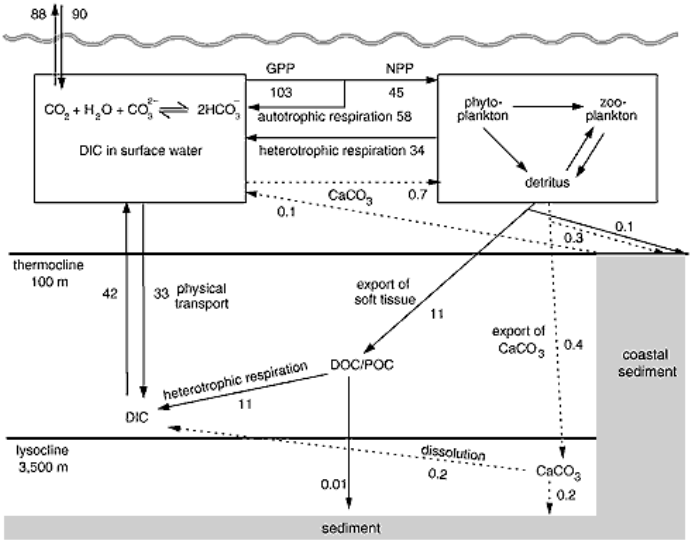

Figure 1.2 *The oceanic carbon cycle. CO_2 is exchanged with the atmosphere. Carbon is exchanged between the inorganic carbon cycle and ocean biology. Carbon is removed from the carbon cycle as sediment formation, though coastal sediments are more dynamic. Reproduced from Prentice (2001). Carbon pool amounts are in PgC, fluxes are in PgC year^{-1}, and are estimated for 1980.*

The ocean holds around 38,000 PgC at present (93 % of the total carbon), much more than either the terrestrial carbon pool (2000 PgC) or the atmosphere (730 PgC), as illustrated in fig. 1.1. The majority of carbon enters the ocean from the atmosphere. CO_2 dissolves more readily

in cold waters. After CO_2 enters the oceans a fraction of it rapidly dissociates to form carbonate (CO_3^{2-}) and bicarbonate (HCO_3^-). These three molecules are the main dissolved inorganic carbon molecules in the ocean (DIC). Only CO_2 is directly exchanged with the atmosphere. DIC is advected around the ocean. The vertical transport of DIC is referred to as the solubility pump. Future changes in ocean circulation could result in changes in the solubility pump. Reactions 1.1 and 1.2 summarise the dissociation process.

$$CO_2 + H_2O \rightleftharpoons H^+ + HCO_3^- \quad (1.1)$$

$$HCO_3^- \rightleftharpoons H^+ + CO_3^{2-} \quad (1.2)$$

Reactions 1.1 and 1.2 are reversible and rapid, so the concentrations of the three carbon molecules quickly form a dynamical equilibrium, *i.e.* the ratio of CO_2 :HCO_3^-:CO_3^{2-} is in equilibrium. The pH of the water is a measure of the concentration of hydrogen ions, which means that the reaction rates of reactions 1.1 and 1.2, and hence the CO_2 :HCO_3^-:CO_3^{2-} ratio is linked to the pH of the sea water. The pH therefore determines what fraction of the total DIC exists as dissolved CO_2, and controls the exchange of CO_2 with the atmosphere.

The vertical profile of DIC is also affected by ocean biology, which accounts for the rest of the vertical gradients in oceanic carbon, and is referred to as the biological pump (*e.g.* Kump *et al.* (1999) p. 136). Plankton is the main component of ocean biology. Plankton is defined as any drifting microscopic organism (*e.g.* Kump *et al.* (1999) pp. 135-136). It is useful to divide plankton into two groups, plants (phytoplankton) and animals (zooplankton). Phytoplankton combine dissolved CO_2 and nutrients through photosynthesis into organic matter. Photosynthesis is light limited and phytoplankton is limited to the upper regions of the ocean where light penetrates (the euphotic zone). Phytoplankton respire carbon, which re-enters the inorganic carbon cycle (*autotrophic respiration*). When phytoplankton die, or defecate they produce particular organic matter (POM) which gradually sinks out of the euphotic zone. In the deep ocean POM is remineralized, re-introducing dissolved CO_2 and nutrients. The liberated CO_2 and nutrients may then be eventually transferred back to the surface. It is by the sinking of POM that CO_2 is moved by the biological pump to lower levels. The other plankton group, zooplankton, graze living phytoplankton, and POM. Zooplankton also produce POM, and respire (*heterotrophic respiration*). The oceanic carbon cycle is illustrated in fig. 1.2.

The oceanic carbon cycle is difficult to measure as the ocean is effectively opaque, and satellite observations are limited to observations of the surface conditions. Satellite observations of the ocean colour can be used to estimate phytoplankton abundance as phytoplankton reflects radiation predominantly at green wavelengths (Sabins (1996)). Observations of sea surface temperature and ocean surface winds may also be used to estimate oceanic circulation (Vonder Haar and Kidder (1995)). Productivity in the euphotic zone may be estimated directly by measuring the amount of POM settling out of the euphotic zone. Matter settling on the ocean floor forms sediment layers. Sediment cores can provide information of previous ocean productivity, and ecosystem composition.

The size of the ocean carbon pool means that any mechanism attempting to explain the glacial-interglacial variations in atmospheric CO_2 must involve changes to the ocean carbon cycle (Archer *et al.* (2000)). One mechanism, the iron hypothesis, is discussed here. The iron hypothesis is included here to give a better understanding of how the ocean carbon cycle could possibly change, but also emphasises the importance of the land surface, and the importance of considering the Earth system as a whole (Ridgwell (2002)).

Martin (1990) hypothesised that additional iron in the surface ocean could enhance phytoplankton activity, causing an increase in the biological pump and a reduction in atmospheric CO_2. The iron hypothesis requires that phytoplankton photosynthesis is primarily limited by iron availability. The iron fertilisation hypothesis is supported by artificial oceanic iron dumping experiments which show a substantial increase in short-term photosynthesis when iron is dumped into the ocean (Boyd *et al.* (2000)). In the natural system iron reaches the surface ocean as mineral aerosol dust transported from the land surface. Ice core records, fig. 1.4, shows that mineral dust is most abundant during peak glacial conditions. Mahowald *et al.* (1999) supports this interpretation with simulations of dust deposition. Harrison *et al.* (2001) discuss the interactions between the dust cycle and climate further. Iron is thought to be especially limiting in the Southern Ocean because of the small fraction of ice-free (dust source) land masses (Martin (1990), Ridgwell (2003)). Watson *et al.* (2000) estimate that this mechanism could have drawn an extra 40 ppmv

into the ocean at the last glacial maximum. The supply of dust to the ocean is dependent on the size of arid regions (sources of dust), and of the strength of transportation of dust (Andersen and Ditlevsen (1998)). Simulations of the extent of arid regions at the last glacial maximum predict expanded arid zones (*e.g.* Mahowald *et al.* (1999)). Terrestrial vegetation is an important factor in the determination of the arid zones (*e.g.* Charney (1975), Braconnot *et al.* (1999)). Ridgwell (2003) emphasises the importance of terrestrial vegetation, and the land surface in general, in the iron hypothesis.

1.2.3 Atmosphere

Figure 1.1 shows that at present the atmosphere contains 2 % of all the carbon in the carbon cycle. In the atmosphere carbon is found largely as CO_2. CO_2 is chemically inert in the atmosphere and changes in the atmospheric CO_2 concentration are the result of changes in the carbon content of terrestrial and oceanic carbon pools. There is a small production term from methane oxidation but this is negligible except at times of 'catastrophic' methane clathrate release (see Nisbet (2002), Kennett *et al.* (2002)). CO_2 is well mixed in the atmosphere so that the concentration at a given time can be approximated by a single value; however seasonal variations of CO_2 in some regions may exhibit intra-annual variability of the order of 15 ppmv, fig. 1.3(a). The current concentration of CO_2 is around 371 ppmv (15 ppmv is 4 % of this value; Prentice (2001)).

The main reason for interest in the carbon cycle is that CO_2 is a greenhouse gas. This means that longwave radiation emitted from the surface of the Earth is absorbed by CO_2, and re-emitted. Some of the re-emitted radiation is directed back towards the Earth, and this additional energy maintains higher surface temperatures than without the greenhouse gas. A simple mathematical description of this process can be found in Hartmann (1994), pp. 26-27. This additional radiative effect is applied uniformly over the surface of the Earth, due to the well mixed nature of CO_2. The additional radiative forcing associated with an increase of CO_2 is not linear, because of the large amounts of CO_2 already in the atmosphere. Several expressions exist which can be used to estimate the additional radiative forcing at the surface associated with an increase in CO_2. The most common form is given by eqn. 1.3. The value of the constant in eqn. 1.3 is the value

presented in Ramaswamy *et al.* (2001).

$$\Delta F = 5.35 ln(C/C_o) \quad (1.3)$$

C is the atmospheric CO_2 concentration (ppmv). C_o is the CO_2 concentration at a reference level. Δ F is the additional radiative forcing (W m^{-2}). ln is the natural logarithm.

The concentration of CO_2 in the atmosphere has been directly observed for several decades (*e.g.* Keeling *et al.* (1995)) and has consistently risen as a result of anthropogenic emissions (Prentice (2001)). Figure 1.3(a) presents the concentration of CO_2 between 1973 and 2002. In 1998 the atmospheric CO_2 concentration was 365 ppmv, an increase of 87 ppmv since 1750 (pre-industrial), resulting in an additional radiative forcing of 1.46 W m^{-2} (Ramaswamy *et al.* (2001)).

The rate of increase in atmospheric CO_2 is not constant. Figure 1.3(b) shows the smoothed rate of change of CO_2 between 1981 and 2001. Analysing the rates of change of CO_2 can help identify important mechanisms for the transfer of CO_2 between the atmosphere and other parts of the Earth system. The causes of the different rates of change of CO_2 vary, but CO_2 rates strongly correlate with the El Niño Southern Oscillation (ENSO ; *e.g.* Keeling *et al.* (1995)). ENSO is a climate oscillation in the tropical pacific, involving ocean and atmosphere processes, and is an important mode of variability of the climate system. ENSO suppresses equatorial upwelling of carbon rich deep water (reducing the outgassing of CO_2), however ENSO is also associated with enhanced tropical land surface temperatures, which increase plant and soil respiration (increasing atmospheric CO_2; Jones *et al.* (2001)). The land surface effect dominates, and CO_2 levels rise. Jones *et al.* (2001) reproduce the ENSO dependency of CO_2 using a coupled climate-carbon cycle model. Volcanic activity can also be an important mechanism in the rate of change of CO_2 (Jones and Cox (2001b)).

There is clear evidence that atmospheric CO_2 has increased because of anthropogenic emissions (Prentice (2001)), but CO_2 has also changed naturally in the past. As CO_2 is chemically inert in the atmosphere these changes imply changes in the other carbon cycle components. Samples of permanent ice contain ancient air, and so provide records of past atmospheric composition

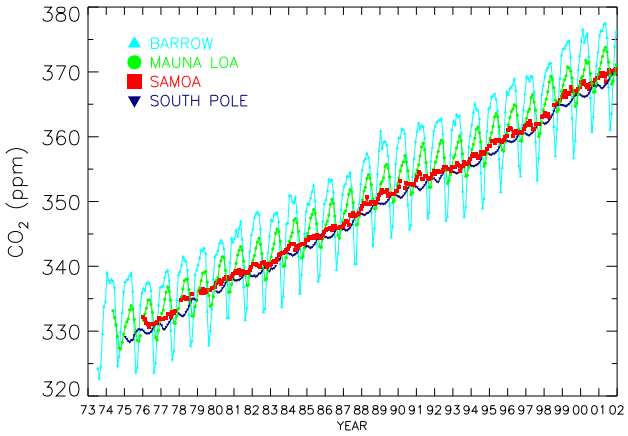

(a) The observed atmospheric CO_2 concentrations.

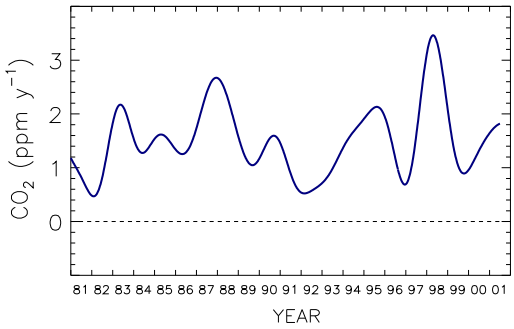

(b) Rate of change of atmospheric CO_2 concentrations.

Figure 1.3 *a) Observed CO_2 concentrations at the 4 NOAA CMDL baseline observatories. b) Smoothed rate of change of global mean atmospheric CO_2 concentrations. Reproduced from the National Oceanic and Atmospheric Administration (NOAA), Climate Monitoring and Diagnostics Laboratory (CMDL), Carbon Cycle Greenhouse Gases Group website: http://www.cmdl.noaa.gov/ccgg on 10/5/2003.*

(Berner *et al.* (1980)). Ice cores can only be obtained from regions of permanently frozen ice, and most ice cores are taken either from Antarctica or Greenland. Past CO_2 levels may also be reconstructed from sources other than ice cores. Fossil stomata can, for example, be used as a proxy for CO_2 levels (Beerling (1999)). Alternative methods of estimating CO_2 levels

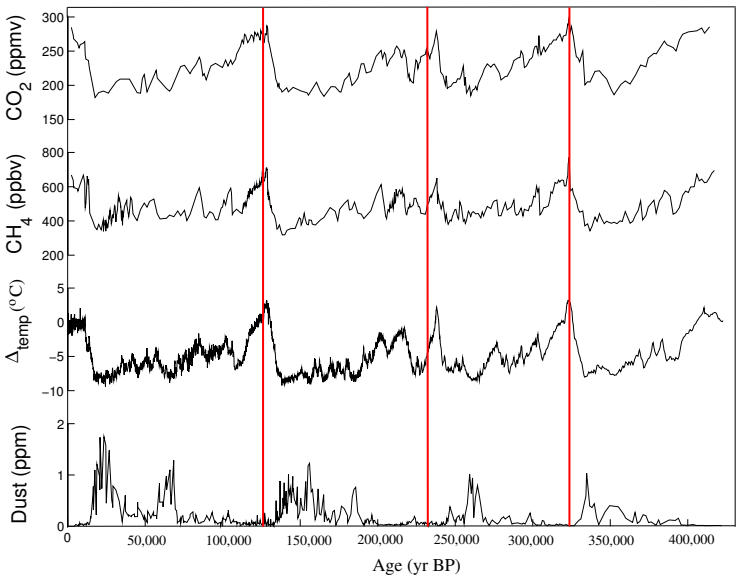

Figure 1.4 *Variations in CO_2, CH_4, temperature, and deposited dust, as reconstructed from the Vostok ice core in Antarctica (Petit* et al. *(1999)). Temperature reconstructions are from oxygen 18 isotope and deuterium records. Interglacial peaks (other than the present interglacial) have been highlighted with vertical red lines. Maximums in CH_4 and CO_2 correspond to maximums in reconstructed temperature (interglacials). Maximums in the deposited dust correspond to periods of glacial maximum. The impact of increased dust deposition is discussed in section 1.2.2.*

provide independent validation of the ice core records. Figure 1.4 shows levels of CO_2, CH_4 , reconstructed air temperature and dust levels over 4 glacial-interglacial cycles (420,000 years) from the Vostok ice core (reproduced from Petit *et al.* (1999)). During the past glacial-interglacial cycles CO_2 variations (fig. 1.4) produced half the changes in radiative forcing (Archer *et al.* (2000)), implying that feedbacks are important and that the glacial cycles are not solely caused by the variability of the solar output referred to as the Milankovitch cycles (see Hartmann (1994), pp. 300-312). Both CO_2 and CH_4 correlate well with the reconstructed temperature records. The challenge of simulating glacial-interglacial cycles in CO_2 is still unsolved and remains a major focus of current research (Archer *et al.* (2000)). Despite the fact that CO_2 levels have fluctuated in the past, fig. 1.4 shows that the current level of CO_2 (365 ppmv) is greater than during the previous 420,000 years. Because CO_2 is chemically inert in the atmosphere the glacial-interglacial cycles in CO_2 imply variations in the oceanic and terrestrial carbon cycle (see

Indermuhle *et al.* (1999)).

1.2.4 Photosynthesis

Photosynthesis forms the main link between the atmospheric and terrestrial carbon cycles, as is illustrated in fig. 1.5. Vegetation photosynthesis draws in CO_2 from the atmosphere, forming carbohydrate and oxygen. Photosynthesis is dependent on the environmental conditions of the leaf, and the availability of raw materials.

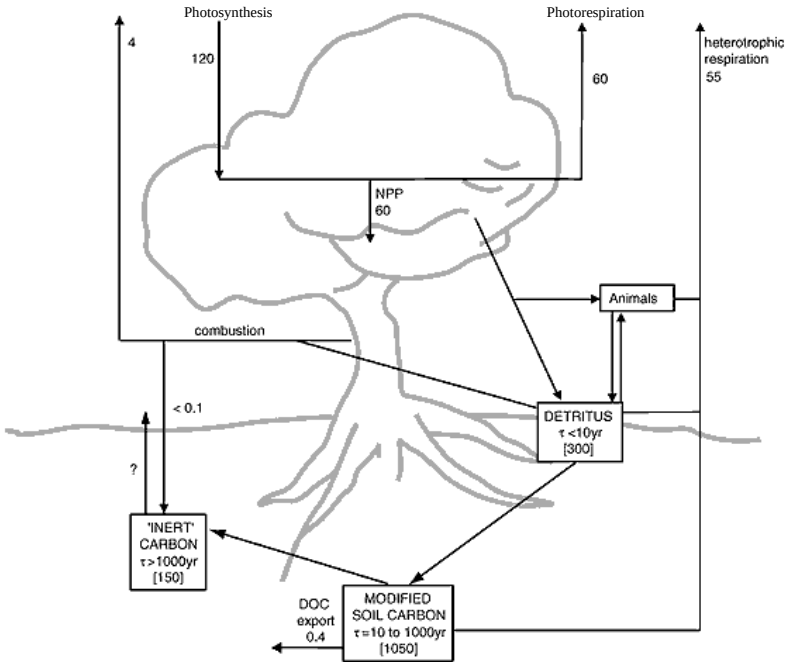

Figure 1.5 *The terrestrial carbon pool. Carbon enters the terrestrial carbon pool through photosynthesis. It is then cycled between vegetation, animals, and the soil. Reproduced from Prentice (2001). Carbon pool amounts are in PgC, fluxes are in PgC year^{-1}, and are estimated for 1980.*

Exchanges between the leaf interior and the atmosphere take place through small openings in the leaf surface called stomata. Figure 1.6(a) is an image of a stomata. Figure 1.6(b) illustrates how

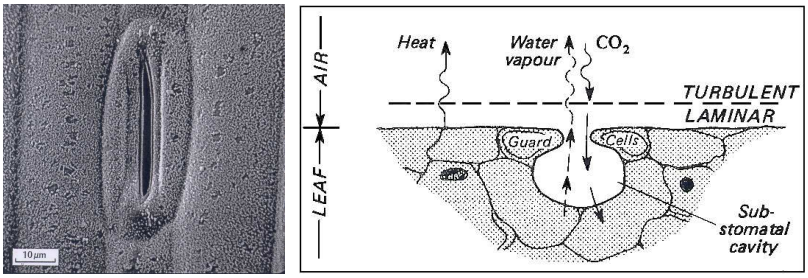

(a) (b)

Figure 1.6 *a) Image of a stomata. The typical dimensions of a stomata are 30μm by 2μm. The width of a particular stomatal opening varies in response to environmental conditions. b) schematic of transfer processes associated with the stomata. Both figures were reproduced from Oke (1987), p. 114.*

moisture and CO_2 are exchanged with the atmosphere. Exchange between leaf and atmosphere is regulated by the guard cells, situated at the neck of the stomatal cavity. The guard cells vary the size of the stomatal opening, which is necessary when soil moisture is limited (in which case the stomatal opening is reduced, limiting the loss of moisture from the plant). The loss of water through stomata establishes a humidity potential difference, drawing water and nutrients into the plant from the surrounding soil. As well as moisture being lost, CO_2 enters through the stomata and so the stomata opening size regulates the amount of CO_2 available for photosynthesis. The transpiration of moisture through the stomata is also an important mechanism for cooling the leaves (Beerling *et al.* (2001)).

The first stage in the photosynthesis reaction is the conversion of CO_2 to carbohydrate. This reaction requires the enzyme Rubisco (RuBP), and the acceptor molecule Ribulose (RuP_2). Rubisco and Ribulose also react with oxygen. One of the eventual products of this second reaction is CO_2 (Mooney and Ehleringer (1997)). The balance between CO_2 removal from the atmosphere (*photosynthesis*) and CO_2 production (*photorespiration*) is dependent on the internal concentrations of oxygen and carbon dioxide. The balance between photosynthesis and photorespiration is defined as the net primary production (NPP), and is the net amount of carbohydrate

produced. In addition to this mechanism (referred to as C3 type photosynthesis) some plants have evolved an additional mechanism involving the enzyme phosphoenolpyruvate carboxylase (PEP). This mechanism increases internal CO_2 concentrations near the RuBP/RuP_2 reaction site, shifting the balance towards photosynthesis rather than photorespiration. Photosynthesis using this additional mechanism is referred to as C4 type photosynthesis. C4 plants are typically grasses or crop plants, such as sugar cane (Krebs (2001) pp. 99-102). The C4 mechanism enables plants to photosynthesise in low atmospheric CO_2 atmospheres, whereas C3 type plants suffer reduced photosynthesis. The C4 mechanism is also important in arid regions, where low moisture availability restricts the stomatal opening. There is evidence that the C4 mechanism has developed several times in the past in response to low atmospheric CO_2 levels (*e.g.* Mooney and Ehleringer (1997) pp. 25-26).

The rate of enzyme activity in both C3 and C4 plants is increased for small increases in temperature, and decreased for cooling, below an optimum temperature. This introduces a temperature dependency into the photosynthesis reaction. Extreme temperatures can also damage plant structure. It has been shown that C3 type photosynthesis is greater than C4 photosynthesis for low temperatures, whilst for high temperatures the reverse is true (*e.g.* Ehleringer and Cerling (2001), Cerling *et al.* (1998)). The exact value of the predicted dominance reversal temperature depends on atmospheric CO_2 concentration (Ehleringer and Cerling (2001), p. 268).

Light is required to overcome the activation energy in the formation of the carbohydrate molecule. Only photons with sufficient energy are able to overcome the activation energy barrier. The fraction of incoming solar radiation which is energetic enough to take part in the photosynthesis reaction (PAR) is around 45 % of the total flux of photons (Monteith and Unsworth (1990), p. 38). At low light levels photosynthesis is limited by the availability of photons (Mooney and Ehleringer (1997), pp. 4-5). Above the 100 W m^{-2} level, leaves are light saturated and are insensitive to further increases. Some of the solar energy used to overcome the activation energy is stored in the carbohydrate molecular bonds (Hall and Rao (1994), pp. 1-2), and this energy supports the global terrestrial ecosystem of herbivores, omnivores, and carnivores.

Nutrients such as nitrogen and phosphorus are important component elements of the Rubisco enzyme. If the supply of nitrogen limits the production of Rubisco then photosynthesis is itself limited. The potential limit of a leaf photosynthesis, V_{max}, is strongly dependent on the leaf nitrogen content (*e.g.* Dickinson *et al.* (2002)). Plant nitrogen content is itself determined by plant-soil interactions that are climate dependent, and the global cycling of nitrogen.

1.2.5 The Terrestrial Carbon cycle

This section discusses the main paths of carbon through the terrestrial carbon cycle after it has been sequestered by photosynthesis. The terrestrial carbon cycle is illustrated by fig. 1.5. After being incorporated into vegetation by photosynthesis, carbon may be released back to the atmosphere by the burning of vegetation. When vegetation dies, or drops leaves, the carbon remains on or in the soil, forming the detritus carbon pool. The detritus carbon pool may release carbon back to the atmosphere if burnt, may be ingested by animals, or broken down by soil microbes. Soil microbes are micro organisms, usually bacteria. When carbon detritus is broken down by soil microbes it forms soil organic carbon, SOC. Carbon in this form either dissolves in soil water, is respired back to the atmosphere, or becomes 'inert' carbon. Inert carbon processes are long term stores of carbon, and are poorly understood (Prentice (2001)). As well as grazing the detritus, animals may also consume living vegetation. When animals die their carbon content enters the carbon cycle by adding to the detritus carbon pool. Animals also respire CO_2 and CH_4 .

The break down of vegetation matter and dead animals by microbes returns vital nutrients to the soil, where they can be re-used by vegetation. Dead leaves, roots, and stem matter are broken down by soil microbe activity. Soil microbes are an integral part of the soil ecosystem and there are many complexities and challenges associated with understanding their behaviour (Killham (1994), pp. 28-31). However it is usually assumed for models of large scale that microbe activity increases with increasing soil temperature and is limited by extreme drought and water logging.

Satellites can provide useful observations of the terrestrial carbon cycle. Vegetation has different

reflective properties than soil and reflects less radiation than dry soil in the infrared band (Sabins (1996)). By comparing land surface reflectance at the red light wavelength and the infrared band, an estimate of vegetation abundance can be made. Estimates of vegetation amounts are given in units of normalised difference vegetation index (NDVI). Empirical relationships can then be used to convert NDVI into leaf area index (LAI) and vegetation carbon content, both of which are usually predicted by global vegetation models. Whilst ice-core records provide a means of reconstructing past atmospheric conditions (Berner (1997)), other components of the carbon cycle must be reconstructed from proxy records. For the terrestrial carbon cycle these proxies include fossil stomata (McElwain (1998)), ancient soils (Berner (1997)), and black carbon (a proxy of fire history, see Schmidt and Noack (2000), Kuhlbusch (1998)).

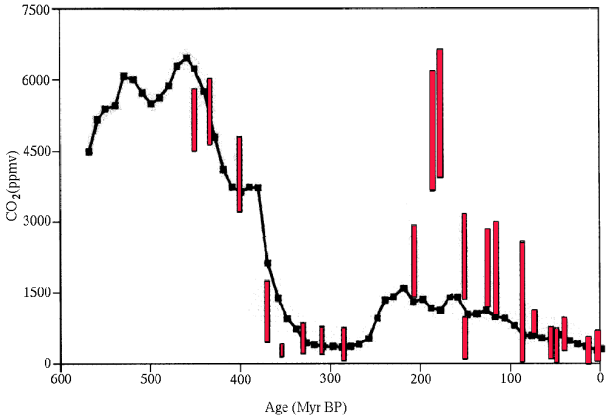

Figure 1.7 *Long term estimates of atmospheric CO_2 derived from geological data. The significant decrease in atmospheric CO_2 after 400 millions of years before present (Myr BP) coincides with the colonisation of land by vascular plants. Red bars represent CO_2 estimates from ancient soils (paleosols). The continuous line is the estimates from a simple model (Berner (1991)). The height of the paleosol estimate bars shows the uncertainty in the reconstructions. Modified from Berner (1997).*

Vegetation is also important on geological timescales. Before plants colonised the land CO_2 was approximately 6000 ppmv. Figure 1.7 shows that as plants colonised the land 400 million years ago the weathering of rocks was enhanced, lowering CO_2 levels (Berner (1997)).

1.3 The simulation of global vegetation

The remainder of this thesis focusses on the terrestrial carbon cycle, and so the rest of this chapter will review this component only.

1.3.1 General Circulation Models

An atmospheric general circulation model (AGCM) is a computer model of the atmosphere designed to predict atmospheric circulation by integrating fluid dynamic equations (McGuffie and Henderson-Sellers (1997)). This allows GCMs to simulate non-linear dynamics and to investigate mechanisms too complex for simpler models or analytical solution. GCMs routinely include radiative and hydrological processes (McGuffie and Henderson-Sellers (1997)).

GCMs are typically run at up to three resolutions. When the GCM is used for global forecasts of synoptic weather systems (1-10 days) the spatial resolution is maximised for this length of simulation given the available computing resources. Longer climatology studies (10-100 years) are more computationally expensive and the GCM is run at a lower resolution. The current Met. Office weather forecast GCM runs at 0.83^o by 0.56^o with 38 vertical levels over the whole surface of the Earth, whilst the climate GCM runs at 3.75^o by 2.50^o, with 19 vertical levels (Gordon *et al.* (2000)). GCMs can also be run for sub-global regions. Reducing the domain size allows the model resolution to be increased. Using this approach the Met. Office regional GCM, HadRM2 is able to simulate climate over the UK at 50 km^2 resolution, with 38 vertical levels (Turnpenny *et al.* (2002)).

As well as simulating atmospheric circulation GCMs are also run with varyingly complex representations of the land surface and oceanic processes. Ocean circulation can be simulated

using similar techniques as for the atmosphere *i.e.* an Ocean GCM (OGCM). The thermodynamic effects of the surface ocean can also be represented in a more simple ocean model, which calculates sea surface temperatures (SSTs) depending on the surface energy balance, prescribed heat convergence, and the large thermal inertia of the mixed layer (McGuffie and Henderson-Sellers (1997)). Atmosphere GCMs may also be run with prescribed SSTs. Initially land surface models calculated the energy balance of the land surface, determining surface fluxes between the land surface and the atmosphere but without coupling the different fluxes (Sellers *et al.* (1997)). Coupling the land surface fluxes became important when more realistic representations of vegetation were included. In the 1980's the importance of CO_2 increases came to prominence and it became necessary to model the effects of CO_2 on the surface energy balance (Sellers *et al.* (1997)). This was achieved by coupling photosynthesis models to the stomatal conductance (Sellers *et al.* (1997)). The importance of stomata on the fluxes of carbon and moisture is described in section 1.2.4. Vegetation structure was initially prescribed. As computer simulations advanced more realistic representations of vegetation were possible. On the global-scale, vegetation distributions are correlated to climate, assuming that vegetation is in equilibrium with the climate. Vegetation models were developed to diagnose vegetation distributions as a function of climate (*e.g.* Holdridge (1947), Prentice *et al.* (1992)). The importance of simulating global vegetation dynamically could then be assessed by performing a series of GCM runs, updating vegetation after each run, providing the land surface parameters for the next run. The validity of this modelling approach relies on how close to equilibrium vegetation is with the atmosphere. Studies such as Cramer *et al.* (2001) show that the terrestrial carbon cycle, and hence vegetation is not in equilibrium with the present day climate as a result of the anthropogenic increase in CO_2. Vegetation models that do not assume vegetation to be in equilibrium with the atmosphere are referred to as dynamic global vegetation models (DGVM). The approaches used by DGVMs are discussed in section 1.3.4.

The spatial resolution of the GCM and the spatial scale of the phenomena being modelled limit the possibility of directly simulating climatic processes. A convective cloud is typically 10 km wide, and is much smaller than the typical resolution of current GCMs, $\sim$100 km, (Gordon *et al.* (2000)). The effects of such sub-grid scale processes may be included into GCM simulation by parameterization schemes (McGuffie and Henderson-Sellers (1997), Schneider (1992)). The

choice of parameterizations in GCMs and other modelling choices means that every GCM is unique. This feature of GCMs means that model investigations must attempt to assess how model-specific a particular modelling result is. Validating the GCM against observations, or against other GCMs can do this. A recent development of GCM based research are experiments performed with a large number of different GCMs. Joussaume *et al.* (1999), for example, simulate changes in the mid-Holocene, north African monsoon using 18 GCMs, whilst the atmospheric model inter-comparison project (AMIP) compared the responses of 32 different GCMs (Gates *et al.* (1999)).

1.3.2 Land surface feedbacks and multiple stable states of the climate system.

The two types of vegetation feedbacks considered here are biophysical and biochemical feedbacks. Biophysical feedbacks involve changes in surface properties, *e.g.* albedo, surface roughness length, or surface hydrology. These changes then alter the atmospheric state, possibly leading to further changes in the land surface properties. Biochemical feedback processes involve changes in the chemical cycles, primarily the carbon cycle. For example, a rise in global temperature could lead to an enhanced emission of CO_2 from soil microbe respiration. The increased CO_2 in the atmosphere would lead to further increased temperatures. Biophysical and biochemical processes are strongly coupled, and analysing the synergism between these two processes is an interesting challenge for future research. The work of Betts (2000), for example, illustrates interactions between biochemical and biophysical processes in the boreal forest region. Betts (2000) show that boreal forests planted to act as a store of atmospheric carbon (the biochemical feedback) would change the surface albedo (the biophysical process), and offset the potential cooling resulting from a reduction in atmospheric CO_2. A study of six DGVMs by Cramer *et al.* (2001) showed that CO_2 levels can alter the response of the biosphere to prescribed physical climate change. Claussen (2001) discusses a method for evaluating synergisms quantitatively, extending the feedback analysis described by Peixoto and Oort (1992), pp. 26-31.

Feedbacks are by definition either positive or negative. Positive feedback processes act to amplify

system changes, whilst negative feedbacks tend to damp out changes in the climate system. The existence of feedbacks within the climate system suggests the possibility that the climate system may exhibit multiple steady states (Royer (2000), Higgins *et al.* (2002)). If there are multiple stable states of the climate system, then there must be basins of attraction in climate space which lead to the different stable states. The term basin of attraction is used here to denote a region of climate space in which the climate system eventually leads to a stable state (either a constant value or a limit cycle). The term climate space is used here to refer to the state of all the different parameters in the climate system. These concepts are features of non-linear dynamical systems. The application of non-linear dynamical system theory to the behaviour of GCMs is discussed more fully by Royer (2000).

Vegetation reacts to an increase in CO_2 by increasing its biomass (*e.g.* Cao and Woodward (1998)). This effect is generally referred to as the CO_2 fertilisation effect. It may also affect the stomatal diameter. Under elevated CO_2 stomata do not need to open as much to get the same amount of CO_2. This is important in the study by Cramer *et al.* (2001). If the increased input of CO_2 into the terrestrial carbon pool is greater than the emission of CO_2 from soil microbe respiration then there is an increased storage of CO_2 in the terrestrial carbon pool (*e.g.* Cox *et al.* (2001)). If the increased storage of CO_2 acts to bring climate closer to the optimum conditions for vegetation photosynthesis then this mechanism is a negative feedback process.

Some model results suggest that as a result of future climate change the biomass of the Amazon forest will be greatly reduced (White *et al.* (1999)). This die-back of the Amazon forest releases carbon back into the atmosphere, and is therefore a positive feedback. The die-back of the Amazon forest also changes the physical properties of the South American land surface, inducing further climate changes. Using a coupled climate model Cox *et al.* (2001) simulate a die-back of the Amazon forest in 2050. The timing of the Amazon die-back is variable, and Jones *et al.* (2003) repeat the simulation of Cox *et al.* (2001), but include sulphate forcings. The effect of sulphate forcings is to delay the Amazon die-back ($\sim$ 10 years), but does not change the final result.

Most GCMs attempts to simulate the mid-Holocene 'greening' of the Sahara under-predict the North African monsoon strength (Joussaume *et al.* (1999)); however Claussen and Gayler (1997), and Claussen *et al.* (2003) are able to simulate the partially vegetated Sahara. Claussen *et al.* (1999) also simulate the rapid desertification of the Sahara observed (Street-Perrott *et al.* (2000), deMenocal *et al.* (2000)), though this study uses the Earth system model of intermediate complexity, CLIMBER2 (Petoukhov *et al.* (2000)). Brovkin *et al.* (1998) investigate the stability of the Saharan system and their analysis suggests that during the Holocene the Saharan system was able to potentially support multiple steady states. Brovkin *et al.* (1998) estimate that approximately 3500 years ago the stability of the Saharan system changed to a single, desert stable state. Claussen *et al.* (1999) suggests that this stability change occurred when summer solar insolation decreased below a threshold value. Renssen *et al.* (2003a) suggests that the stability of the vegetation system was influenced by a decreased intra-annual variability of vegetation fluctuations.

The thermohaline circulation (THC) is the circulation in the oceans driven by temperature and salinity changes on the global scale. A detailed description of the THC is not appropriate here, however it has been hypothesised that the THC may potentially exhibit multiple stable states (Stommel (1961), Manabe and Stouffer (1988)). The THC is important for poleward heat transport, and the effects of a reorganisation of the THC would have an important impact on the Earth system (Stocker *et al.* (2001)). Renssen *et al.* (2003b) show that the effects of a perturbation to the land surface (imposing global desert conditions) could lead to a shut down of the THC (in their model). This coupling of oceanic and terrestrial processes suggests that systems exist which may amplify the behaviour of the terrestrial vegetation and that the dynamic behaviour of the terrestrial vegetation system can be important for simulation of the dynamical behaviour of other systems, as hypothesised by Claussen (2001).

The idea of stabilising vegetation feedbacks in the climate system is illustrated by the conceptual model known as daisyworld. Originally introduced in Watson and Lovelock (1983) daisyworld simulates the competition of two species of vegetation. The two species have different albedoes (0.25, 0.75), and bare soil has an albedo of 0.5. The different vegetation types alter the energy

balance of the environment, altering the global temperature. Vegetation can only exist within the range of 5^{o}C - 40^{o}C in the original paper. The most important feature of the daisyworld model is its ability to alter the climate in a self-regulating way. This behaviour is shown in fig. 1.8. Over a large range of luminosities (65 % - 140 %) global temperatures remain relatively constant, when vegetation is included in the model.

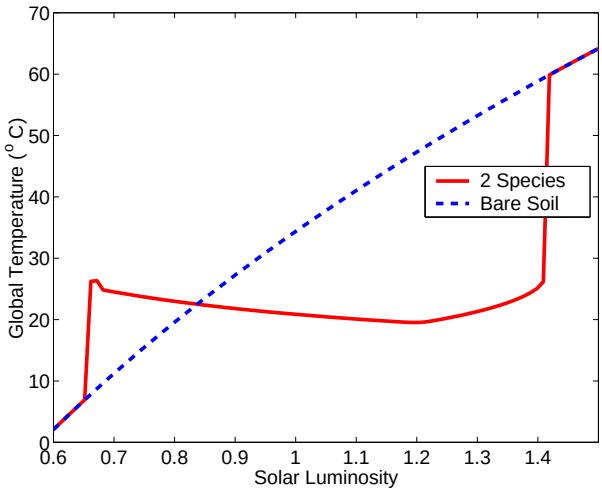

Figure 1.8 *The self-regulating daisyworld behaviour. The two species of vegetation correspond to daisies either darker, or lighter than the underlying bare soil. The solar luminosity constant is a measure of the output of the sun, relative to the present solar output. This plot is reproduced from Watson and Lovelock (1983).*

Since the daisyworld model was first proposed by Watson and Lovelock (1983) the model has been extended to investigate the impact of more realistic ecosystem dynamics (Lenton and Lovelock (2001)). Even with increased model complexity the self-regulating characteristic of the model remains.

The parallels between daisyworld and the real climate system (as represented in GCMs) are discussed by Lenton and Betts (1998); and Betts (1999) demonstrates the self-beneficial behaviour of vegetation in a GCM. The main value of the daisyworld model is not as a predictive tool, but in its relation to the general methodology of Earth system science (Lenton and Wilkinson (2003),

Schellnhuber (1999)).

Investigating the stability behaviour of climate models requires a large number of simulations. For this reason one of the best tools for initial exploration of climate space are Earth system models of intermediate complexity, EMICs (Claussen *et al.* (2002)) and even more simple models (*e.g.* Brovkin *et al.* (1998)). The CLIMBER2 model has been a particularly important EMIC in investigating the stability of the vegetation-atmosphere system, (*e.g.* Brovkin *et al.* (2003), Brovkin *et al.* (1998), Claussen *et al.* (1999)). EMICs use reduced complexity models of components of the Earth system (often the atmosphere), and use the increased speed of integration to perform millennium-scale simulations, investigating the behaviour of a particular climate component. Combining EMICs with full complexity models is an important research technique (Brovkin *et al.* (2003), Claussen *et al.* (2002), Schellnhuber (1999)).

The boreal region is a region of interesting feedback behaviour (*e.g.* Betts (2000)). Forests have a much lower albedo than snow (*e.g.* Oke (1987) p. 12) and snow reflects more incoming solar radiation, maintaining low temperatures that exclude forests. If forests are in place, the lower albedo maintains higher temperatures. The higher temperatures are more conducive to forests growth (Bonan *et al.* (1992), Foley *et al.* (1994)). The boreal forest-snow mechanism is therefore a positive feedback process. Gallimore and Kutzbach (1996) show that the boreal forest-snow mechanism may be important for glacial inception. Brovkin *et al.* (2003) analyse the stability of the boreal regions using a full complexity model, and two Earth system models of intermediate complexity. The models used by Brovkin *et al.* (2003) suggest that the strength of feedbacks in the boreal regions is unable to support multiple stable states.

Biophysical feedback processes are also thought to be important in North Africa (Xue and Shukla (1993)). The Sahara desert dominates North Africa land surface. Saharan desert has high albedo values, relative to the albedoes of vegetation, a difference of about 20 % (Charney (1975)). If vegetation replaces bare soil as the dominant land surface type then more solar energy is absorbed, resulting in a change in the monsoon circulation (which is driven by the difference in temperatures between ocean and continent). This mechanism was first proposed by Charney

(1975), and is investigated further by Charney *et al.* (1975). Vegetation also enhances the recycling of moisture, allowing further transport of moisture into the continent (*e.g.* Braconnot *et al.* (1999), Kutzbach *et al.* (1996), Zheng and Eltahir (1998)). Reconstructions of vegetation distributions suggests that the Sahara was partially vegetated in the mid-Holocene (Jolly *et al.* (1998)). However because the vegetation reconstructions show the vegetation present at the individual sites, continental-scale vegetation coverage cannot be immediately inferred. It is thought that during the mid-Holocene the vegetation coverage changed to a desert state on a timescale of decades to centuries (Street-Perrott *et al.* (2000), deMenocal *et al.* (2000)).

1.3.3 The plant functional type approach

Investigating global vegetation presents a wide choice of temporal and spatial scales. Around 300,000 species of vascular plant (plants with conducting tissue) exist at present (Cox and Moore (1999), p. 12), each with varying physical characteristics, and evolutionary histories. In addition to this diversity, plants interact with other plants, the physical environment, and with animal species creating a daunting network of interactions. One approach adopted by scientists attempting to study vegetation interactions is to categorise vegetation into groups of similar relevant properties, called plant functional types (PFT). The choice of relevant properties varies depending on the phenomena investigated (Gitay and Noble (1997)). The choice of the number of PFT distributions is therefore a trade off between PFT resolution and the range of environmental conditions over which the PFT classification scheme may be applied. The VECODE DGVM for example, categorises terrestrial vegetation into two PFTs, either tree or grass. The TRIFFID DGVM uses five PFT categories: Broad leaf tree, Needle leaf tree, C3 and C4 photosynthesis type grasses, and shrub. Further discussion of the PFT concept and its role in ecology can be found in Woodward and Diament (1991), Woodward and Cramer (1996), or Smith *et al.* (1997).

The PFT resolution is usually low in a DGVM to maintain computational efficiency for global simulations. TRIFFID, and IBIS were designed to simulate vegetation in climate model simulations, and are mainly concerned with correctly predicting land surface properties for the GCMs. In DGVMs the PFT resolution is usually no greater than 9 PFTs (Cramer *et al.* (2001)).

It is assumed that competition dynamics between plants at high PFT resolution does not cause important differences than when low PFT resolution is used. This assumption may be justified by standard ecology theory of competition. This analysis is relatively simple, but is not usually given in textbooks, and therefore is presented here in full. Consider a group of n PFTs, where the ith PFT has a non-dimensional population size X_i. If competition is assumed to take the form of Lotka-Volterra competition equations, the growth rate for PFT i is given by eqn. 1.4.

$$\frac{dX_i}{dt} = X_i(1 - \sum_{j=1}^{j=n} X_j) \tag{1.4}$$

It is assumed here that the intrinsic growth rate, the competition coefficients, and the carrying capacity are equal to 1.0, for simplicity (for further definitions of these terms see Gotelli (1998), pp. 28-33).

The implications of grouping these PFTs together into low resolution PFTs can be assessed by defining two meta-PFTs, Y_1 and Y_2 as shown in eqns. 1.5 and 1.6. The meta-PFTs have been arbitrarily chosen to encompass half the groups of PFTs each, however they could also represent more realistic clusters of PFTs.

$$Y_1 = \sum_{i=1}^{i=\frac{n}{2}} X_i \tag{1.5}$$

$$Y_2 = \sum_{i=\frac{n}{2}+1}^{i=n} X_i \tag{1.6}$$

Then by re-writing eqn. 1.4 in terms of the two meta=PFTs, Y_1 and Y_2, we have:

$$\frac{dY_1}{dt} = Y_1(1 - \sum_{j=1}^{j=2} Y_j) \tag{1.7}$$

$$\frac{dY_2}{dt} = Y_2(1 - \sum_{j=1}^{j=2} Y_j) \tag{1.8}$$

Equations 1.7 and 1.8 are Lotka-Volterra equations for the interaction of the two species. The situation becomes more complex if the assumption of common growth rates and carrying capacities is relaxed, but if only similar plants are grouped together then it may be reasonable to assume that they have similar competition, carrying capacities, and growth rates and the

conclusion is unaltered. This introduces the problem of how to decide an acceptable level of similarity. This analysis suggests that low PFT resolution will not introduce significant errors in simulations of the vegetation dynamics as a result of interspecific competition, especially when Lotka-Volterra equations for competition are used, as is the case in the TRIFFID DGVM.

1.3.4 Existing Dynamic Global Vegetation Models

Relatively few DGVMs exist. The DGVMs discussed here are those investigated by Cramer *et al.* (2001), which are most of the models available at present. The inter-comparison of DGVMs by Cramer *et al.* (2001) provides a valuable means of quantifying differences between models, and also of relating results generated from one model to the group of DGVMs. The six DGVMs considered by Cramer *et al.* (2001) are: TRIFFID (Cox *et al.* (2001)), SDGVM (Woodward *et al.* (1998)), LPJ (Sitch (2000), Sitch *et al.* (2003)), VECODE (Brovkin *et al.* (1998)), HYBRID (Friend *et al.* (1997)), and IBIS (Foley *et al.* (1996), Kucharik *et al.* (2000)).

VECODE is the simplest model, predicting the fractional contributions of grass, tree and bare soil and NPP at a particular grid box using an empirically derived function of precipitation and temperature (Brovkin *et al.* (1998), Lieth (1978)). VECODE was developed for use in the EMIC CLIMBER2 (Petoukhov *et al.* (2000)). In VECODE vegetation structure is updated every year.

LPJ and HYBRID use a “bottom-up” approach to the simulation of vegetation. This method assumes that vegetation on grid box scales exhibit the same dynamics as individual plants (Sitch (2000)). The extent to which ecological processes are scale dependent is a focus of current ecological research (van Gardingen *et al.* (1997)). However it is known that different physical and biological processes influence vegetation structure at different scales (Delcourt *et al.* (1983)). HYBRID simulates individual trees and a layer of grass, competing for light, moisture and nitrogen within a discrete region (Friend *et al.* (1997)). HYBRID is run several times for each grid box, and the runs are combined and scaled up to the grid box scale. In describing HYBRID, Friend *et al.* (1997) state that the optimum number of runs is 10 for each

grid box. Vegetation structure is updated every year. The bottom-up approach is computationally expensive, prohibiting the use of HYBRID interactively in a GCM (Sitch (2000), Cramer *et al.* (2001)). In response to the computational expense of the HYBRID model, the LPJ DGVM simulates plant functional types rather than the individual plants (Sitch (2000)). The PFT population sizes are then used to scale from patch to grid box scale (Sitch (2000)). The LPJ model uses individual based vegetation dynamics theory to simulate changes in the vegetation composition. In LPJ, vegetation competes for light and moisture. Vegetation structure is updated on an annual basis (Sitch *et al.* (2003)).

TRIFFID, SDGVM, and IBIS adopt a "top-down" modelling approach, whereby the land surface properties relevant to GCM simulations (*e.g.* surface albedo, or roughness length) are modelled directly (Cox (2001)). IBIS simulates grid box vegetation in two layers: tree canopy and grass level canopy. Within each canopy PFTs compete for light and moisture. Trees can also act to shade grass, but grass is able to access water as it enters the soil before trees can. Vegetation structure is updated on an annual basis, depending on the annual mean carbon fluxes. Successful PFTs (largest carbon accumulation) crowd out less successful PFTs (Foley *et al.* (1996)). TRIFFID simulates dynamic vegetation structure as the fractional coverage and carbon density of up to 5 PFTs, in the grid box. In TRIFFID PFTs compete horizontally, shrub automatically displaces grasses, and trees displace grass and shrubs. TRIFFID also models competition between grasses and between trees explicitly using Lotka-Volterra competition type equations (*e.g.* Gotelli (1998) p. 101). Using this approach the grass PFT with the larger carbon density will dominate the grass PFT with the lower carbon density. Time averaged carbon fluxes are used by TRIFFID to update vegetation structure every 10 days. SDGVM also predicts ecosystem-scale photosynthesis rates and stomatal conductance, however published literature describing SDGVM is limited, and SDGVM will not be discussed further (two of the most recent papers are Beerling *et al.* (1997), Woodward *et al.* (1998)).

Cramer *et al.* (2001) force the DGVMs with the simulated climate response to estimated anthropogenic emissions between 1850 and 2100, and directly with CO_2 changes. Figure 1.9 shows the globally averaged net primary productivity (NPP) in response to the predicted climate

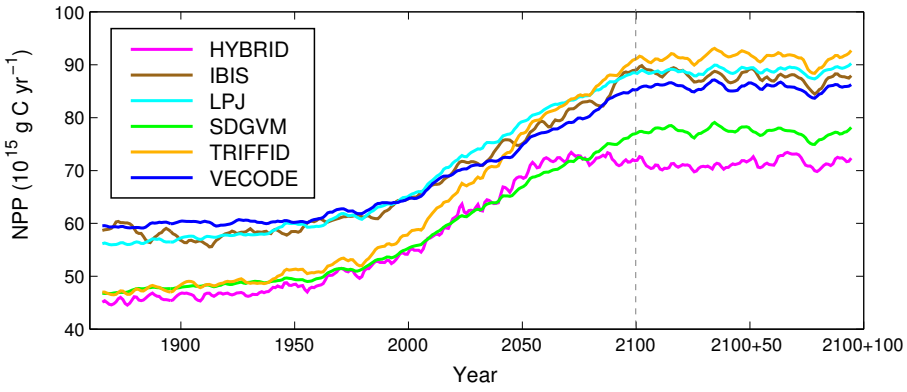

Figure 1.9 *Global averaged NPP predicted by 6 DGVMs. The HadCM2 GCM was forced with estimated CO_2 levels between 1850 and 2100. Until 1990 the CO_2 values are observed concentrations. After this time an increase of 1 % per year is assumed. After 2100 CO_2 was held constant, allowing the HadCM2 to come to equilibrium. The predicted climate from HadCM2 was then used as input datasets to the 6 DGVMs. This figure has been reproduced from Cramer* et al. *(2001).*

change. The increased NPP is mainly a direct response to increased CO_2 rather than the changes in the physical climatology (Cramer *et al.* (2001)). At the start of the simulation shown in fig. 1.9, the predicted NPP is clustered into two groups. HYBRID, TRIFFID, and SDGVM are in the lower cluster, VECODE, LPJ, and IBIS are in the upper cluster. The clustering of predicted NPP does not appear to reflect the modelling approach. As CO_2 increases during the experiment 5 of the DGVMs predicted increase NPP, but remain in the clusters. TRIFFID, however, predicts a greater rate of increase of NPP than the other DGVMs. The effect of TRIFFID's response to elevated CO_2 is to move TRIFFID's NPP from the lower cluster to the top of the upper cluster. This behaviour is illustrated in fig. 1.9. One main feature of TRIFFID which most uniformly differentiates it from the other DGVMs is that TRIFFID uses the Collatz *et al.* (1991) C3 photosynthesis scheme, whilst four of the remaining five DGVMs use the Farquhar *et al.* (1980) scheme. This hypothesis will not be tested more rigourously here. The other DGVM, VECODE, uses an empirical model to predict NPP (Brovkin *et al.* (1997)). The difference in predicted rate of change of CO_2 suggests that TRIFFID is more sensitive to increased CO_2 than other DGVMs.

Cramer *et al.* (2001) also simulate potential vegetation distributions using climate simulated by the HadCM2 GCM. Potential vegetation distributions represent vegetation distributions in the absence of anthropogenic influences, under natural present-day climatic forcings. Analysis of the potential vegetation maps show that different DGVMs predict slightly different vegetation distributions for the same climate. This is seen in a global variability, most importantly in the structure of the forests, and also in the northern extent of the Saharan desert region. However this may also reflect the problems faced in interpolating the different models onto a single set of PFTs.

At the time of the Cramer *et al.* (2001) study TRIFFID and VECODE were the only DGVMs simple enough to be included interactively in a climate model. VECODE was developed for inclusion into an EMIC (Brovkin *et al.* (1997)), whilst TRIFFID has been developed for inclusion into GCMs, and the balance between computational cost and capturing the maximum possible complexity has been chosen to reflect GCM capacities. TRIFFID is the most suitable DGVM to investigate the transient behaviour of global vegetation in the climate system, because of its computational efficiency and the number of studies completed which make use of its surface exchange scheme. The structure of TRIFFID also means that its dynamical properties can be investigated mathematically.

1.4 Aim of this study and plan of the thesis

The aim of this study is to investigate the behaviour of the dynamic vegetation model included into the HadSM3 GCM. Of particular interest is the impact of coupling a dynamic vegetation model interactively to a climate model. There have been several studies testing the modelled surface fluxes, and it is not necessary or possible to repeat this sort of validation here. The ability of the model to simulate vegetation distributions has also been quantified elsewhere. Validating the dynamic behaviour of global vegetation behaviour requires global observations of vegetation properties, over periods of several decades. These data are yet not available, and this study will not attempt to validate the behaviour of the large-scale vegetation dynamics against observations. It will, however investigate the potential importance of vegetation dynamics for the climate

system.

Chapter 2 is mainly a discussion of the GCM used in this study, including a description of some of the validation of this model. Also presented in this chapter is a suite of four GCM experiments investigating and illustrating the sensitivity of the GCM to the carbon cycle and to atmospheric CO_2. These experiments are particularly interesting as they include the die-back of the Amazon forest, a model result of intense scientific, ecological, and political interest.

In chapter 3 a simplified version of the dynamic vegetation model is used to derive key properties of the vegetation model. This model is simple enough for analytical investigation. These results will then be vital in interpreting results during the rest of this study.

The behaviour of the terrestrial vegetation is investigated in chapter 4. This uses the HadSM3 GCM to simulate the recovery of the land surface from initial global desert conditions. This study investigates the length of timescales of the recovery, and the differences between different regions of the land surface.

The experiment discussed in chapter 4 is investigated further in chapter 5. In this chapter the effect of interactions between atmosphere and vegetation on the recovery timescales is examined in more detail. The HadSM3 experiment is investigated further using an offline version of the surface energy scheme.

Finally, chapter 6 summarises the results of the preceding chapters, including some discussion of the conclusions drawn from the results. Some possible avenues for future research are then proposed.

CHAPTER 2

The Hadley Centre Climate Model

2.1 Introduction

In the previous chapter a review was made of climatological theory, focussing on the importance of the land surface, and general techniques used to model the land surface. In order to investigate the interactions between the atmosphere and dynamic global vegetation in GCMs, in this thesis we use the Hadley Centre Climate model, HadSM3. This includes a thermodynamic representation of the mixed layer of the ocean, rather than the fully dynamic ocean more commonly used (HadCM3). Details of HadSM3 will be reviewed, along with a discussion of other versions of the Hadley Centre model, atmosphere only (HadAM3), and fully coupled dynamic ocean and atmosphere (HadCM3). Here HadSM3 includes the MOSES2 land surface exchange scheme. MOSES2 includes the TRIFFID dynamic global vegetation model (DGVM). Existing validation of the model will be referred to, highlighting key features of the model, and illustrating its suitability to investigations of the atmosphere-vegetation system. Four GCM simulations are also presented, investigating the effects of global bare soil conditions, the equilibrium effects of doubling atmospheric CO_2, and the combined effects of both of these perturbations. Although these experiments have been separately performed elsewhere (Betts (1999), Williams *et al.* (2001)), the combination of runs within a single modelling experiment (with all other variables held constant) allows for a new synthesis of results.

2.2 Model physics

2.2.1 Atmosphere

The atmosphere component of HadSM3 is a grid point model, with a 2.5 ^{o} latitude by 3.75 ^{o} longitude grid box resolution. Recent research has highlighted the importance of the horizontal resolution (Pope and Stratton (2002)). Pope and Stratton (2002) investigate how atmosphere behaves as the horizontal resolution is reduced from climate model resolution (2.5 ^{o} latitude by 3.75 ^{o} longitude), to forecast model resolution (0.83 ^{o} latitude by 0.56 ^{o} longitude). Pope and Stratton (2002) show that the climate model predictions do not always converge, due to non-linear hydrological processes and atmosphere dynamics. The implications of this are that the horizontal resolution of a model is a defining characteristic of the GCM. This result also provides motivation for using a group of models run at different resolutions, rather than assuming that results obtained at one resolution is representative of other model resolutions. In the version of HadSM3 used here there are 19 vertical levels, and the model uses a hybrid vertical co-ordinate, combining pressure and height. The atmospheric timestep is 30 minutes (Pope *et al.* (2000)). The model is hydrostatic and uses a Eulerian (standard) advection scheme.

The radiation scheme used in HadUM3 (the generic term used here to refer to the different variants of the GCM, i.e. HadSM3, HadCM3, HadAM3, etc.) is the Edwards and Slingo (1996) scheme. This model is based on the two-stream approximation (scattered radiation is assumed to be transmitted separately from direct radiation). The Edwards and Slingo (1996) scheme has variable spectral resolution and can scale from expensive line-by-line radiation codes to low resolution models, suitable for inclusion into a GCM. The Edwards and Slingo (1996) model has 6 shortwave bands, and 8 longwave bands when included in HadUM3 model (Gordon *et al.* (2000)). The Edwards and Slingo (1996) scheme includes the effects of H_20, CO_2, O_3, N_2O, CH_4, CFC-11, and CFC-12 in the longwave band, and H_2O, CO_2, O_3, and O_2 in the shortwave band. The radiation code is applied every 4 hours. At other atmospheric timesteps the radiative fluxes are applied, but assumed to be equal to the radiative fluxes at the previous radiation timestep. In HadSM3 CO_2 is applied as a uniform concentration and is therefore computationally cheap to model.

In HadUM3 the convection scheme used is a mass flux 'bulk' cloud model. The convection scheme is described in detail by Gregory and Rowntree (1990). Convection is triggered in the model when the vertical thermodynamic profile becomes unstable. The mass flux approach means that the convection scheme explicitly simulates clouds. In the convection scheme clouds are treated as an ensemble of clouds and only the average properties are modelled (the 'bulk' method). Once convection is triggered in the model the air parcel mixes with the overlaying layers as it rises. The maximum height of convection is determined by the the atmospheric temperature profile, and the air parcel properties. In the HadUM3 convection scheme precipitation is triggered when the cloud depth reaches a critical height, or if the cloud temperature of the parcel drops to -10^oC, as long as there is sufficient moisture in the air to enable precipitation.

The closure assumption made to relate convection to the large scale properties relates the energy released to the mass flux at the starting level. This mass flux is then assumed to be a function of the stability of the layer. Convection of air and the mixing of air associated with convection act to alter the thermodynamic, and hydrological atmospheric profiles (which then alter the radiative atmospheric profile). The convection scheme is constrained to conserve the total heat content of the system (enthalpy). The effects of convection on the transport of momentum are also simulated in the model (Gregory *et al.* (1997)).

2.2.2 Ocean

The Hadley Centre climate model can be simulated with three different approaches: prescribing sea surface temperatures (SSTs), HadAM3, a thermodynamic ocean model, HadSM3, and using a fully dynamic ocean model, HadCM3. In this thesis HadSM3 is used, and so the thermodynamic (slab) ocean model will be described in detail. To understand the limitations associated with the slab ocean it will also be necessary to discuss the dynamic ocean model. The slab ocean model used in HadSM3 is described by Williams *et al.* (1999) and the discussion of the slab ocean model included here is based upon this report. The thermodynamic slab ocean

model is referred to as a slab ocean model because it assumes that the ocean can be represented as a single, well mixed slab of water. The slab ocean model runs at the same resolution as the atmospheric component. In the HadSM3 slab ocean the sea surface temperatures are calculated by incorporating prescribed horizontal heat convergences, and the advection of temperatures. Initially the total sea surface radiative fluxes, F_{ao}, are calculated for each oceanic grid box:

$$F_{ao} = (1 - A_{ice})[(SW - BLU) + LW - H + L_c E] + BLU \quad (2.1)$$

BLU is the fraction of the net downward shortwave radiation corresponding to blue light, as the blue light wavelengths penetrate to the greatest depth of sea water (W m^{-2}). SW is the net downward shortwave radiation flux (for all shortwave wavelengths) (W m^{-2}). H is the sensible heat flux (W m^{-2}). L$_c$ is the latent heat of condensation of water at 0^{o}C (2.501$\times$10^6 J kg^{-1}). E is the evaporation flux (kg m^{-2} s^{-1}). LW is the net downward longwave radiation flux (W m^{-2}). A$_{ice}$ is the fractional coverage of sea ice at that particular grid box. Sea surface temperatures are then updated according to the calculated atmosphere-ocean flux of energy:

$$\frac{d(SST)}{dt} = \frac{[F_{ao} - L_f S_n(1 - A_{ice}) - F_{oi}]}{C_p \rho_w Z} \quad (2.2)$$

L$_f$ is the latent heat of fusion at 0^{o}C (0.334$\times$10^6 J kg^{-1}). S$_n$ is the snowfall rate (kg m^{-2} s^{-1}). F$_{oi}$ is the ocean to ice flux of heat, and is proportional to the difference in temperature between the sea ice and the slab ocean temperature. A timestep of 1 day is used here. ρ_w is the density of water (kg m^{-3}). C$_p$ is the specific heat capacity of water (the product C$_p$ $\cdot$ ρ_w = 4.04$\times$10^6 J K^{-1} m^{-2}). Z is the depth of the mixed layer (m), and is assumed to be 50 m. The choice of parameters used here are those used by Williams *et al.* (1999).

After the SSTs are updated according to the local energy budget they are advected using surface currents assuming continuity of sea water (surface currents are prescribed in HadSM3). Advection redistributes temperature horizontally but the application of the continuity assumption to the horizontal currents means that the vertical water velocities are estimated (the magnitude of upwelling and downwelling). When the horizontal currents produce local upwelling the model assumes that the upwelling water has the same temperature as the zonal mean slab ocean temperature. The SSTs are then calculated as a function of prescribed heat convergences, H$_C$.

$$\frac{d(SST)}{dt} = \frac{H_C}{\rho_w C_p Z} \tag{2.3}$$

The heat convergences are prescribed. The prescribed heat convergences vary throughout the year and H_C is generally positive in the winter hemisphere (300 W m^{-2}) and negative in the summer hemisphere (-200 W m^{-2}). These heat convergences are interactively adjusted to compensate for varying grid box size (a function of latitude) and the effects of sea ice.

Sea ice is dynamically simulated in HadSM3. The sea ice model is an important model in climate processes. Sea ice can rapidly alter the sea surface properties, and act as a positive feedback mechanism, cooling sea temperatures further (Gordon *et al.* (2000)). In eqns. 2.1, 2.2, and 2.3 sea ice directly effects the simulation of SSTs (in eqn. 2.3 sea ice affects the heat convergence). Sea ice is simulated in terms of fractional coverage and sea ice depth (over the fraction of the grid box covered by sea ice). Cattle and Crossley (1995) describe the dynamic sea ice included in HadSM3. Sea ice is advected in the model according to the surface currents, which are prescribed. New ice forms when the SST at a grid box falls below the freezing temperature. For each sea ice covered grid box, snow can accumulate on it. Snow depth is updated as the balance between snowfall and sublimation. It is also updated as snow melts. Below the snow layer the ice thickness is updated as a function of melting snow, sea surface temperatures, and a fraction of the atmospheric flux, F_{ao}, which is estimated using eqn. 2.1. Melting sea ice also alters the sea surface temperature. Changes to the fractional coverage of sea ice are caused by changes in the ice thickness.

In HadCM3 the dynamics of the ocean circulation are explicitly simulated. The dynamic ocean model runs at 1.25^o latitude by 1.25^o longitude resolution, with 20 vertical levels. The dynamic ocean model is based on the model presented in Cox (1984). The dynamic ocean model incorporates the same sea ice model as the slab ocean model. Due to the model developments (mainly the high resolution) the dynamic ocean model is run without imposed corrections to the air-sea fluxes (flux adjustments). The transfer of heat and salinity by ocean geostrophic eddies are parameterized using the method presented in Visbeck *et al.* (1997). Visbeck *et al.* (1997) relate the diffusion constant, k, to the horizontal and vertical thermal stratification, and the eddy

flux of heat is assumed to be proportional to the temperature gradient. A low resolution version of the dynamic ocean model has been developed (HadCM3L), which runs at the same horizontal resolution as the atmospheric component. This low resolution version of the model requires flux adjustments but is computationally cheaper, allowing longer integrations (see, for example Jones *et al.* (2001)) Flux adjustments modify the ocean-atmosphere fluxes so that the coupled model is stable for long integrations (for further discussion see Meehl (1992), pp. 572-577).

In this thesis HadSM3 is used. Using HadCM3, or HadCM3LC, would allow the global carbon cycle to be simulated interactively, and would be able to capture changes in ocean circulation, however these models are computationally expensive. The studies presented in this thesis are not designed to correspond to particular climatic periods and it is beyond the scope of this thesis to investigate interactions between terrestrial biosphere and coupled atmosphere-ocean phenomena, for example ENSO events. Using the HadAM3 model would eliminate the possibility of SST feedbacks. The HadSM3 slab ocean model will therefore be used because of its ability to simulate SSTs, and the fact that it is relatively inexpensive to integrate.

2.2.3 Land Surface

The version of HadSM3 used in this thesis contains the MOSES2 surface exchange scheme. The previous version of MOSES2, MOSES, is discussed in Cox *et al.* (1999). Many of the processes in MOSES2 are the same as MOSES, but MOSES2 includes the TRIFFID DGVM. Essery *et al.* (2001) describe MOSES2, however the description of the land surface processes in HadSM3 will make use of equations presented in both Cox *et al.* (1999) and Essery *et al.* (2001) as each paper describe different aspects of the surface exchange scheme. Smith (1993) will also be used as a source of equations, especially for the boundary layer flux equations.

In the surface exchange model there are nine different land surface types. These land surface types are: broadleaf tree, needleleaf tree, shrub, C3 type grass, C4 type grass, urban, bare soil, inland water, and permanent land ice. Each land surface grid box can be covered by a

combination of any of the first 8 of these land surface types. Grid boxes covered by permanent land ice is assumed to be completely covered. The fraction of a grid box covered by a land surface type (its fractional coverage) determines how much the land surface type contributes to the grid box surface properties. Most land surface parameters are weighted by the fractional coverage of the associated land surface type. This is the case for the surface albedo, infiltration rate, canopy heat capacity, canopy coverage, and soil moisture extraction by roots. Canopy conductance and soil moisture extraction rates are averaged over non-lake land surface types. The roughness length, z_o, for each PFT is a fraction of the vegetation height ($\frac{1}{20}$ for trees, $\frac{1}{10}$ for other vegetation types). The roughness lengths for the other land surface types are constant (urban = 1.5m, water = 3×10^{-4}m, soil = 3×10^{-4}m, and ice = 1×10^{-4}m). The grid box mean value is calculated by:

$$z_o = L_{blend} \cdot exp\{-[\Sigma_j \frac{\nu_j}{ln^2(L_{blend}/z_{o,j})}]^{-1/2}\} \quad (2.4)$$

L_{blend} is a defined height, presumed to be between the height at which the flow is independent of surface roughness and the near-surface height where the local flow is determined entirely by $z_{o,j}$ (Mason (1988)). A value of L_{blend}=20 m is used in HadSM3. ν_j is the fractional coverage of land surface type j. $Z_{o,j}$ is the roughness length of land surface type j (m). The surface albedo for vegetated surface types (unweighted by fractional coverage) is given by:

$$\alpha_o = \alpha_{soil} + (1 - exp^{-LAI/2})(\alpha_o^\infty - \alpha_{soil}) \quad (2.5)$$

α_{soil} is the bare soil albedo and is specified. α_o^∞ is a PFT dependent constant. LAI is the leaf area index and is a common measure of the amount of leaves. LAI is the area of leaves per unit area of ground taking one side of the leaf into account.

The state of the land surface at any time is defined by the amount of snow present, the canopy water content, and soil moisture and temperature profiles. As rain falls on vegetation some of the water is retained in the vegetation canopy. This amount is free to evaporate back into the atmosphere. The evaporative flux from the canopy water store is given by:

$$E_c = f_a \frac{\rho_{air}}{r_a}[q_{sat}(T_*) - q_1] \quad (2.6)$$

f_a is the fraction of the grid box with a wet canopy. ρ_{air} is the surface air density (kg m^{-3}). q_1 is the surface air specific humidity (kg kg^{-1}). $q_{sat}(T_*)$ is the saturated specific humidity (kg kg^{-1}) at the surface temperature, T_* (K). r_a is the aerodynamic resistance to the transport of moisture, and depends on the roughness length, wind speed and atmospheric stability (s m^{-1}). r_a is estimated by:

$$r_a = (C_H|v_1 - v_0|)^{-1} \tag{2.7}$$

v_1 is the horizontal wind velocity of the surface air. v_0 is the horizontal wind velocity at the surface. v_0 is zero for land points, but is equal to the prescribed current over sea grid boxes. The exchange temperature and moisture between the surface and the immediate air level is influenced by the exchange coefficient, C_H. C_H is given by:

$$C_H = f_h \cdot k_v^2 \{ln(\frac{z_1 + z_0}{z_0})ln(\frac{10(z_1 + z_0)}{z_o})\}^{-1} \tag{2.8}$$

f_h is a measure of the stability of the atmosphere, and incorporates a dependency on the surface air wind speed, the vertical gradients of temperature and humidity, and the surface resistance. z_1 is the height of the lowest atmospheric layer. k_v is the von Karman constant, k_v = 0.4. The amount of rainfall not retained in the canopy is given by:

$$T_F = R_n(1 - \frac{C}{C_m})exp(-\frac{\epsilon C_m}{R\Delta t}) + R_n\frac{C}{C_m} \tag{2.9}$$

R_n is the rainfall rate (kg m^{-2} s^{-1}). ϵ represents the fraction of the grid box over which the rainfall occurs. For large-scale rain $\epsilon = 1$, whilst $\epsilon = 0.3$ for convective rainfall reflecting the typical scales of convection and large scale precipitation. Δt is the timestep for updating the canopy water content and is 30 minutes in the model. C_m is the canopy water capacity and increases with increasing vegetation height. C is the canopy water content and is updated by:

$$C^{n+1} = C^n + (R_n - T_F)\Delta t \tag{2.10}$$

When water reaches the soil it enters, or flows out of the grid box. Surface run-off is calculated by:

$$Y = \begin{cases} T_F - R_n\frac{C}{C_m}[1 - exp(-\frac{\epsilon K C_m}{R_n C})] & \text{K } \Delta t \leq \text{C} \\ R_n \cdot exp[\frac{-\epsilon(K\Delta t + C_m - C)}{R_n \Delta t}] & \text{K } \Delta t > \text{C} \end{cases} \tag{2.11}$$

K is the surface infiltration rate. K depends on the land surface type and the soil properties (both constants in HadSM3). Moisture that reaches the soil, and is not lost as run-off infiltrates the soil.

Moisture also evaporates from the soil surface. The bare soil evaporation is given by:

$$E_b = (1 - f_a)(1 - \nu)\beta \frac{\rho_{air}}{r_a + r_{ss}}[q_{sat}(T_*) - q_1] \quad (2.12)$$

β is a function of top level soil moisture and incorporates the hydrological properties of the soil predicting how saturated the soil layer is. Soil is specified to have one of three soil types: fine, medium, and coarse. The global distributions of soil types are specified using the Wilson and Henderson-Sellers data set (Wilson and Henderson-Sellers (1985)). r_{ss} is the soil surface aerodynamic resistance and is set to 100 s m^{-1}.

Vegetation roots draw moisture from lower levels, soil evaporation only from the top level. When soil moisture is drawn into the roots the transpiration of moisture through the leaves is predicted by:

$$E_\nu = (1 - f_a)\nu \frac{\rho_{air}}{r_a + \frac{1}{g_c}}[q_{sat}(T_*) - q_1] \quad (2.13)$$

g_c is the stomatal conductance of the vegetation canopy to water vapour (m s^{-1}). g_c is dependent on the predicted photosynthesis rate:

$$g_c = A \frac{1.6RT_*}{\Delta CO_2} \quad (2.14)$$

A is the photosynthesis rate (mol CO_2 m^{-2} s^{-1}). R is the perfect gas constant (8.3143$\times 10^3$ J K^{-1} $kmol^{-1}$). ΔCO_2 is the CO_2 gradient between internal and atmospheric partial pressures (Pa).

When there is no snow covering on the grid box evaporation from the surface is assumed to be the sum of contributions from eqns. 2.6, 2.12, and 2.13. When there is a covering of snow the sublimation of snow is the only process in the evaporative flux. A layer of snow on the grid box also alters the surface albedo, and acts to cool the surface temperature. Melting snow also supplies water to the soil, and and excess amounts of melt-water is allowed to exit the grid box as run-off. Snow melt run-off is estimated using eqn. 2.11, substituting the snow melt rate S_m for R_n and using $\epsilon = 1$. The total input of moisture to the soil is the throughfall (T_F) and snowmelt, minus the run-off, for each grid box land type (weighted by fractional coverage). Evaporation

also depends on the overlaying air humidity and the surface resistance, incorporating the effects of variable roughness length and atmospheric stability.

In the model, soil is represented by four layers. The depths of these layers are set to 0.1, 0.25, 0.65, and 2.0 metres. In the surface layer (0.1 m layer) soil moisture is increased through snow melt and throughfall of rain. Moisture from the top layer is then decreased according to the flow of water into lower layers, the evaporation from bare soil, and water taken into plant roots. The vertical flux of water (W) uses a form of the Darcy equation (for further discussion of Darcy's equation see Price (1996), pp. 48-57, for example):

$$W = K_s S_u^{2b+3}\left(\frac{\Psi_s \partial S_u^{-b}}{dz} + 1\right) \quad (2.15)$$

K_s, Ψ_s, and b are empirical soil dependent constants. S_u is the unfrozen soil moisture content (kg m^{-2}).

The extraction of water from any particular soil layer by roots is proportional to the total evapotranspiration. The constant of proportionality reflects the vertical distribution of roots. Different PFTs have different root depths allowing tree PFTs to access moisture from greater depths than shrub or grasses.

In MOSES2 soil moisture interacts with the thermal properties of the soil. The temperature of a soil layer is determined by heat diffusion with the surrounding layers and the transport of heat associated with moisture fluxes. The heat capacity of the soil is determined by soil properties and the amount of frozen and unfrozen moisture. When there is a layer of snow on the grid box surface the thermal conductivity of the soil in the top two layers is increased. The heat capacity of a soil layer also takes into account the apparent heat capacity associated with changes in moisture phases.

The surface temperature is determined by the energy balance at the surface:

$$C_c \frac{dT_*}{dt} = SW_{net} + \downarrow LW - \sigma T_*^4 - H - LE - L_f S_n - G_o \quad (2.16)$$

C_c is the canopy heat capacity and depends on the amounts of carbon stored in wood and leaves. For non-vegetative land surface types C_c is set to zero. $\downarrow LW$ is the downward longwave radiation flux (W m^{-2}). SW_{net} is the net shortwave radiation flux (W m^{-2}). σ is the Stefan-Boltzmann constant (5.67×10^{-8} W m^{-2} K^{-4}). σT_*^4 is the emitted longwave radiation from the surface. H is the sensible heat flux (the transfer of heat by dry air ; Wm^{-2}). E is the total evapotranspiration from the surface (kg m^{-2} s^{-1}). L is the latent heat of evaporation (2.501×10^6 J kg^{-1}). LE is therefore the energy transported by the moisture. $L_f S_m$ incorporates the effect of snowmelt. G_o is the flux of heat into the ground. G_o depends on the top level soil properties and the fraction of the grid box covered by vegetation canopy. Snow also affects the heat flux by modifying the thermal conductivity. The sensible heat flux (H) is given by:

$$H = \frac{\rho_{air} C_p}{r_a}(T_* - T_1 - \frac{g}{C_p} z_1) \quad (2.17)$$

C_p is the heat capacity of air (J kg^{-1} K^{-1}). T_1 is the temperature at the immediate atmospheric layer. g is the acceleration due to gravity (9.81 m s^{-2} at sea level). The downward flux of momentum at the surface (τ_m) is given by:

$$\tau_m = C_D |v_1 - v_0| (v_1 - v_0) \quad (2.18)$$

C_D is the drag coefficient and in MOSES2 is equal to:

$$C_D = [k ln(\frac{z_1 + z_0}{z_0})]^2 \quad (2.19)$$

2.3 Carbon cycle treatment

2.3.1 Oceanic carbon

The GCM used in this thesis, HadSM3, simulates the ocean using a thermodynamic ocean model. HadSM3 is therefore unable to simulate the oceanic carbon cycle, which requires the simulation

of upwelling and other circulation features. A description of the oceanic carbon cycle will be included here in order to give a general overview of the carbon cycle in HadUM3.

The HadCM3 ocean model includes representations of both inorganic and organic carbon cycles. The flux of carbon into the ocean is proportional to the partial pressure gradient of CO_2 across the ocean-atmosphere interface, and also depends on the strength of surface winds.

After CO_2 has entered the ocean it is represented as the total dissolved inorganic carbon, DIC. This is then redistributed by ocean dynamics, and DIC is treated as a tracer. This process may result in carbon taken into the ocean at one point being emitted at another grid box. The ocean carbon cycle model also simulates alkalinity. Alkalinity is advected similarly to DIC and is also altered by ocean biology. The other factors controlling carbon distributions in the oceans are organic effects.

The organic carbon model is presented in Palmer and Totterdell (2001). Dynamic pools of phytoplankton, zooplankton, a generic nutrient, and Detritus (also referred to as particulate organic matter, POM) are included. Each of these components other than nutrients are modelled in terms of their carbon content and are treated as tracers within the dynamic ocean model.

In the model phytoplankton feed on nutrients and respire nutrients back into the ocean. When phytoplankton die a fraction of carbon returns to the nutrient pool whilst the rest forms detritus. Phytoplankton are also eaten by zooplankton. Zooplankton feed on the phytoplankton and on detritus. Some of the carbon taken in through grazing is lost in the process and forms detritus. When zooplankton die the zooplankton carbon returns to dissolved nutrients and detritus. Detritus may also sink out of the layer or dissolve. Dissolving detritus returns to the nutrient pool.

2.3.2 Terrestrial Photosynthesis model

The photosynthesis model is a central component of both the dynamic global vegetation model, DGVM, and the surface exchange scheme in the Met. Office climate model. MOSES2 predicts photosynthesis rates from environmental conditions. In the DGVM, photosynthesis is the main input, driving vegetation expansion, and leaf area index (LAI) changes. The surface exchange scheme uses a closure approach linking photosynthesis rates to canopy conductance (e.g. Sellers *et al.* (1997)). This approach means that the photosynthesis model plays a central role in both the terrestrial carbon cycle and the surface fluxes (eqn. 2.16). It is therefore important to devote time to discussing the properties of the photosynthesis model.

The photosynthesis model was initially presented in Collatz *et al.* (1991) for C3 type photosynthesis and then in Collatz *et al.* (1992) for C4 type photosynthesis. The combined photosynthesis model implemented in MOSES2 was initially presented in Cox *et al.* (1999). Other photosynthesis mechanisms such as crassulacean acid metabolism (CAM) photosynthesis (see Mooney and Ehleringer (1997), pp. 21-23) are relatively rare and are not included in the MOSES2 photosynthesis model. CAM photosynthesis is found in certain desert plants and some tropical epiphytes (non-parasitic plants living on other plants). In CAM plants the stomata open during the night. CO_2 diffusing into the CAM plant is stored as an organic acid, via the PEP reaction. During the day, whilst the stomata are closed, light is used to process the stored CO_2. The CAM mechanism allows plants to minimise the loss of moisture through stomata, explaining their ability to survive in dry environments.

In MOSES2 the gross photosynthesis rate is assumed to be limited by three factors. In C3 plants these are RuBP limiting (Wc), light limiting (Wl), and limitation by the transport of photosynthesis products (We). In C4 plants these are PEP limited (Wc), light limited (Wl), and the transport of photosynthetic products (We; Cox *et al.* (1999)). Most photosynthesis schemes assume a sharply defined cut-off between limitation factors, whereas the MOSES2 photosynthesis scheme assumes a smoothed minimum of the three limiting factors, producing a gradual transition (Huntingford *et al.* (2000)), which may be more appropriate for grid box scale

predictions.

These limiting factors, Wc, Wl, and We are sensitive to the local environment. Equations 2.20, 2.21, and 2.22 define the photosynthesis model, as presented in Cox *et al.* (1999), appendix A.

$$W_c = \begin{cases} V_m(\frac{C_i-\Gamma}{C_i+2\Gamma}) & \text{C3 plants} \\ V_m & \text{C4 plants} \end{cases} \tag{2.20}$$

$$W_l = \begin{cases} 0.08(0.85)I_{PAR}(\frac{C_i-\Gamma}{C_i+2\Gamma}) & \text{C3 plants} \\ 0.04(0.83)I_{PAR} & \text{C4 plants} \end{cases} \tag{2.21}$$

$$W_e = \begin{cases} 0.5V_m & C3 \text{ plants} \\ 2\times 10^4 V_m \frac{C_i}{p_*} & C4 \text{ plants} \end{cases} \tag{2.22}$$

V_m is the maximum rate of photosynthesis (mol CO_2 m^{-2} s^{-1}). V_m is a function of temperature and leaf nitrogen content (eqn. 2.23), in this model leaf nitrogen content is assumed to be constant. Γ is the photorespiration compensation point. C_i is the internal CO_2 partial pressure. p_* is the surface pressure (Pa). I_{PAR} is the incoming photochemically active radiation (mol PAR photons m^{-2} s^{-1}).

$$V_m = \frac{V_{max}2.0^{0.1(T_c-25)}}{\{1+exp[0.3(T_c-T_{upp})]\}\{1+exp[0.3(T_{low}-T_c)]\}} \tag{2.23}$$

T_c is the leaf temperature. V_{max} is the magnitude of the maximum rate of photosynthesis. V_{max} is assumed to be proportional to the leaf nitrogen content. Equation 2.23 introduces upper and lower temperature controls (T_{upp},T_{low}), defining environmental niches of each PFT. V_m is plotted for the different PFTs in fig. 2.1.

The photorespiration compensation point, Γ, is defined as :

$$\Gamma = \begin{cases} \frac{O_a}{2\tau} & \text{for C3-type plants} \\ 0.0 & \text{for C4-type plants} \end{cases} \tag{2.24}$$

As was described in chapter 1, photosynthesis (involving the fixation of CO_2) is balanced against photorespiration (involving oxygen), and increased oxygen amounts present in the leaf

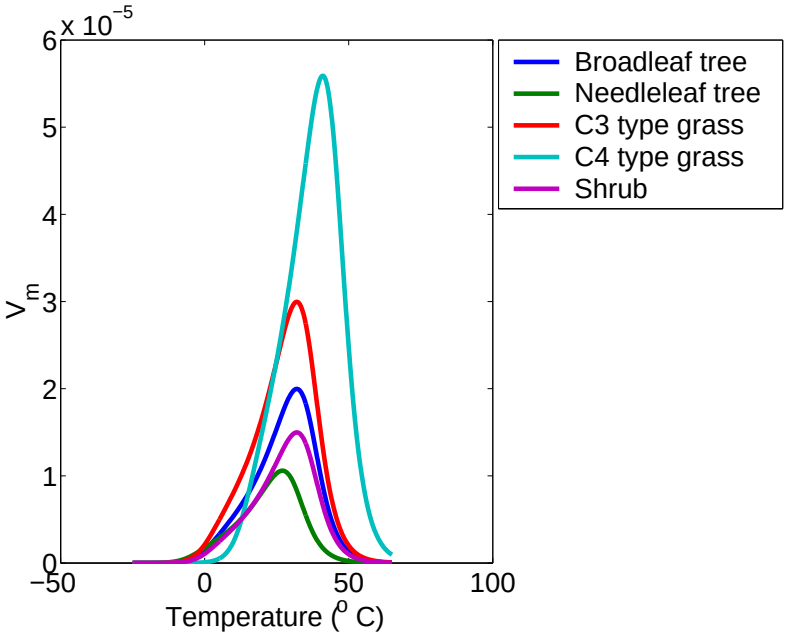

Figure 2.1 *The range of temperatures defined as suitable for each TRIFFID PFT, as incorporated into the photosynthesis model through the Vm function (mol CO_2 m^{-2} s^{-1}), eqn. 2.23.*

reduce photosynthesis in favour of photorespiration. The photorespiration compensation point, eqn. 2.24, incorporates this effect. The C4 mechanism evolved to increase the local CO_2 concentration, and C4 photosynthesis is not sensitive to atmospheric oxygen concentration, O_a (Pa). τ incorporates the effects of temperature into the reaction, $\tau = 1482.00^{0.1(T_c - 25.0)}$.

The internal CO_2 pressure, C_i, is determined by the stomatal size and the atmospheric CO_2 level, C_a (Pa). C_i is defined in eqn. 2.25. The internal CO_2 concentration is influenced by the humidity deficit. This is the closure assumption, and is the basis of eqn. 2.25. Equation 2.25 also implies that changes in the atmospheric CO_2 will alter the transport of moisture through vegetation.

$$C_i = (C_a - \Gamma)F_o(1 - \frac{\Delta Q}{\Delta Q_{crit}}) + \Gamma \tag{2.25}$$

ΔQ is the canopy level humidity deficit. ΔQ_{crit} is the critical humidity deficit, at which the stomata close. F_o is the maximum possible ratio of internal to external CO_2.

Figure 2.2 shows how photosynthesis rates vary as a function of different environmental conditions, for C3 and C4 grasses. Figure 2.2 actually shows how canopy conductance varies

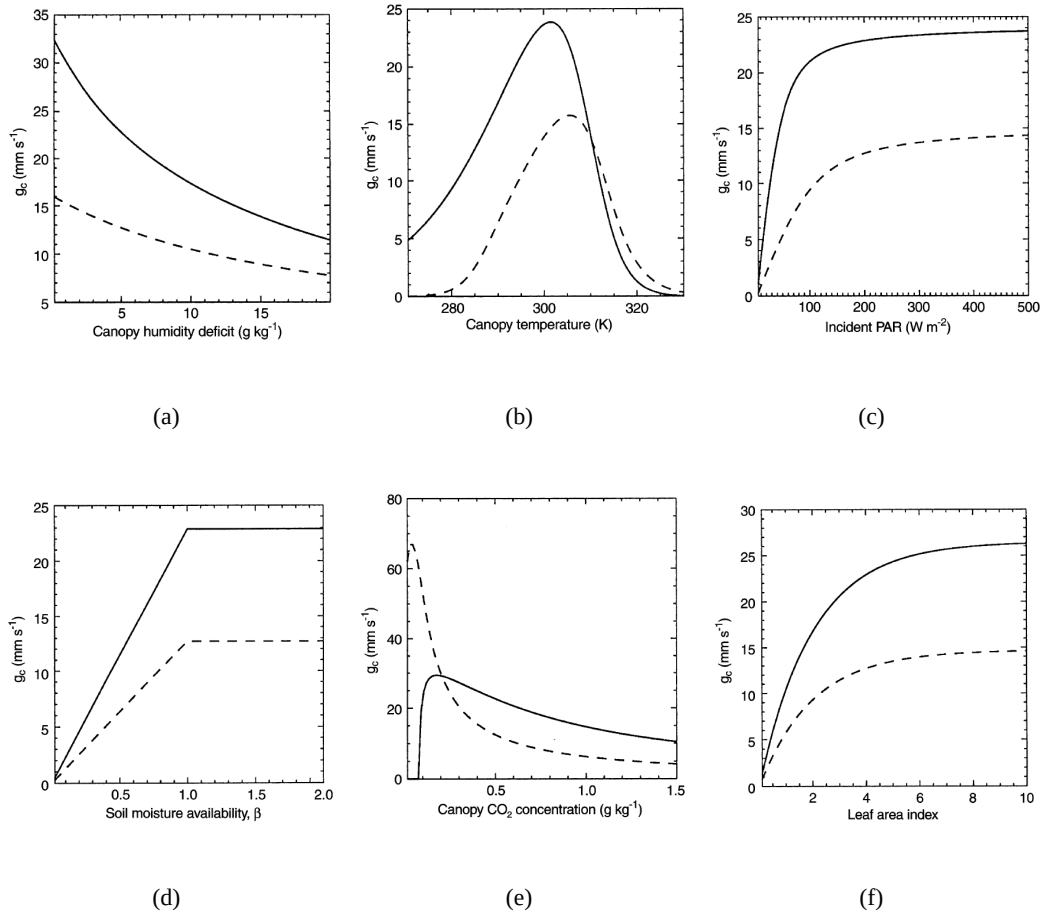

Figure 2.2 *The response of the photosynthesis model to changing environmental parameters. gc is the stomatal conductance. The solid line is the response of C3 grass. The dashed line is the response of C4 grass. Reproduced from Cox* et al. *(1999).*

with environmental conditions, but eqn. 2.14 implies that fig. 2.2 also illustrates qualitatively the photosynthesis behaviour. Humidity deficit, photochemically active radiation (PAR), soil moisture and leaf area index all influence photosynthesis, but the effects saturate with relatively large values. The canopy CO_2 content and canopy temperature, however, introduce a threshold, and above a certain temperature the dominance of C4 and C3 type photosynthesis is reversed.

The canopy temperature dependency introduces an optimal temperature for photosynthesis. In the C3 photosynthesis scheme the CO_2 sensitivity also introduces a CO_2 level below which C3 photosynthesis stops, due to CO_2 starvation. There is interaction between the canopy temperature threshold and the canopy CO_2 cut-off point. The canopy temperature curve, fig. 2.2(b) was generated with CO_2 = 0.490 g kg^{-1}, and fig. 2.2(e) shows that at the optimal temperature, the maximum photosynthesis rate is determined by CO_2 level. Therefore the temperature at which C3 grass is replaced by C4 grass is different for different CO_2 levels, assuming that higher photosynthesis rates implies dominance (see chapter 3). This dependency is realistic (Ehleringer and Cerling (2001), pp. 268). Soil moisture also modulates the photosynthesis rate. Photosynthesis is assumed to be maximum at the optimum soil moisture content and decreases linearly on either side of this value.

Photorespiration is assumed to be proportional to the maximum rate of photosynthesis, V_m. The balance between photosynthesis and photorespiration is defined as the net primary productivity, NPP, and is the net amount of carbon assimilated into vegetation (kg C m^{-2} s^{-1}).

The photosynthesis model simulates the photosynthetic rates of a single leaf, and the predicted rate of photosynthesis must therefore be scaled up to the canopy scale. In MOSES2 scaling up is achieved by assuming that the relative magnitude of the different limiting factors other than light remains constant throughout the canopy. To a first approximation light will decrease exponentially throughout the vegetation canopy (applying Beers law). This leads to a scaling constant f_{par} such that $NPP_{canopy} = f_{par} NPP_{leaf}$, where $f_{par} = 2 - 2e^{-0.5LAI}$ (Cox *et al.* (1999)). f_{par} also relates leaf-scale predictions of stomatal conductance, and photorespiration to canopy scale values.

2.3.3 Vegetation structure

In TRIFFID vegetation structure is updated as a function of the predicted net primary productivity (the amount of carbon assimilated). In TRIFFID vegetation structure is primarily expressed in terms of vegetation carbon density (kg C m^{-2}), and the fraction of the grid box covered by each PFT. These in turn are used to derive to values of roughness length, and surface albedo.

The main equations of the dynamic vegetation structure are included in chapter 3, where they are used to derive a simplified model. These equations will therefore not be reproduced here.

One benefit of dynamically modelling global vegetation dynamically is that it allows the simulation of the terrestrial carbon cycle interactively. Vegetation in TRIFFID can be thought of as a volume of carbon, the product of fractional coverage, vegetation carbon density, and grid box surface area. Carbon enters the terrestrial carbon cycle through the photosynthesis module in MOSES2. This carbon is then stored in either stem, leaves, or root carbon pools. NPP is calculated every 30 minutes, and the accumulated NPP is passed to TRIFFID and used to update vegetation structure every 10 days.

2.3.4 Soil carbon pool

In MOSES2 carbon enters the soil carbon pool when vegetation drops leaves as the result of natural turnover, or in response to environmental change. Litterfall may also take place in response to a large scale disturbance (prescribed in this version of the model) and the effects of competition with other PFTs . The litterfall input term is proportional to the different vegetation carbon pools (stem, leaf, and root). Temperatures below which vegetation increasingly drops leaves are introduced in the model, and a detailed representation of leaf phenology dynamics models has been introduced to model the environmental tolerances of the leaves. The carbon

inputs from the different PFTs are weighted according to fractional coverage.

In the soil, carbon is respired back into the atmosphere by the action of microbes. Soil carbon content is then the balance between litterfall and soil respiration. Soil respiration (R_s) is estimated in the model by:

$$R_s = K_s C_s f_\theta q_{10}^{0.1(T_s-25)} \tag{2.26}$$

T_s is the soil temperature (^{o} C). K_s is the soil respiration at T_s = 25^{o}C. f_θ is a function of soil moisture, introducing the effects of soil moisture saturation and drought. In MOSES2 q_{10} is assumed to be 2.0 and an increase in soil temperature of 10^{o}C results in a doubling of soil respiration. If soil respiration increases rapidly and is larger than the rate of NPP then the terrestrial carbon cycle would be a net source of carbon; because global temperature is expected to rise in the immediate future due to anthropogenic emissions this is an important issue (Grace and Rayment (2000), Cox *et al.* (2000), Cox *et al.* (2001)). Cox *et al.* (2001) show that a CO_2 sink-to-source transition of the land surface is inevitable if the CO_2 enhancement of photosynthesis saturates at high levels of CO_2, and if $q_{10} > 1$ (soil respiration continues to increase with increasing temperature). The first condition is generally believed to be true, whilst the truth of the second condition is more controversial. It has recently been suggested that 1.0 is a more realistic value of q_{10} (Giardina and Ryan (2000)) implying that the sink-to-source transition would not occur. However Jones and Cox (2001a) estimate q_{10} from atmospheric variability of CO_2 levels, and show that a value of $q_{10} = 2.1 \pm 0.7$ is consistent with the observed variability in atmospheric CO_2. This is achieved by scaling the results from Jones *et al.* (2001) to match observed CO_2 variability. Jones *et al.* (2001) simulate the carbon cycle response to ENSO. This modelling approach to validating the q_{10} value assumes that the model's climate response to ENSO is realistic (Jones *et al.* (2001)). However independent of the validity of this assumption, Jones and Cox (2001a) show that using $q_{10} = 2.0$ is valid within the HadSM3LC model, and $q_{10} = 2.0$ will be used in this thesis.

2.4 Model Validation

Testing the ability of HadUM3 to simulate climate against observations is vital. Various validation studies have been completed using different versions of the HadUM3 model. Most of the studies use either HadAM3, HadCM3, or HadCM3L (the low ocean resolution, flux corrected coupled model normally used for interactive ocean carbon cycle simulations). Some of the model tests require a particular version of HadUM3, for example testing the ENSO variability in the model requires either HadCM3 or HadCM3L as ENSO is a coupled atmosphere-ocean phenomena. In discussing the validation of the HadUM3 models results from HadSM3 validation will be focussed on because HadSM3 is used here; however results from other versions of HadUM3 will be included where results for HadSM3 are unavailable, or when the validation would not be possible using HadSM3.

The difference between HadUM3 versions is mainly the different approaches taken to model the ocean. Hewitt *et al.* (2003) compare the simulation of climate at the last glacial maximum using both HadSM3 and HadCM3. The differences in the annual mean surface temperatures between HadSM3 and HadCM3 are shown in fig. 2.3.

Another difference between the dynamic and thermodynamic ocean models is in simulations of the transient response to climate change. Manabe *et al.* (1991) demonstrated important differences in the transient response to gradual changes in the atmospheric CO_2 content. These differences are up to 2^o C in the surface air temperature, and occur over northern North Atlantic and the Circumpolar regions in the Southern Hemisphere. Both of these regions correspond to regions of deep vertical mixing in the ocean. In these regions the thermodynamic ocean model (which assumes a constant mixed layer thickness) under-estimates the depth of the mixed layer, and under-estimates the heat capacity of the ocean in these regions. This means that in the dynamic ocean model the mixed layer can change its apparent timescale (associated with the heat capacity of the ocean surface), whilst this mechanism is not included in the slab ocean model used here. The importance of this mechanism for vegetation-climate interactions could be tested using a fully coupled atmosphere-vegetation-ocean model, but this is not considered here.

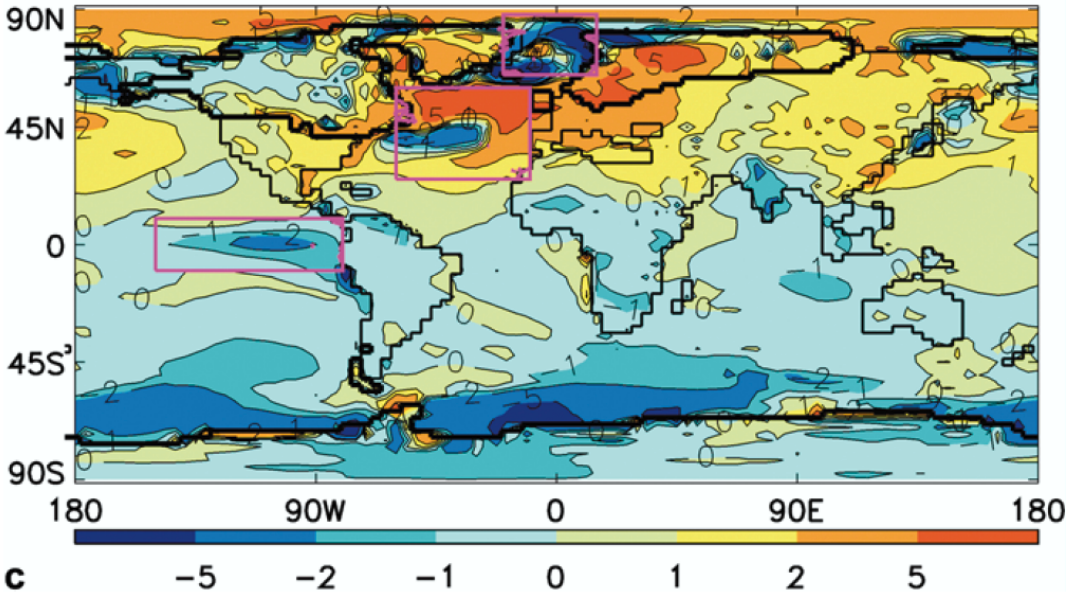

Figure 2.3 *Difference between predicted annual mean surface temperatures (^oC) using HadSM3 and HadCM3 for the last glacial maximum (HadCM3-HadSM3). This figure is reproduced from Hewitt* et al. *(2003).*

Averaged over the globe, both HadSM3 and HadCM3 predict almost identical cooling (the difference is 0.1^oC). Large differences between the two models that Hewitt *et al.* (2003) highlighted as most important are shown in fig. 2.3 by magenta-coloured boxes. At the region off the coast of Peru in fig. 2.3 HadSM3 is warmer than HadCM3. Hewitt *et al.* (2003) show that this difference is attributable to enhanced upwelling, which HadSM3 does not attempt to simulate. The other main differences are due to the inability of HadSM3 to simulate changes in the North Atlantic thermohaline circulation.

Figure 2.4 compares the pre-agricultural climate simulated by the HadSM3 model with the Legates and Willmott (1990) climatology. Figure 2.4(a) shows the difference in annual mean 1.5 metre air temperature, whilst fig. 2.4(b) shows the difference in the annual mean surface precipitation. Figure 2.4(a) shows that the HadSM3 climatology is almost uniformly cooler than the Legates and Willmott (1990) climatology. This difference is especially pronounced over

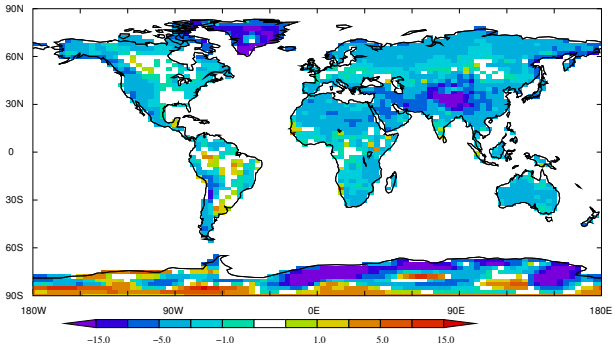

(a)

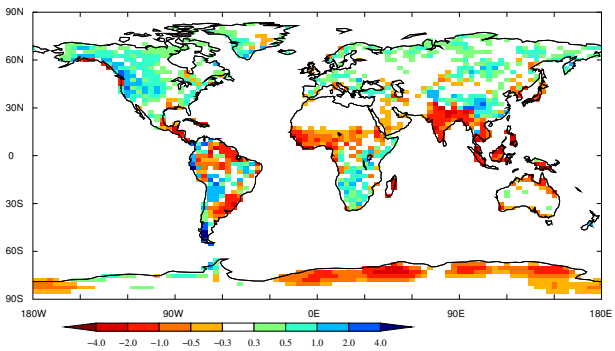

(b)

Figure 2.4 *Comparison of the annual mean temperature and precipitation fields from the pre-agricultural control simulation (using HadSM3) against the Legates and Willmott (1990) climatology (HadSM3-Climatology). a) 1.5 metre air temperature (^oC). b) Precipitation (mm day^{-1}). Only the differences over land are plotted.*

some regions of Antarctica, Greenland, and Tibet. Some of the grid boxes in South America are warmer than the observations. The comparison of HadSM3 annual mean precipitation against observations in fig. 2.4(b) show that there is a substantial dry bias over various regions of South America (including the Amazon region). The Sahara/Sahel interface is also too dry, as is India, and the Maritime continent, relative to the Legates and Willmott (1990) climatology. This suggests a general under-prediction of tropical precipitation. HadSM3 also over predicts precipitation in the Northern Hemisphere boreal regions, by 0.5 mm day^{-1}.

In order to investigate the convection scheme within HadSM3 the relationship between sea surface temperature (SST) and out-going longwave radiation (OLR) in the tropics (30 ^{o} N to 30 ^{o} S) is plotted, from a 20 year control simulation (this simulation is discussed further in later sections of this chapter). Figure 2.5 compares the OLR, SST relationship in HadSM3 with observations. The observations used are from Graham and Barnett (1987), and are from January 1974 to December 1979. Deep tropical convection has a high cloud top, and results in a reduction of OLR. Observations such as Graham and Barnett (1987) suggest that tropical deep convection requires SST values greater than 27.5^o C, which is seen in fig. 2.5. Figure 2.5 also shows that HadSM3 captures this relationship, including reproducing the critical temperature value. HadSM3 over-predicts OLR below the critical SST, but this will not be investigated further here though it may be related to differences due to the experimental setup (e.g. CO_2 values), or the effects of non-convective clouds. In validating the convection scheme when it was introduced, Gregory and Rowntree (1990) also compare the predicted OLR, SST relationship with the observations of Graham and Barnett (1987) and show that the convection scheme reproduces the observations. The convection scheme validation performed by Gregory and Rowntree (1990) uses a previous version of the GCM, and the convection scheme used here also includes the effects of momentum transfer and downdrafts (see Gregory *et al.* (1997)).

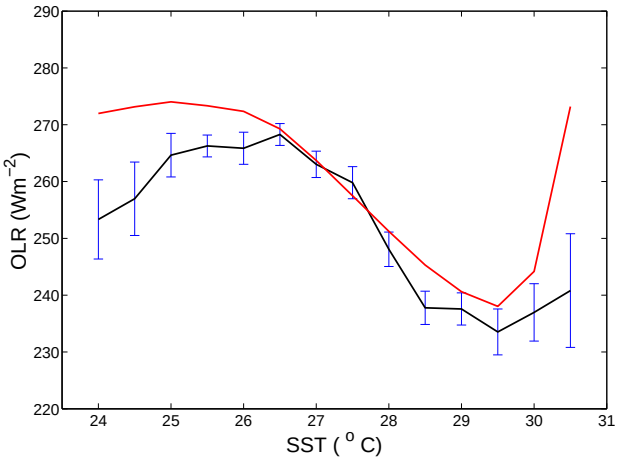

Figure 2.5 *Validation of the OLR-SST relationship in HadSM3 against observations from Graham and Barnett (1987). The red line shows the mean SST-OLR relationship from 20 years of data from a pre-agricultural control run using HadSM3. The black line shows observed SST-OLR relationship. The uncertainty bars on the observations are 95% confidence intervals.*

The radiation scheme included in HadUM3 has variable resolution (the number of divisions the radiation spectrum is split into). Variable resolution allows the coarse resolution of the radiation scheme used in the model to be directly validated against a more realistic model. Figure 2.6 shows the difference between high resolution and low resolution settings. Figure 2.6 shows that low resolution setting captures the behaviour of the high resolution model.

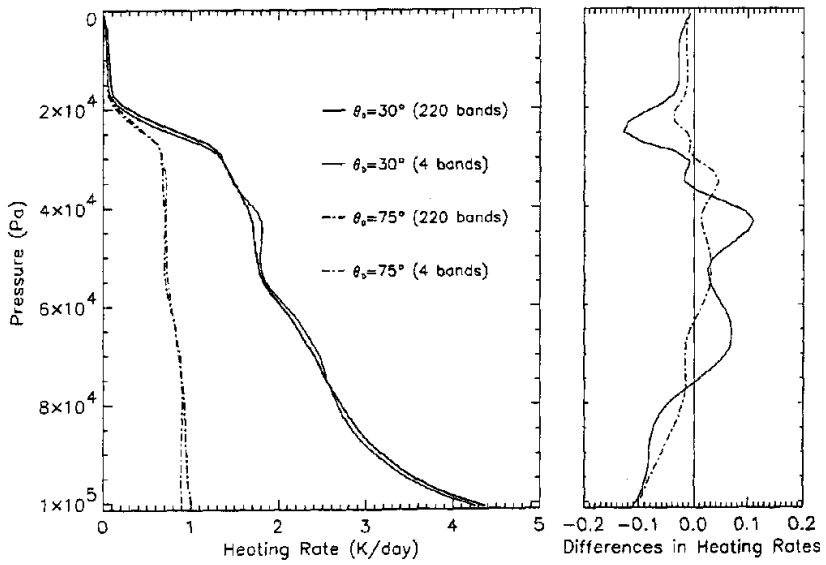

Figure 2.6 *Comparison of different resolutions of the radiation code, for shortwave radiation heating. Zenith angle 30 ^{o} (dashed lines) and 75 ^{o} (dotted lines) are plotted, for 220 band resolution and 4 band resolution. Also plotted is the differences in heating rates (4 band - 220 band resolution). The figure is reproduced from Edwards and Slingo (1996).*

Pope *et al.* (2000) show that most of the differences in the predicted atmospheric temperature fields between HadSM2 and HadAM3 are due to the different radiation scheme used. The ability of the radiation code within the GCM to reproduce observations is tested by Pope *et al.* (2000). Pope *et al.* (2000) compare the predicted OLR (at the top of the atmosphere) from HadAM3 to the ERBE climatology (Barkstrom *et al.* (1989)). The differences between HadAM3 and the ERBE climatology vary regionally, are positive and negative, and have a maximum magnitude of 30 Wm^{-2} (about 10%). Perhaps most important for this thesis, HadAM3 over-predicts OLR across much of Africa, the Amazon region, the Maritime continent, and large regions of North

America and Asia. The largest differences in these regions are at tropical latitudes. In the tropics the regions of over-prediction of OLR corresponds to regions where the model is too dry (Pope *et al.* (2000)). This suggests that the over-prediction of OLR is due to the under-prediction of convection.

Validation of the land surface model was carried out by Harding *et al.* (2000) using 3 years (1995-1997) of observations of surface fluxes, surface meteorology, and soil moisture, over C3 type grassland. A more global validation of the surface exchange scheme was carried out by Cox *et al.* (1999), where the surface exchange scheme is shown to improve the ability of the Met. Office climate model to simulate current climate. Previous validation of the land surface exchange scheme also acts to validate the photosynthesis model, due to the closure equation, eqn. 2.25. In addition to this, Cox *et al.* (1998) test the photosynthesis model against observations of CO_2 and water vapour fluxes, over C4 type grassland. Harris *et al.* (2003) test the ability of MOSES2 to simulate surface fluxes of heat, moisture, and CO_2 at two forest sites in the Amazon region. For these sites the standard version of MOSES2 is shown to under-predict the stomatal conductance, g_c. Using the first site Harris *et al.* (2003) recalibrate the MOSES2 photosynthesis model. Using data from the second site Harris *et al.* (2003) show that this improves the ability of MOSES2 to simulate surface fluxes. Harris *et al.* (2003) do not demonstrate that predictions of stomatal conductance in MOSES2 is uniformly under-predicted, however this result suggests that MOSES2 may under-predict stomatal conductance in the Amazonian region.

The ability of MOSES2 to simulate present-day vegetation distributions is assessed by Cox *et al.* (2001) and Betts *et al.* (2003). Figure 2.7 shows the validation of vegetation distributions against satellite observations (Loveland *et al.* (2000)), reproduced from Betts *et al.* (2003). Betts *et al.* (2003) conclude that MOSES2 reproduces global vegetation reasonably. Of particular interest here, however, are the differences associated with the Amazon forest and the Sahara-Sahel interface. In HadCM3LC near the mouth of the Amazon river there is a region which receives insufficient precipitation to support trees. This dry bias is a common feature of GCMs (Betts *et al.* (2003)). HadCM3LC also predicts the Sahara-Sahel interface to be 3^o to 5^o further south than observed. This may result from an under-representation of vegetation feedbacks in

this region. This hypothesis is supported by the inter-comparison study of Joussaume *et al.* (1999) which shows that 19 current GCMs consistently under-predict the enhanced Saharan vegetation coverage during the middle Holocene period suggested by paleorecords (see previous chapter). Betts *et al.* (2003) attribute some of the local differences in the vegetation to inadequate representation of natural disturbances (e.g. fire).

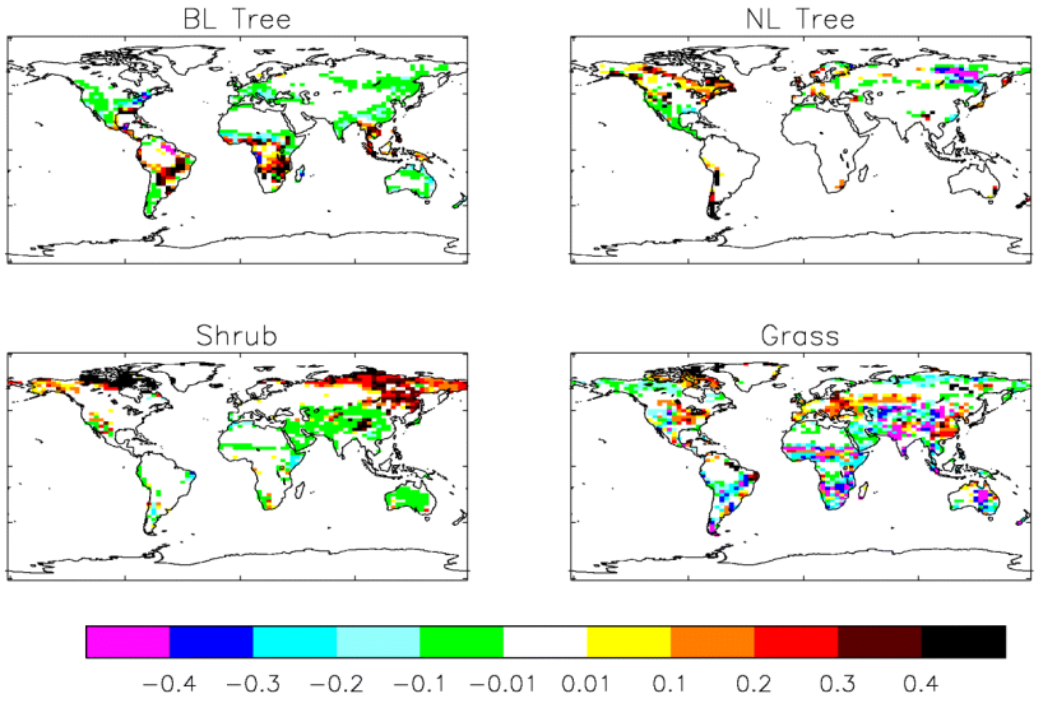

Figure 2.7 *Agreement of simulated vegetation fractional coverages with IGBP satellite observations Loveland* et al. *(2000). C3 and C4 grasses have been combined into a single prediction of grass distribution. The plots show differences in the fractional coverage (model-IGBP). This figure is reproduced from Betts* et al. *(2003).*

The El Niño Southern Oscillation (ENSO) is a major mode of climate variability (Jones *et al.* (2001)). Jones *et al.* (2001) show that HadCM3LC is able to reproduce the observed ENSO variability in atmospheric CO_2. Collins *et al.* (2000) show that the spectral profile of surface temperature in HadCM3LC is consistent with observations over wavelengths of 1-10 years. HadCM3LC is HadCM3L with fully coupled atmosphere, ocean, and terrestrial carbon cycle models. Figure 2.8 compares the variability of surface temperature in HadAM3LC against

observations, and is reproduced from Collins *et al.* (2000).

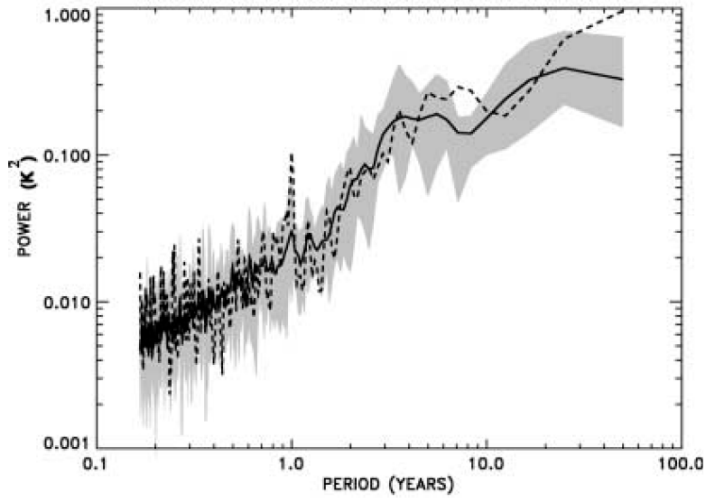

Figure 2.8 *Evaluation of the spectrum of variability of HadCM3 surface temperature against observations (Jones (1994), Parker* et al. *(1995)). This figure is reproduced from Collins* et al. *(2000). The shaded region shows the range of powers computed for HadCM3, whilst the solid line is the mean HadCM3 power. The dashed line shows the observations.*

2.5 Exploratory experiments

Two standard perturbation experiments routinely performed with GCMs, and which are relevant to the land surface model, are described here: the effects of global bare soil (e.g. Betts (1999), Kleidon *et al.* (2000)), and the equilibrium response of the GCM to a doubling of CO_2 (e.g. LeTreut and McAvaney (2000), Williams *et al.* (2001)). Modelling the effects of global bare soil estimates the maximum impact of changes in vegetation distributions. The equilibrium response to a doubling of CO_2 estimates how the GCM will respond to future CO_2 levels. However these two experiments are not usually performed in the same study. It is useful to perform the experiments in the same study because this allows direct inter-comparisons to be made, and because it is expected that the results will have some model bias. These two perturbation experiments (referred to as BS and 2CO2 hereafter) are compared with a control run (CTL) for

reference and a third experiment combining both perturbations (2CBS). The investigation of the equilibrium response of vegetation can then be further investigated by combining the analysis of all of these experiments. This analysis serves as an introduction to the vegetation behaviour.

All four of the experiments use HadSM3 with modern heat convergences prescribed in the slab ocean. HadSM3 is run at the standard 2.5^o latitude by 3.75^o longitude atmospheric resolution. A constant atmosphere CO_2 level was used for all experiments, 287 ppmv was taken for the CTL CO_2 levels, and 574 ppmv for 2CO2 conditions. Assuming a constant CO_2 level means that these simulations ignore carbon cycle feedbacks. Vegetation structure is allowed to vary dynamically in CTL and 2CO2 using the MOSES2 surface exchange scheme. The CTL and 2CO2 experiments are integrated for 100 years, until the terrestrial carbon cycle had reached a steady state. BS and 2CBS experiments did not require such a long spin up period because there is no biosphere. In these experiments HadSM3 had reached a steady state after 30 years. Climate plots show 20 year averages, taken after the climate system had been satisfactorily spun up. The four experiments are summarised in table 2.1.

Experiment	CO_2 (ppmv)	Surface conditions	Length of run (years)
CTL	287	dynamic vegetation	120
BS	287	global desert	50
2CO2	574	dynamic vegetation	120
2CBS	574	global desert	50

Table 2.1 *The experimental setup for each of the four exploratory experiments.*

The initial atmospheric states of the different experiments were form other GCM experiments. The CTL initial conditions came from previous control simulations, where the land surface conditions had been initialised using the Wilson and Henderson-Sellers (1985) data set. The other GCM experiments were initialised with the final atmospheric state from the CTL experiment. The length of the CTL experiment was required because of the time taken to come to equilibrium for the particular choice of model setup used here. BS and 2CO2 experiments were initialised form the CTL experiment to avoid this requirement. The 2CBS experiment was initialised from the final state of the BS experiment. The particular initial state

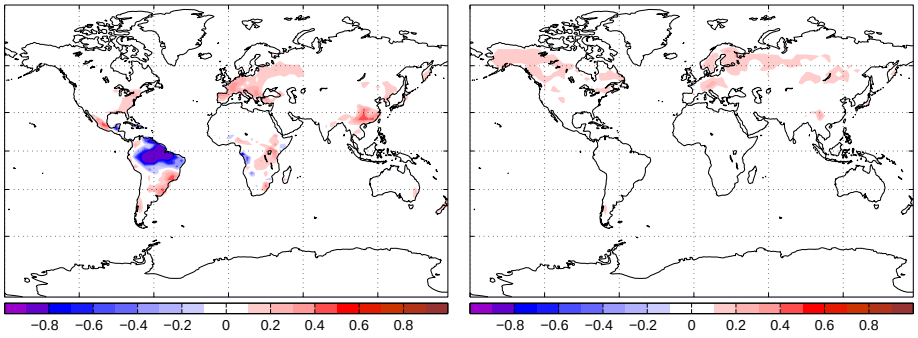

(a) Broadleaf tree (b) Needleleaf tree

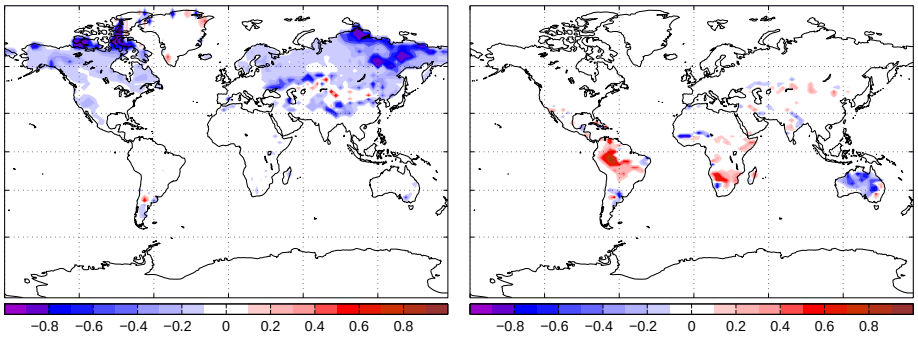

(c) C3 type grass (d) C4 type grass

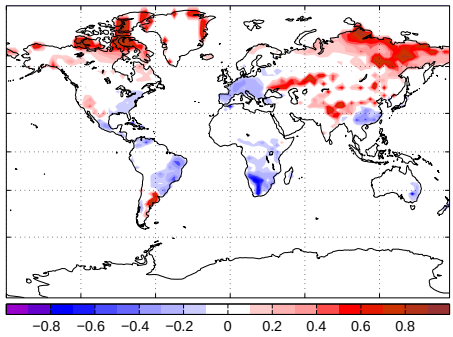

(e) Shrub

Figure 2.9 *Differences in vegetation fractional coverage. The plots show doubled CO_2 equilibrium vegetation (2CO2) minus pre-agricultural control (CTL). Negative anomalies indicates greater vegetation fractional coverage in CTL than in the 2CO2 experiement.*

used for the 2CBS experiment may be important if using the BS state modifies the response of the GCM to a doubling of atmospheric CO_2 , however this will not be investigated further here.

2.5.1 Sensitivity to atmospheric CO_2

In order to estimate the equilibrium sensitivity of HadSM3 to CO_2 experiments $2CO_2$ and CTL were performed. Figure 2.9 shows the changes in equilibrium vegetation coverages resulting from a doubling of atmospheric CO_2 concentration. Comparing the vegetation structure in 2CO2 and CTL, in fig. 2.9, we see that there are significant differences in vegetation structure. A prominent feature of 2CO2 experiment is the continental-scale reduction in Amazon broadleaf tree coverage which is partially replaced with C4 type grass. The loss of the Amazon forest is an important feature of current GCM prediction for future climate (e.g. White *et al.* (1999), Betts *et al.* (2003)) and was discussed in the previous chapter. Figure 2.9 suggests that the Amazon forest loss is a relatively robust aspect of the Hadley model and does not depend on the dynamic ocean or the precise scenario of future CO_2 concentrations. Broadleaf tree coverage increases in boreal regions, as does needleleaf tree and is consistent with a warming in these regions. C3 grass coverage is reduced globally as a result of large increases in shrub coverage. C4 grass coverage is greatly reduced over Australia, whilst increasing in other regions (South America and South Africa). Shrub coverage also declines in South America and East Australia.

The sensitivity of the temperature and precipitation fields to a doubling of CO_2 with vegetation included is shown in figs. 2.11(a) and 2.10(a). Temperatures universally increase in response to the doubling of CO_2, however the largest change in surface temperature is associated with the Amazon die-back. Temperature changes in the region of the Amazon die-back are approximately 20 K. The Amazon die-back is also associated with a local reduction of precipitation in excess of 1 mm day^{-1}. These changes combine the primary effects of doubling CO_2 and the positive feedback of the Amazon die-back.

2.5.2 Bare soil simulation

Using static vegetation structure and a previous version of the Hadley Centre GCM (HadCM2), Betts (1999) showed that vegetation alters global climate such that climate is more suitable for vegetation growth, for the present-day. This study analysed the climate change resulting from a global bare soil simulation and the resulting changes in vegetation structure which were predicted offline. Analysing the resulting changes in vegetation showed that vegetation feedbacks on climate allowed more vegetation to exist.

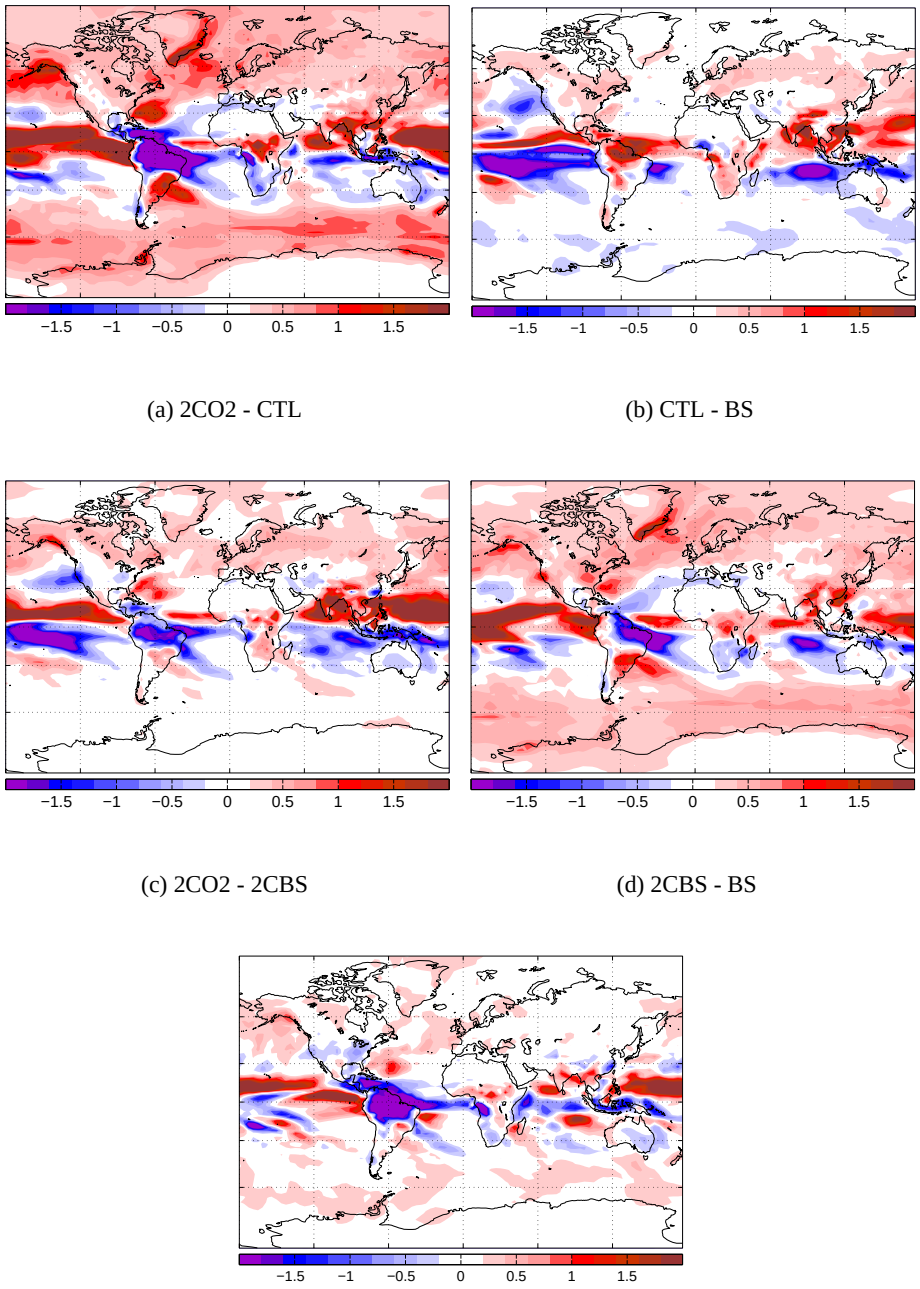

(a) 2CO2 - CTL

(b) CTL - BS

(c) 2CO2 - 2CBS

(d) 2CBS - BS

(e) (2CO2 - CTL) - (2CBS - BS)

Figure 2.10 *Annual mean precipitation difference fields mm day^{-1}. a) The effect of doubling CO_2 levels on the climate. b) The effect of doubling CO_2 on the climate, without vegetation. c) The impact of global bare soil conditions d) The impact of global bare soil conditions, under doubled CO_2 levels. e) The impact of vegetation on the response of the climate system to a doubling of CO_2.*

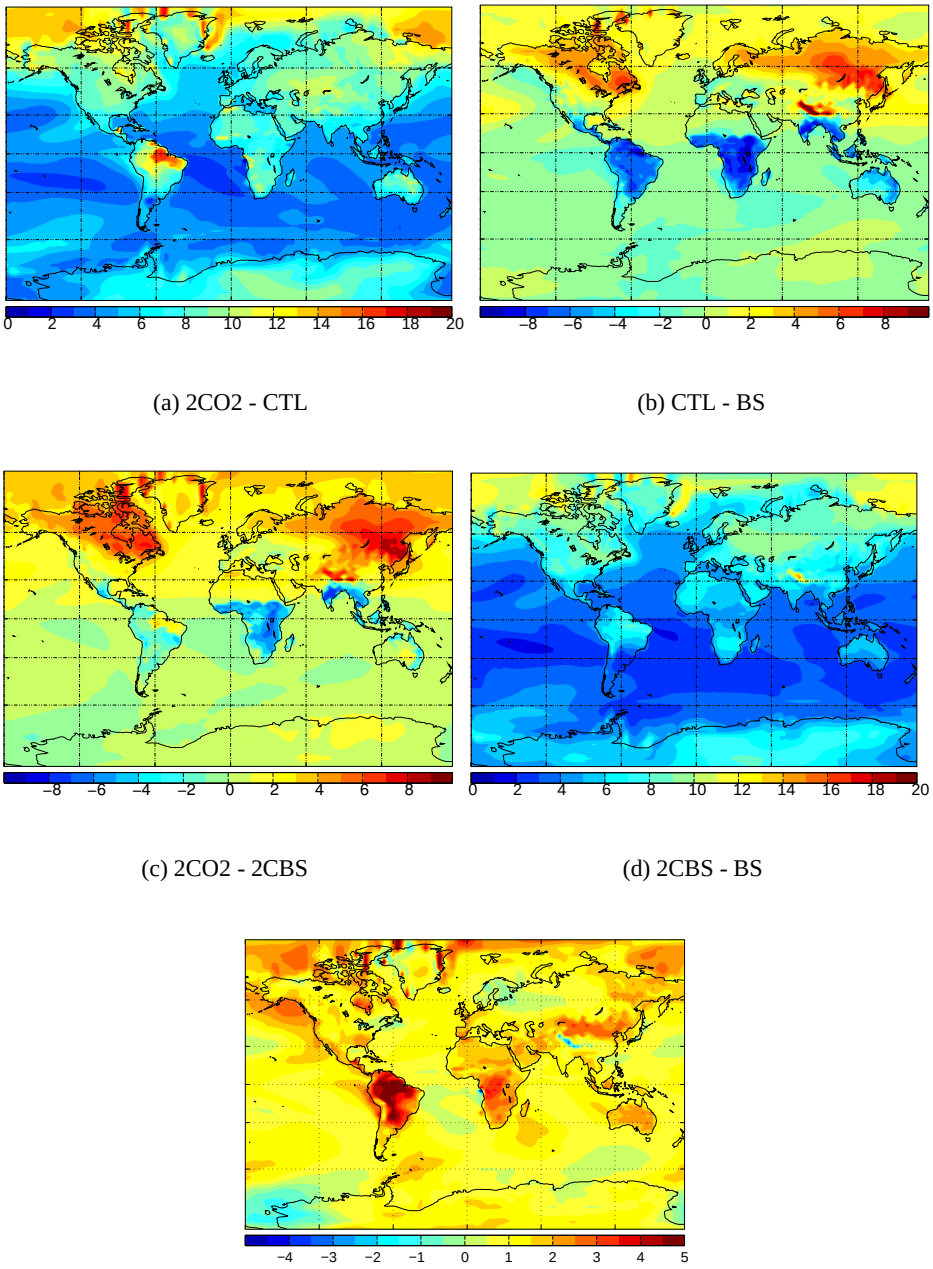

(a) 2CO2 - CTL

(b) CTL - BS

(c) 2CO2 - 2CBS

(d) 2CBS - BS

(e) (2CO2 - CTL) - (2CO2$_{(BS)}$ - BS)

Figure 2.11 *Differences in annual mean surface temperature fields (^{o} C). a) The effect of doubling CO_2 levels on the climate. b) The effect of doubling CO_2 on the climate, without vegetation. c) The impact of global bare soil conditions. d) The effect of doubling CO_2 under global bare soil conditions. e) The impact of vegetation on the response of the climate system to a doubling of CO_2.*

Betts (1999) used TRIFFID offline, but here TRIFFID is used within the GCM. In the bare soil experiments presented here the atmosphere "sees" bare soil conditions and the vegetation structure is held at global bare soil conditions, however the photosynthesis model still calculates the NPP values consistent with the environment, which could potentially drive the expansion of vegetation if vegetation were allowed to re-grow.

The modification of climate by vegetation is shown here as the difference in surface temperature and precipitation fields (CTL-BS) in figs. 2.10(b) (precipitation) and 2.11(b) (surface temperature). The patterns of change are similar to those simulated by Betts (1999). However the regional changes in temperature are twice the magnitude in fig. 2.11(b) than in Betts (1999). This difference is not surprising as Betts (1999) use a different model (HadCM2) to the model used here (HadSM3) which leads to different climate predictions. The differences may also be the result of the different modelling approaches to simulating the ocean (HadCM2 uses a dynamic ocean model, whilst HadSM3 uses a thermodynamic slab ocean model).

The global mean land surface levels of precipitation and 1.5 m air temperature are summarised for the different GCM experiments (including results from Betts (1999)) in table 2.2. In all sets of experiments, vegetation acts to increase the mean precipitation over land. In Betts (1999) the effect of vegetation on air temperature is a slight cooling over land (-0.4 K), whilst in CTL-BS the effect is a slight warming (0.4 K). These values are the residual of regional differences and are therefore probably not significant. When the impact of vegetation under 2CO2 is investigated, the mean warming over the land surface is substantial (2.2 K).

The mean land surface net primary productivity, unweighted by fractional coverage is given for each plant functional type in table 2.3 for the four experiments presented here. The values presented in table 2.3 illustrate how climatic changes alter the photosynthetic potential of each PFT, i.e. it shows the mean NPP that would result from uniform coverage of that PFT. Under both 287 ppmv and 574 ppmv the potential NPP is greater in the vegetated simulation than the desert climate system simulation. Table 2.3 shows that the effects of doubling CO_2 is a global increase in broadleaf tree NPP, and a global reduction in needleleaf tree NPP. C3 and C4 type

grasses both increase NPP as a result of doubling CO_2, and the increase of C4 NPP is larger than that of C3 NPP. The potential NPP of shrub is also increased.

Betts (1999) did not assess how increasing CO_2 levels affects the self-beneficial behaviour of vegetation. The effect of vegetation feedbacks on climate with doubled CO_2 is shown for precipitation in fig. 2.10(c), and for surface temperature in fig. 2.11(c). In the 2CO2 experiment much of the Amazon forest has been lost, along with other changes in the land surface composition (see previous description). The cooling effect of South African vegetation is also reduced. There is also a difference in Northern Hemisphere boreal temperatures, where vegetation acts to warm this region in $2CO_2$ relative to 2CBS. The conclusion from the experiments presented here is that the self-beneficial effects of vegetation are reduced under elevated CO_2, largely as a direct result of the simulated Amazon die-back.

	NOVEG	VEG	BS	CTL	2CBS	2CO2
1.5 m Temperature (K)	280.95	280.53	279.20	279.61	285.53	287.69
Precipitation (mm day^{-1})	1.91	2.19	1.77	1.97	1.95	2.06

Table 2.2 *Changes in the annual mean climate over the land surface. NOVEG and VEG from Betts (1999) are equivalent to BS and CTL experiments respectively.*

	Broad leaf tree	Needle leaf tree	C3 type grass	C4 type grass	Shrub
CTL	0.2541	0.1940	0.4345	0.5959	0.2533
BS	0.0140	0.0458	0.1244	0.5034	0.0953
2CO2	0.2780	0.1381	0.4469	0.8157	0.2929
2CBS	0.0794	0.0379	0.1565	0.5025	0.1443

Table 2.3 *NPP on PFT (kg C m^{-2} year^{-1}) for the different GCM experiments.*

2.5.3 Combined effects

In order to estimate the effects of the combination of doubled CO_2 and global bare soil conditions the GCM response to doubling CO_2 level experiment is repeated, with vegetation held at global desert conditions (the 2CBS experiment). Figures 2.10(d) and 2.11(d) show the response of the desert climate system to a doubling of CO_2, in terms of precipitation and surface temperature changes. In the absence of vegetation the drying effect of doubling CO_2 over the Amazon is reduced; the large warming associated with the Amazon die-back is also lost, because the local climate is already warmer and drier in the BS experiment. The difference in the global climate response to CO_2 with and without vegetation is shown in figs. 2.10(e) and 2.11(e). The strongest change in precipitation is associated with the Amazon die-back. The temperature response to the CO_2 doubling is increased when vegetation is included.

The equilibrium response of a GCM to a doubling of CO_2 is a standard experiment, and is sometimes quoted for a GCM as a measure of its general sensitivity (e.g. Renssen *et al.* (2003b)). The response to a doubling of CO_2 provides a means of comparing the sensitivity of GCMs. Figure 2.12 plots the sensitivity of HadSM3 to a doubling of CO_2 and the predicted equilibrium response from 9 other GCMs which also use slab ocean models (these 9 other GCM sensitivities are taken from LeTreut and McAvaney (2000)). The HadSM3 response to a doubling of CO_2 was calculated by differencing 2CO2 and CTL experiments. The response of HadSM3 to a doubling of CO_2 in the absence of vegetation was estimated from 2CBS-BS. Figure 2.12 shows that HadSM3 is more sensitive to a doubling of CO_2 than any of the other GCMs considered, including a previous version of the Hadley Centre GCM, UKMO. Spatial plots of the surface climate response of HadSM3 to a doubling of CO_2 (figs. 2.10(a) and 2.11(a)) show that the largest change in climate is associated with the Amazon die-back. However whilst the Amazon die-back acts to increase the predicted change in temperature the Amazon die-back reduces precipitation and the other changes predicted cover a much larger proportion of the globe and dominate. The change in sensitivity due to the inclusion of vegetation is shown in figs. 2.10(e) and 2.11(e). Figures 2.10(e) and 2.11(e) show that vegetation increases the sensitivity of the Amazon land surface. This is also seen over the African continent, though the effect is not as strong. By plotting the equilibrium response of HadSM3 with global bare soil, the natural

response of the GCM in the absence of vegetation can be estimated. Figure 2.12 shows that even in the absence of vegetation, HadSM3 is the most sensitive GCM (equally sensitive as the CSIRO GCM). Including vegetation, however, increases the sensitivity of the GCM.

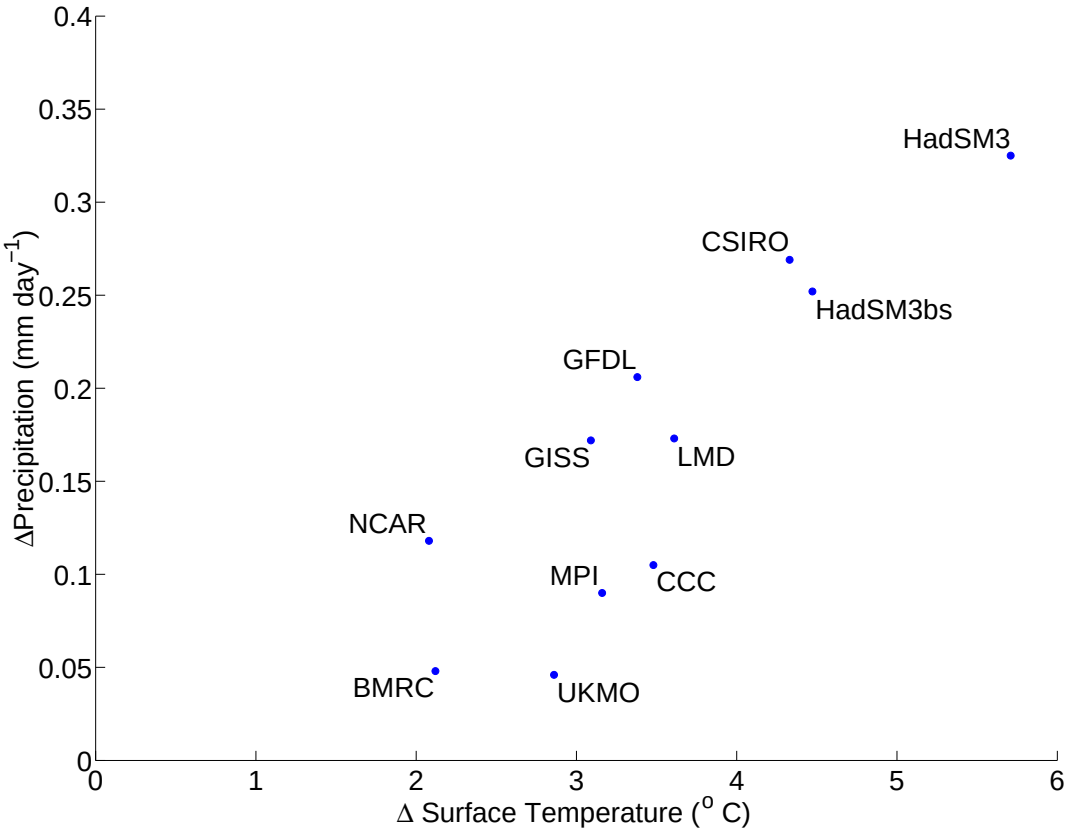

Figure 2.12 *Inter-comparison of the equilibrium sensitivity of GCMs to a doubling of CO_2. HadSM3 and HadSM3bs (HadSM3 without vegetation) values were taken from experiments described here, the other 9 GCM responses are reproduced from LeTreut and McAvaney (2000). All the GCMs used slab ocean models.*

2.6 Summary

In this chapter the GCM model that will be used in the following chapters has been described. The discussion of HadSM3 has focussed on those aspects of the model affecting the land surface and the terrestrial carbon cycle. Validations of the model have been presented both from previous studies and performed as part of this thesis. Importantly several model biases have been diagnosed in the simulation of the land surface climatology relative to the Legates and Willmott (1990) observation data set. The limitations of the ocean model have been discussed, relative to a more detailed representation of ocean dynamics. The land surface processes have been described in detail, and a discussion of the implications of the assumptions made in formulating the model has been included. Existing validations of MOSES2 have been reviewed, which assess the ability of MOSES2 to simulate short-term land-air fluxes, and the ability of MOSES2 to predict pre-agricultural equilibrium distributions.

A series of equilibrium experiments has been presented here investigating the sensitivity of HadSM3 to a doubling of CO_2, and the maximum impact of reductions in vegetation structure (global bare soil). The sensitivity of HadSM3 to a doubling of CO_2 has been shown to be greater than 9 other GCMs. The self-beneficial effects of vegetation, first demonstrated by Betts (1999), has been reproduced here. The self-beneficial effects has also been shown to be reduced under elevated CO_2 levels. This reduction in the self-beneficial effects of vegetation is partially due to the fact that the simulation of climate under doubled CO_2 predicts a die-back of the Amazon tree coverage. In the experiments presented here the equilibrium effects of the Amazon die-back simulated by HadSM3 was investigated. The Amazon die-back simulated by HadSM3 is an example of dynamic vegetation behaviour on a continental scale. Understanding the dynamics of the vegetation model will lead to an improved understanding of such phenomena. It may also provide insight into the general coupling between vegetation and atmosphere.

In the remaining chapters the dynamic behaviour of the global vegetation model will be investigated. In chapter 3 a simplified form of TRIFFID is derived and the dynamic properties are investigated. In chapters 4 and 5 the dynamic behaviour of global vegetation is investigated

within HadSM3.

CHAPTER 3

Simplified TRIFFID model approach

3.1 Introduction

The TRIFFID model couples a photosynthesis model (Cox *et al.* (1998)) to a population model, and updates the fractional coverage and height of vegetation depending on the predicted photosynthesis. The TRIFFID model is described by Cox (2001). The previous chapter discussed the photosynthesis model and the way that environmental conditions are translated into predicted net primary productivity (NPP) rates. This chapter will investigate the population model, and derive a simpler version which helps give greater insight into the fundamental processes and interactions.

In section 3.2 standard analysis of the type of population model (Lotka-Volterra competition equations) is reproduced. This is then linked to the TRIFFID model parameters. The diffusive Lotka-Volterra competition equations are also investigated, and these results are then linked to the TRIFFID model. Analysis of the Lotka-Volterra competition equations is not new, but it is necessary to reproduce it here, to be able to investigate the TRIFFID equations. Few textbooks contain the analysis of the diffusive equations, but it is a very simple addition to the investigation of the non-diffusive equations. In section 3.3 the assumption of a single plant functional type is tested. Using simulated plant functional type distributions from the pre-agricultural control climate (see chapter 2) the mutually exclusive nature of competing plant functional types is demonstrated. In section 3.4 the simplified form of TRIFFID is derived. In section 3.5 the ability of the simplified form of TRIFFID to predict the vegetation dynamics is verified, and in section 3.6 the steady state solution of the simplified TRIFFID model is discussed. In the next section the initial growth rate of the simplified TRIFFID model is analysed. In section 3.8 the maximum rate of expansion of fractional coverage is derived, and the stability of the model is discussed. Internal variability and the interaction with stochastic forcing is analysed in section 3.9. In section 3.10

the re-growth timescale of needleleaf tree PFT is compared with the recovery of real forest to a grid box scale perturbation. The extent that the simplified model captures the behaviour of the full TRIFFID model and the lessons learnt from the whole chapter will be discussed in section 3.11.

Using a similar approach, Huntingford *et al.* (2000) present a simplified version of the terrestrial carbon cycle. Huntingford *et al.* (2000) also reduce the vegetation dynamics to a single plant functional type (assumed to be a tree PFT). The model of Huntingford *et al.* (2000) incorporates a representation of soil carbon dynamics and photosynthesis. As a result of this approach, Huntingford *et al.* (2000) focus on simulating the response to increasing CO_2 levels. Whilst the study of Huntingford *et al.* (2000) focussed on the impact of environmental change, the simplified model presented here will be used to investigate the dynamical properties of the vegetation model, interpreting the results of this to help understand how the vegetation model behaves in the full GCM system. Several of the assumptions made by Huntingford *et al.* (2000) and also in this chapter are evaluated here. The links between the simplified model presented here and the full complexity TRIFFID model are made explicit, and the ability of the simplified model to capture the behaviour of TRIFFID is tested; this was not performed by Huntingford *et al.* (2000). In the next chapter the TRIFFID model is investigated within a full GCM system, allowing vegetation to dynamically interact with the atmosphere. The results from this chapter will help in the interpretation of this simulation.

3.2 Competition solution

In this section the now classic analysis of Lotka-Volterra competition equations is reproduced (see Case (2000) pp. 316-327). This analysis is then related to the specific case of the TRIFFID model. The Lotka-Volterra analysis is then extended to consider diffusive Lotka-Volterra competition equations. One modification to the Lotka-Volterra equations is to introduce the effects of harvesting. This is a steady reduction in population and is usually either a constant rate or proportional to the population size. If the decrease in population size is greater than a

population's ability to increase, then the population size will decrease towards extinction. For this reason Lotka-Volterra competition equations including the effects of grazing are said to be diffusive (Case (2000), p. 137). The TRIFFID model is based on diffusive Lotka-Volterra competition equations. The original Lotka-Volterra competition equations for two species are given by eqns. 3.1 and 3.2 (*e.g.* Gotelli (1998),p. 101).

$$\frac{dN_1}{dt}\frac{1}{N_1} = \frac{r_1}{K_1}(K_1 - N_1 - c_1 N_2) \tag{3.1}$$

$$\frac{dN_2}{dt}\frac{1}{N_2} = \frac{r_2}{K_2}(K_2 - N_2 - c_2 N_1) \tag{3.2}$$

N_1 and N_2 are population sizes for two competing species (*e.g.* between grasses). Coefficients c_1 and c_2 are the competition coefficients, and quantify the ability of one species to restrict the expansion of another species. r_1 and r_2 are the intrinsic growth rates for N_1 and N_2 respectively. K_1 and K_2 are the maximum magnitudes of N_1 and N_2 that can be supported by their environment.

In TRIFFID, shrub dominates grasses (i.e. it always displaces grass fractional coverage). Trees dominate both grasses and shrub. However between plant functional types on the same level of this dominance hierarchy competition is resolved with Lotka-Volterra competition for space. To derive the possible solutions of the Lotka-Volterra competition equations we consider the necessary conditions under which a population will persist under the least favourable conditions possible in the Lotka-Volterra equations. For species N_1 this is when $N_2 \sim K_2$, and N_1 is close to 0, *i.e.* the conditions (dN_1/dt)(1/N_1) > 0, when N_1 tends to zero, and N_2 tends to K_2. Then we have

$$\frac{dN_1}{dt}\frac{1}{N_1} \approx \frac{r_1}{K_1}(K_1 - 0 - c_1 K_2) \tag{3.3}$$

For $\frac{dN_1}{dt}\frac{1}{N_1} > 0$, since $r_1 > 0$ by definition, we get eqn. 3.4.

$$\frac{K_1}{K_2} > c_1 \tag{3.4}$$

By considering what conditions are required for N_2 to expand, when $N_1 = K_1$ and N_2 is close to 0 we get inequality (3.5).

$$\frac{K_2}{K_1} > c_2 \tag{3.5}$$

Now each inequality (eqns. 3.4 and 3.5) is either satisfied, or not, generating 4 possible combinations.

Case 1: N_2 does not satisfy eqn. 3.5, and will not persist, but N_1 satisfies eqn. 3.4 and persists. This leads to the case where N_1 out-competes N_2 with the steady state solution $N_1 = K_1$, $N_2 = 0$, fig. 3.1(a).

Case 2: The reverse of Case 1 , N_2 satisfies eqn. 3.5, but N_1 doesn't satisfy equality 3.4, leading to the solution N_1=0, N_2=K_2, fig. 3.1(b)

Case 3: Both N_1 and N_2 persist as equality 3.4 and 3.5 are both satisfied, and a stable co-existence is reached, fig. 3.1(c).

Case 4: Neither eqn. 3.4 3.5 are satisfied, and N_1 and N_2 are in unstable equilibrium, fig. 3.1(d).

Exact solutions of the Lotka-Volterra competition equations are found when the time derivatives of the Lotka-Volterra competition equations are set to zero. This leads to eqns. 3.6 and 3.7

$$N_1 = K_1 - c_1 N_2 \tag{3.6}$$

$$N_2 = K_2 - c_2 N_1 \tag{3.7}$$

Then the four different cases simply refer to the 4 different ways of plotting the two solution lines.

In fig. 3.1 the arrow triplets show the direction both the populations move in, for a specific region of the graph. To the right of the steady state line for N_1, $N_1 > K_1$, i.e. the population of N_1 is

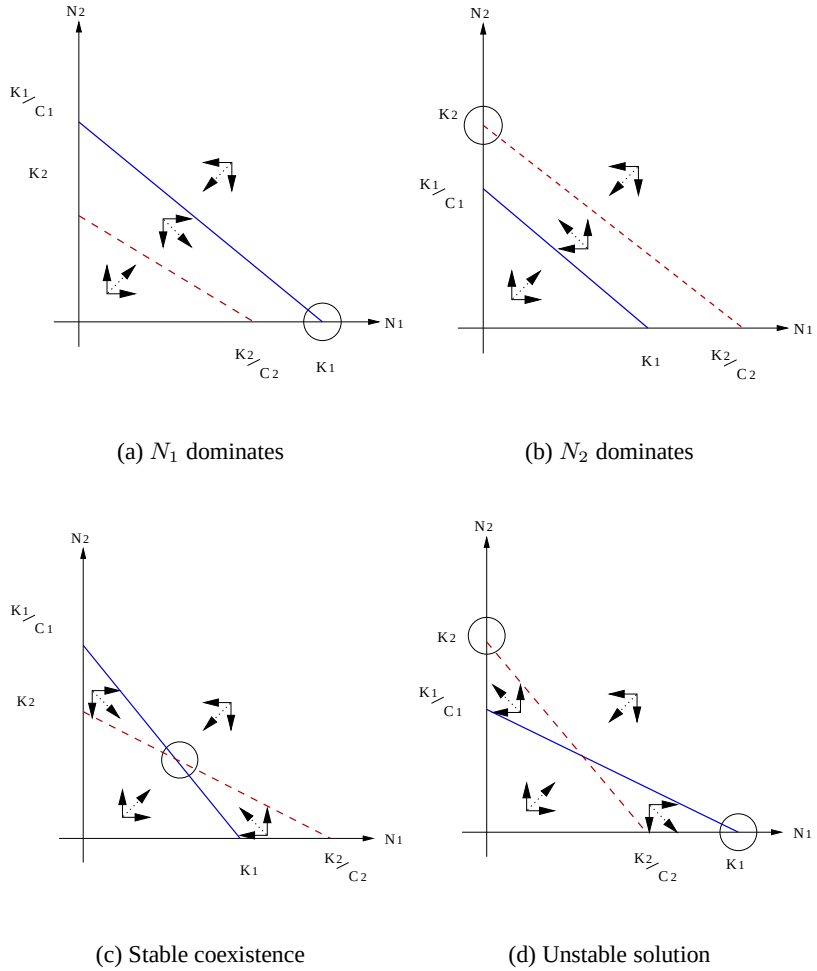

(a) N_1 dominates (b) N_2 dominates

(c) Stable coexistence (d) Unstable solution

Figure 3.1 *The four possible solutions of the Lotka-Volterra model. The lines correspond to the equilibrium solutions of the Lotka-Volterra model. The solid, blue line is the equilibrium solution for species N_1. The dashed, red line is the equilibrium solution for species N_2. The circles indicate the final solution in each case. Reproduced from Gotelli (1998), pp. 107-114. The x-axis shows the magnitude of population N_1. The y-axis shows the magnitude of population N_2. The arrow triplets indicate the direction of change of both populations, in a particular region of the graph. The dotted arrow in the triplet indicates the net movement on the graph.*

too large to be supported, and N_1 decreases (moves to the left). Therefore the plots allow the behaviour to be predicted for any point on the N_1,N_2 plane.

The TRIFFID model is constrained to case 3 by the following assumptions (which are built into TRIFFID): c_1 and c_2 are always less than 1.0, and K_1 = K_2. As $\frac{K_1}{K_2}$ = 1, and c_1 is < 1 eqn. 3.4 is satisfied. $\frac{K_2}{K_1}$ = 1 and $c_2 < 1$, satisfying eqn. 3.5, so we have the case of stable co-existence. In the TRIFFID model setup non-diffusive Lotka-Volterra competition equations must be constrained to case 3 because the total fractional coverages must sum to 100 %, and dominant PFTs impose the same reduction in space for both of the two competing species. If, however, competition were for something other than fractional coverage these assumptions might not necessarily apply, and other cases would be possible.

The above analysis ignored diffusion. TRIFFID uses a diffusive version of the Lotka-Volterra competition equations, which become:

$$\frac{dN_1}{dt}\frac{1}{N_1} = \frac{r_1}{K_1}(K_1 - N_1 - c_1 N_1) - \gamma_1 \quad (3.8)$$

$$\frac{dN_2}{dt}\frac{1}{N_2} = \frac{r_2}{K_2}(K_2 - N_2 - c_2 N_2) - \gamma_2 \quad (3.9)$$

and the inequalities 3.4 and 3.5 become :

$$\frac{K_1}{K_2} > c_1 + \frac{\gamma_1}{r_1}\frac{K_1}{K_2} \quad (3.10)$$

$$\frac{K_2}{K_1} > c_2 + \frac{\gamma_2}{r_2}\frac{K_2}{K_1} \quad (3.11)$$

γ is the natural disturbance rate, including such effects as fire and herbivory. Constraining these inequalities to the properties of TRIFFID, using the same assumptions as the non-diffusive case, the inequalities become:

$$1 - \frac{\gamma_1}{r_1} > c_1 \quad (3.12)$$

$$1 - \frac{\gamma_2}{r_2} > c_2 \quad (3.13)$$

The equilibrium solutions of the diffusive Lotka-Volterra equations are :

$$N_1 = K_1(1 - \frac{\gamma_1}{r_1}) - c_1 N_2 \quad (3.14)$$

$$N_2 = K_2(1 - \frac{\gamma_2}{r_2}) - c_2 N_1 \quad (3.15)$$

The effect of diffusion is to force a translation of the solution lines, parallel to the axis. It has now been shown that for the non diffusive case, constraining the Lotka-Volterra competition equations to the TRIFFID choice of parameters forces stable coexistence of the two species. As can be seen from eqns. 3.12 and 3.13, when $r_1 >> \gamma_1$ and $r_1 >> \gamma_2$ the diffusive TRIFFID model is constrained to the case of stable coexistence. When these inequalities are not satisfied the other three cases are also possible.

When the two equalities are met, and there is stable coexistence, N_1 and N_2 are given by eqns. 3.16 and 3.17

$$N_1 = [K_1(1 - \frac{\gamma_1}{r_1}) - c_1 K_2(1 - \frac{\gamma_2}{r_2})](1 - c_1 c_2)^{-1} \quad (3.16)$$

$$N_2 = [K_2(1 - \frac{\gamma_2}{r_2}) - c_2 K_1(1 - \frac{\gamma_1}{r_1})](1 - c_1 c_2)^{-1} \quad (3.17)$$

When eqns. 3.12 and 3.13 are not both met then either $N_1 = K_1(1 - \frac{\gamma_1}{r_1})$ or $N_2 = K_2(1 - \frac{\gamma_2}{r_2})$, depending on which of the inequalities is satisfied, and the other fractional coverage is at most that which can exist in the space left by the dominant species, N_2 = 1 - K_1(1-$\frac{\gamma_1}{r_1}$), or N_1 = 1 - K_2(1-$\frac{\gamma_2}{r_2}$).

3.3 The 1-species assumption

In the rest of this chapter we investigate the properties of a single species version of TRIFFID. This is equivalent to assuming that grid boxes are dominated by only one PFT of a competing pair of PFTs (*e.g.* broadleaf and needleleaf trees.). The previous section showed that the Lotka-Volterra competition equations do not exclude the possibility of coexistence, but the physical parameters of the different PFTs suggest that they may thrive in different environments (see chapter 2). In order to justify the assumption of a single, dominant fractional coverage of vegetation, the simulated pre-agricultural vegetation is analysed (see chapter 2 for details of the pre-agriculture simulation, CTL). If vegetation is mutually exclusive, then in a scatter plot of the two fractional coverages, the points will lie on the axis. The further from the axis the points are, the less reliable is the assumption of a single dominant species.

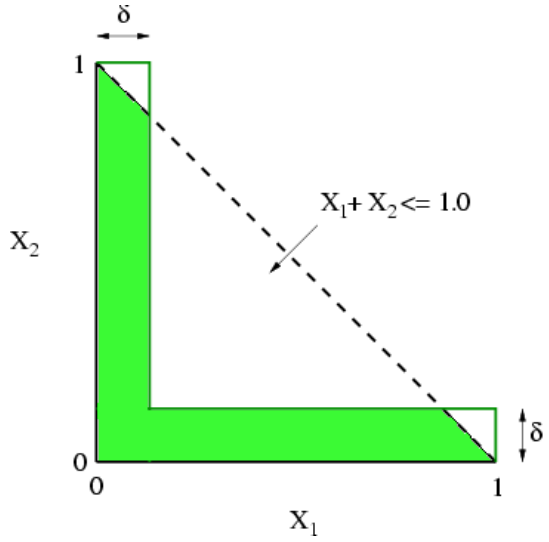

Figure 3.2 *Delta function. X_i is the fractional coverage of species i. The Triangular region, bounded by the points [(0,0), (0,1), (1,0)] is the range of possible combinations of X_1, and X_2. The ratio of the number of points within the green shaded region to the total number of points is calculated. When δ is small only points that are approximately [X_1,0] or [0, X_2] are in the green region.*

In order to quantify the validity of the single species assumption the number of points found within a region, δ, of the axes is calculated and expressed as the ratio to the total number of points. This ratio is calculated for δ ranging between zero and 0.5 (when it includes all the possible space), and is illustrated in fig. 3.2. It can be shown that if the points are uniformly distributed then the ratio of points within the δ region (equivalent to the area of the region) to the total number of points (or area) is equal to $1-(1-2\delta)^2$, neglecting the effects of diffusion, which varies from grid box to grid box.

Discounting zero coverage grid boxes produces four datasets of pre-agricultural fractional coverages, of 2,381 points. These datasets actually incorporate a total of 2,571,480 data points as the pre-agricultural vegetation is a mean of 30 years of data, at 10 day resolution. Plots of the ratio of points within the δ region to the total number of plots are shown for the grasses and the trees in fig. 3.3. Figure 3.3 also plots the uniform distribution assumption, $1-(1-2\delta)^2$, for comparison.

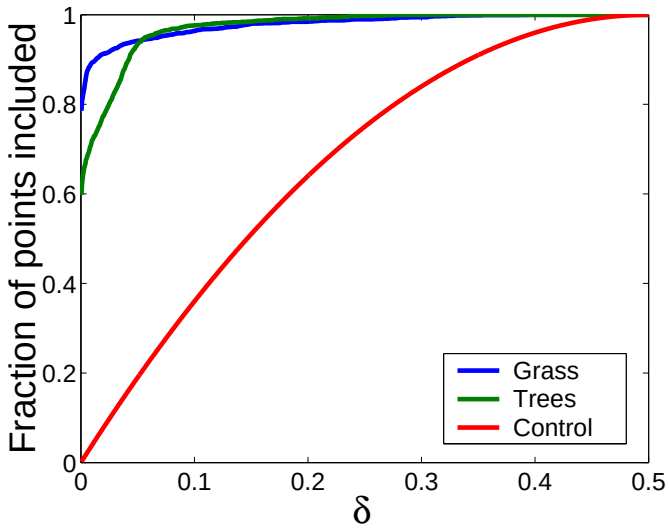

Figure 3.3 *The δ test for simulated coexistence, for the grass PFTs (blue line), and the tree PFTs (green line). Also shown is is the control ratio (red line), i.e. how the fraction would increase as a function of δ if the fractional coverages were uniformly distributed.*

Figure 3.3 shows that the distribution of points is significantly clustered around the axis, i.e. for the simulation of steady state, pre-agriculture vegetation, vegetation is largely either C3 or C4 type grass, or either broadleaf or needleleaf tree, at a particular grid box. Figure 3.3 suggests that the assumption of a single dominant plant functional type is reasonable. For pre-agricultural grasses, 96 % of grass is found within the $\delta = 0.05$ region. For tree plant functional types, 94% is found within the $\delta = 0.05$ region. Figure 3.3 shows that if the plant functional types were uniformly distributed this percentage would be close to 20 %.

3.4 Derivation of simplified TRIFFID

Having justified the assumption of single PFT, in this section the simplified TRIFFID model is derived. The litterfall rate, Λ_l, and the disturbance parameter, γ_ν are assumed to be a constant.

By reducing the TRIFFID model to a single PFT, we restrict the use of the simplified model to predicting the behaviour of the dominant PFT.

The main dynamic vegetation equations in the TRIFFID model represent the balance between increasing vegetation carbon density and increasing fractional coverage. The equations are:

$$\frac{dC_\nu}{dt} = (1-\lambda)\Pi - \Lambda_l \tag{3.18}$$

$$C_\nu \frac{d\nu}{dt} = \lambda \Pi \nu_* (1 - \sum_j c_{ij}\nu_j) - \gamma_\nu \nu_* C_\nu \tag{3.19}$$

C_ν is the vegetation carbon density of the PFT, Π is the NPP, Λ_l is the litterfall rate on PFT, and represents the loss of carbon matter resulting from the natural life cycle of the vegetation. ν_i is the fractional coverage of PFT i. ν_* is the fractional coverage of PFT i, if ν_i ¿ 0.001 %, otherwise ν_* = 0.001 %. γ_ν is a disturbance parameter and implicitly incorporates the effects of mortality arising from processes other than competition with other PFTs, *e.g.* fire, disease, and herbivory into TRIFFID. λ is defined in expression 3.20. λ controls the partitioning of NPP between increasing the fractional coverage and increasing the carbon density.

$$\lambda = \begin{cases} 1 & \text{for } L_b > L_{max} \\ \frac{L_b - L_{min}}{L_{max} - L_{min}} & \text{for } L_{min} < L \leq L_{max} \\ 0 & \text{for L} \leq L_{min} \end{cases} \tag{3.20}$$

L is the Leaf area index (LAI), and L_{min} and L_{max} are minimum and maximum values, and are specified for each PFT. c_{ij} is the intra-species competition term between species i and species j, as described by table 3.1.

$$c_{ij} = \frac{1}{1 + exp\{20(height_i - height_j)/(height_i + height_j)\}} \tag{3.21}$$

$height_i$ is the vegetation height of PFT i. C_ν is the carbon content of the plant functional type, defined by eqn. 3.22.

$$C_\nu = L + R + W \tag{3.22}$$

L, R and W are the different components of the vegetation carbon content, divided into (L)eaf carbon, (R)oot carbon and (S)tem carbon. The local litterfall rate, Λ_l, is given by:

	i=1	i=2	i=3	i=4	i=5
j=1		*	1	1	1
j=2	*		1	1	1
j=3	0	0		1	1
j=4	0	0	0		*
j=5	0	0	0	*	

Table 3.1 *Intra- species competition relationships. Numbers $i = 1, 5$ represents plant functional types: broadleaf tree, needleleaf tree, shrub, C3 type grass, and C4 type grass. Entry '*' is given by eqn. 3.21. A value of 0 implies that PFT i dominates PFT j. A value of 1 implies PFT j dominates PFT i.*

$$\Lambda_l = \gamma_l L + \gamma_r R + \gamma_w W \tag{3.23}$$

γ_l,γ_r, and γ_w are the turnover rates of the different carbon pools. If we approximate eqn. 3.23 by

$$\Lambda_l \sim \frac{\gamma_l + \gamma_r + \gamma_w}{3}(L + R + W) \tag{3.24}$$

Then comparing eqns. 3.24 and 3.22 we can see that we are in effect approximating Λ_l as $\Lambda_l \propto C_\nu$. This assumption is also made by Huntingford *et al.* (2000). The TRIFFID equations can now be simplified to the one species case, expressed in terms of ν and C_ν. This form of TRIFFID is given in eqns. 3.25 and 3.26.

$$\frac{dC}{dt} = (1 - \lambda)\Pi - \alpha C \tag{3.25}$$

$$\frac{d\nu}{dt} = \frac{\lambda' \Pi \nu}{C_\nu}(1 - \nu) - \gamma\nu \tag{3.26}$$

NPP is initially assumed to be a constant. The λ function is originally a function of balanced leaf area index (balanced leaf area index is the LAI value before phenological constraints are applied), but leaf area index is approximately proportional to C_ν (Huntingford *et al.* (2000)) and so we can approximate the original λ function by a function of vegetation carbon content, given in eqn. 3.27.

$$\lambda' = \begin{cases} 1 & \text{for } C > C_{max} \\ \frac{C - C_{min}}{C_{max} - C_{min}} & \text{for } C_{min} < C \leq C_{max} \\ 0 & \text{for } C \leq C_{min} \end{cases} \tag{3.27}$$

C_{min} and C_{max} are the carbon densities corresponding to the maximum and minimum LAI values. The values of constants in eqns. 3.25, 3.26, and 3.27 are given in table 3.2. The value of α is chosen such that the behaviour of the simplified form of TRIFFID matches as closely as possible that of the full complexity TRIFFID.

	BL	NL	C3	C4	SH
γ ($year^{-1}$)	0.004	0.004	0.100	0.100	0.030
C_{max} ($kgC\ m^{-2}$)	26.0	27.1	0.3	0.5	2.0
C_{min} ($kgC\ m^{-2}$)	4.3	4.7	0.1	0.1	0.2

Table 3.2 *Values of constants, for each PFT. α must be chosen so the behaviour of the simplified model matches that of the full complexity model. This method was used in Huntingford* et al. *(2000). The γ values presented here are reproduced from Cox (2001). C_{max}, and C_{min} values are equivalent to minimum and maximum leaf area index values presented in Cox (2001).*

3.5 Validation

In order to test the ability of the simplified model to successfully capture the behaviour of the TRIFFID model, the simplified model is forced with a dataset of NPP, from a control run of MOSES2. The vegetation fractional coverage predicted by the simplified model is then compared to the fractional coverages predicted in the full TRIFFID model. Figure 3.4 compares the simplified model predicted fractional coverage of C4 grass, for an Australian grid box. Grass was chosen because it exhibits high variability, and therefore provides the most stringent test of the simplified model. Other tests were performed for land surfaces dominated by other PFTs. The shrub and tree PFTs do not exhibit as great variability as the grass PFTs, and because the simplified model requires that a suitable choice of α be selected these other tests are not particularly demanding. Therefore reproducing the high variability of grass PFT structure is the best test of the simplified model.

Figure 3.4 shows that the simplified model is fully capable of reproducing the behaviour of the

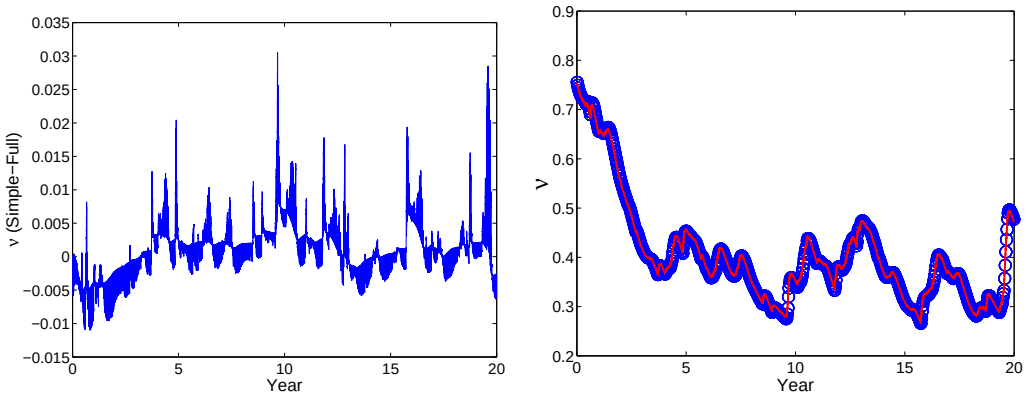

(a) (b)

Figure 3.4 *Comparison of fractional coverages from the full complexity TRIFFID DGVM, and from the simplified model, forced with identical net primary productivity. This is for an Australian grid box. a) shows the difference between simple model fractional coverage and the full complexity TRIFFID. b) shows the fractional coverage from the full complexity model and the simplified model. The full complexity TRIFFID fractional coverage is plotted with blue circles, and the simplified model predicted fractional coverage is plotted with a solid red line. For the simple model, a choice of* α *= 8.0*$\times$ 10^{-9} *year*$^{-1}$ *gave the best fit to the behaviour of the full complexity model. This value was derived through a method of trial and error.*

TRIFFID model. It suggests that results from analysis of the simplified model are directly applicable to the full TRIFFID model. We will therefore analyse the properties of this simplified model

3.6 Steady state solutions of the simplified model

Figure 3.5 simulates the re-growth from a small seeded amount ($1\times$ 10^{-4} % fractional coverage, and $1\times$ 10^{-6} kg C m^{-2} s^{-1}) of the broadleaf and needleleaf tree. As can be seen in fig. 3.5, the re-growth of the fractional coverage is much slower in coming to equilibrium than the carbon density. The difference in behaviour between the two tree PFTs is due to the different values of C_{max} and C_{min} (see table 3.2). The 's' shaped pattern of fractional coverage recovery is characteristic of the logistic equation (which has the general form : $\frac{dX}{dt} = X(1-X)$). The

logistic equation is characterised by an initially slow growth rate, when the population size (or fractional coverage) is small. Next the population undergoes rapid expansion, until the effects of over-crowding slow the population expansion rate down, and the curve reaches a steady state.

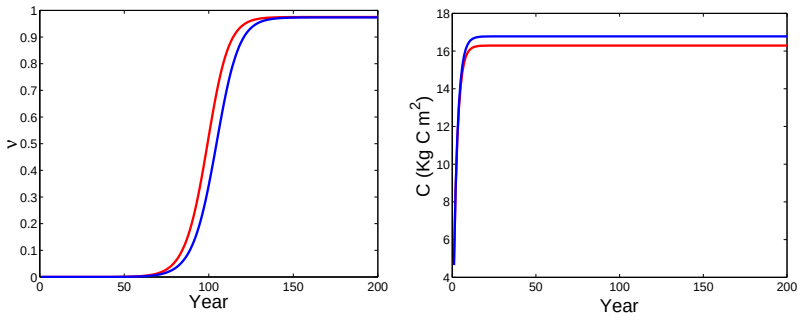

(a) (b)

Figure 3.5 *Simulation of broadleaf and needleleaf re-growth from bare soil using the simplified TRIFFID model. a) Fractional coverage. b) Carbon density. These figures show the re-growth from a small initial population of the two tree PFTs. Both PFTs have been individually simulated, and the two runs are over-laid for comparison. Broadleaf tree is shown as the red line, whilst needleleaf tree is shown as the blue line. In simulating the tree's re-growth the values for model constraints were taken form table 3.2,* α *was set to 0.128 year*$^{-1}$*. NPP = 1.57*$\times 10^{-7}$ *kg C m*$^{-2}$ *s*$^{-1}$*. Values of* α *and NPP were chosen so that the re-growth of trees took a realistic time (similar to that observed in later chapters). The merit of these plots is not in the prediction of the re-growth timescales, but in illustrating the intrinsic differences between the different tree PFTs, and the general pattern of re-growth common to all PFTs.*

The steady state solutions of the simplified model equations are found by setting the time derivatives to zero, and by solving the resulting equations. Doing this leads to eqns. 3.28 and 3.29.

$$\nu_{ss} = 1 - (\frac{\gamma}{\alpha})(\frac{1-\lambda'}{\lambda'}) \tag{3.28}$$

$$C_{ss} = \frac{(1-\lambda')\Pi}{\alpha} \tag{3.29}$$

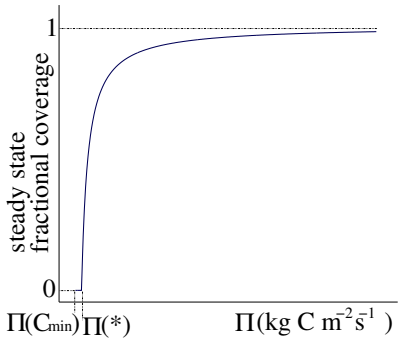

Figure 3.6 *The generic steady state response of vegetation fractional coverage to NPP (*Π*). The x-axis shows NPP. The y-axis shows steady state fractional coverage.*

When λ' takes the form of expression 3.27, the steady state solution is :

$$\nu_{ss} = 1 - \frac{\gamma}{\alpha}\left(\frac{(C_{max} - C_{min} + \frac{\Pi}{\alpha})}{(\frac{\Pi}{\alpha} - C_{min})} - 1\right) \tag{3.30}$$

$$C_{ss} = \frac{\Pi}{\alpha}\left(1 - \frac{(\frac{\Pi}{\alpha} - C_{min})}{(C_{max} - C_{min} + \frac{\Pi}{\alpha})}\right) \tag{3.31}$$

When the steady state fractional coverage is plotted as a function of net primary productivity, fig. 3.6, we see that below a cut off value of NPP, which will be referred to as $\Pi(*)$, the steady state fractional coverage is zero. For NPP $\leq \Pi(*)$ the growth rate is less than the harvesting rate and the population cannot expand. For NPP values greater than $\Pi(*)$ the fractional coverage increases non-linearly as a function of NPP. Initially the rate of change of ν_{ss} with respect to NPP is relatively large, and ν_{ss} is sensitive to small increases in NPP. For larger values of NPP the rate of change of ν_{ss} with respect to NPP is relatively small, and ν_{ss} is insensitive to increases in NPP. The absolute values of NPP vary for different PFTs, however, as NPP approaches some value, Π', such that ν_{ss} approaches 1, the vegetation structure becomes increasingly insensitive to further increases in NPP, because of the substantial over-crowding effects at this point on the curve. C_{ss} has a similar non-linear response, without the threshold level value of $\Pi(*)$.

3.7 Initial growth rates

The intrinsic growth rate (r_i) is the rate of population expansion in a completely unrestricting environment (i.e. without the effects of overcrowding). Lotka-Volterra type equations have one main timescale of variability (τ), which is the inverse of the intrinsic growth rate, $\tau = 1/r_i$. In the simplified TRIFFID model the intrinsic growth rate is given by:

$$r_i = \frac{\lambda' \Pi}{C} - \gamma \tag{3.32}$$

Equation 3.32 shows that the intrinsic growth rate is a linear function of net primary productivity. It also shows that the response time of the TRIFFID model is inversely proportional to carbon density. As NPP decreases towards $\Pi(*)$, τ increases towards infinity.

In the section 3.6 it was stated that below NPP$= \Pi(*)$ the steady state fractional coverage is zero. The interpretation of this is that at $\Pi(*)$ the growth rate (r_i) =0. Therefore from eqns. 3.31 and 3.32 it can been derived that:

$$\Pi(*) = \alpha[\frac{\alpha C_{min}(C_{max} - C_{min})}{1 - \gamma(C_{max} - C_{min})} + C_{min}][1 - \frac{\alpha C_{min}}{1 - \gamma(C_{max} - C_{min})}]^{-1} \tag{3.33}$$

In this chapter several different timescales are referred to. It important to define the relationships between these different timescales. The generic logistic curve has the form $\frac{d\nu}{dt} = r_i \nu(1 - \nu)$. r_i is the intrinsic growth rate. ν is the population size (in non-dimensional units). The maximum size of ν is assumed to be 1. When ν is small, $\frac{d\nu}{dt}\frac{1}{\nu} = r_i$. Therefore the intrinsic growth rate is equivalent to the initial growth rate. The logistic equation has solutions of the form:

$$\nu(t) = \frac{1}{1 + be^{-r_i t}} \tag{3.34}$$

This form of the logistic equation can then be used to relate the intrinsic growth rate to the re-growth timescale. The time taken to re-grow is assumed to be the time take to re-grow from ν_{init} to ν_{final}, *i.e.* the re-growth timescale is assumed to be the time taken to re-grow from a very small fractional coverage to some value close to the maximum possible fractional coverage. Figure 3.5(a) shows that as fractional coverage approaches the maximum possible value the re-growth slows down, and so it is necessary to consider re-growth to some percentage of the

maximum possible population as having re-grown. Constraining eqn. 3.34 to the initial condition $\nu(0)$=ν_{init} we have:

$$\nu(t) = \frac{1}{1+(\nu_{init}^{-1}-1)e^{-r_i t}} \tag{3.35}$$

and then the time taken to reach ν_{final} is given by:

$$re-growth\ time = \frac{1}{r_i} ln[(\nu_{final}^{-1}-1)(\nu_{init}^{-1}-1)^{-1}]^{-1} \tag{3.36}$$

This shows that the re-growth time, and indeed the time taken to change between any two values of ν is determined by the intrinsic growth rate and the two values of ν. Therefore the recovery from a 4% reduction in fractional coverage, the re-growth from near-bare soil conditions, and the initial re-growth rate are all governed by the same parameter, r.

3.8 Maximum rate of expansion and stability analysis

Equation 3.26 can be rearranged as :

$$\frac{d\nu}{dt} = (\frac{\lambda\Pi}{C}-\gamma)\nu - \frac{\lambda\Pi}{C}\nu^2 \tag{3.37}$$

A plot of $\frac{d\nu}{dt}$ against ν takes the form of a parabola, fig. 3.7. The zeros of $\frac{d\nu}{dt}$ are $\nu = 0$ and $\nu = 1 - \frac{\gamma C}{\lambda\Pi}$. The maximum value of $\frac{d\nu}{dt}$ is at $\nu = (1 - \frac{\gamma C}{\lambda\Pi})/2$, then the maximum rate of expansion is given by :

$$\frac{d\nu}{dt}|_{max} = \frac{\gamma^2 C}{2\Pi\lambda} \tag{3.38}$$

Figure 3.7 also demonstrates the stability of the model, for positive fractional coverages. At fractional coverages greater than $\nu = 1 - \frac{\gamma C}{\lambda\Pi}$ the change in fractional coverage is negative, and the fractional coverage decreases. For fractional coverages less than $\nu = 1 - \frac{\gamma C}{\lambda\Pi}$ the change in fractional coverage is positive, so perturbations away from the equilibrium point decay, and the model is stable.

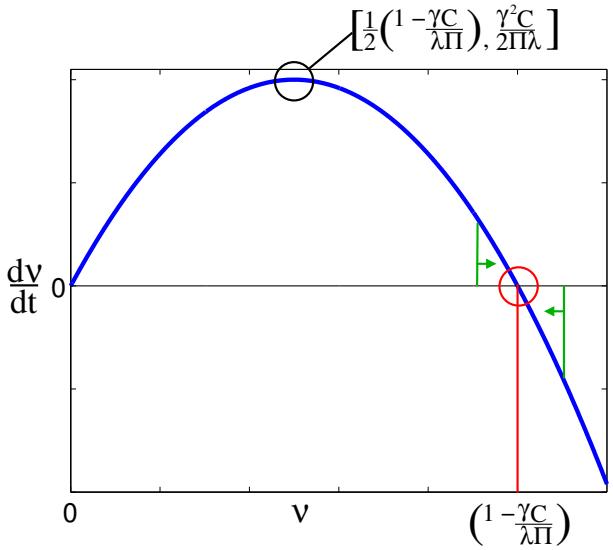

Figure 3.7 *Parabola properties of the simplified TRIFFID model. This figure shows the stability properties of the fractional coverage, ν. Marked on this figure is the maximum rate of expansion, and the maximum fractional coverage. The green lines and arrows indicate that if displaced from the equilibrium point marked with a red circle the system will return to the equilibrium point. This is therefore a stable equilibrium.*

In the discrete form of the logistic equation, equations can exhibit chaotic behaviour (May (1976)). However this is numerical chaotic behaviour of the discrete logistic equation, and it means that there is a limit to the size of possible timesteps. This effect is important when the timestep size is equal to 1 year, but is eliminated when a timestep of 10 days is used (tests were performed for grass plant functional types, as with the fastest response time they are most prone to chaotic effects). This emphasises the need to use relatively small timesteps.

3.9 Internal variability

The values of NPP in the full TRIFFID model are not constant, and are associated with the variability of meteorological surface conditions. The effect of forcing the simplified TRIFFID

model with stochastic net primary production is investigated in this section.

There is considerable intra-annual variability in grass structure in TRIFFID. The simple model is ideal for investigating the source of this variability. When the simplified model is run with a constant value of NPP, the fractional coverage does not vary between timesteps. A randomly generated data set of white noise NPP values are used to force the simple model. When this is done, as is seen in fig. 3.8, the vegetation structure also exhibits stochastic-like variability. The random NPP values mimic the natural variability of environmental conditions. When forced by stochastic NPP the model still exhibits convergence behaviour. This means that the model is still stable even when forced with random NPP datasets (which represents the variability of environment conditions in the full model). A system is generally considered stable if small differences in the initial conditions remain close together (Khalil (1996) p. 97).

In order to investigate the role of the intrinsic timescale in the observed variability of vegetation structure the spectral profile of the changes in fractional coverage was calculated, when the simplified model was forced with a white noise NPP data set. The simple model was run with broadleaf tree parameter values. Figure 3.9 shows the spectral profiles of both the NPP data and the corresponding fractional coverage changes. Figure 3.9 shows that when the simplified model is forced with white noise NPP it responds with red noise variability. This means that high frequency noise in the NPP data set is damped out. The frequency above which the variability is damped corresponds to the time taken to re-grow from near-bare soil conditions ($\sim$100 years). TRIFFID therefore acts as a climatic integrator below these timescales. This is also a general feature of individual trees (Woodward (1987)). The attenuation of timescales less than the characteristic response time was also shown by Lasaga and Berner (1998) to occur for the geological terrestrial carbon cycle. Henderson-Sellers (1993) state that this property of the global vegetation model is an important component of modelling global vegetation dynamically.

An additional feature discussed by Woodward (1987) is that trees tend to have an increased response to climate close to the characteristic timescale. This is equivalent to stating that the trees *resonate* at their characteristic timescale (for a mathematical definition of resonance see Thomson

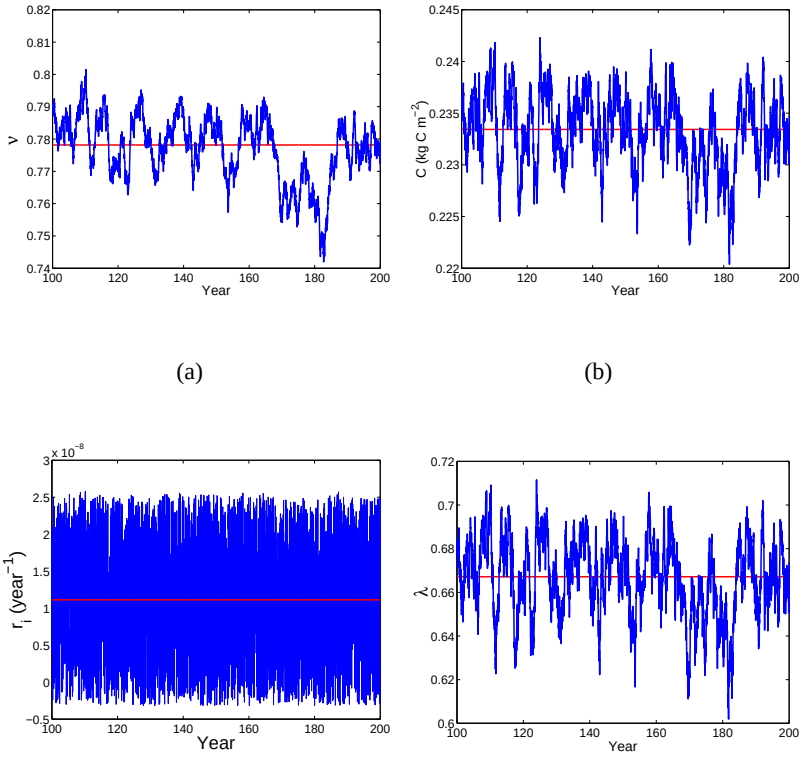

(a) (b)

(c) (d)

Figure 3.8 *The effect of forcing the simplified model with stochastic NPP, for C3 type grass. a) Fractional coverage. b) Carbon density. c) Intrinsic growth rate. d) λ function. The red line shows the grass behaviour for constant NPP. The blue line shows the behaviour of C3 type grass with a stochastic NPP term. α =7.13$\times 10^{-9}$ s^{-1}. $\overline{NPP}$=5$\times 10^{-9}$ $kg\ C\ m^2\ s^{-1}$. The amplitude of noise added to $\overline{NPP}$ =5$\times 10^{-9}$ $kg\ C\ m^2\ s^{-1}$. Values of α and $\overline{NPP}$ were chosen such that the re-growth from bare soil was realistically simulated. The amplitude of noise added was chosen to maximize the observed variability in vegetation structure.*

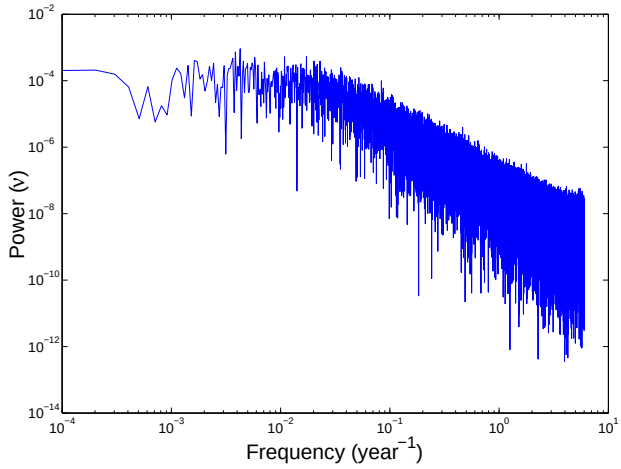

(a)

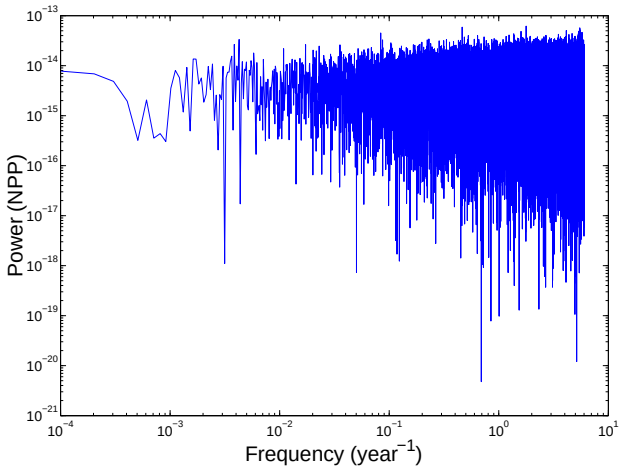

(b)

Figure 3.9 *a) the spectral profile of vegetation fractional coverage fluctuations. b) the spectral response of the NPP data set used to force the simplified model. In both figures the y-axis shows the power at a given frequency, whilst the x-axis shows the frequency. The model was run with monthly timesteps, and the data set length was 10,000 years.* $\overline{NPP}$*=1.57*$\times 10^{-7}$ $kg\ C\ m^2\ s^{-1}$. *The white noise amplitude is 1.25*$\times 10^{-7}$ $kg\ C\ m^2\ s^{-1}$. α*=0.128 year*$^{-1}$. *These values were chosen such that the re-growth from a small initial fractional coverage was realistically simulated. The amplitude of the white noise was chosen to maximize variability of fractional coverage.*

(1993)). The TRIFFID model does not explicitly include resonance (this can be seen in fig. 3.9), but may exhibit resonant behaviour when coupled to the ocean (through the atmosphere), as was the case in the conceptual model of Nevison *et al.* (1999). This would be hard to detect in the Hadley Centre model, and there is no evidence for vegetation-oceanic resonance at present. There is no clear resonant peak in the suite of models discussed by Mitchell and Karoly (2001), which includes the HadCM3 GCM.

3.10 Validation of re-growth times

Validation of the behaviour of the dynamical vegetation model is problematic, because of the length of observations required (Woodward and Beerling (1997)). One source of possible validation is the recovery of vegetation after the 1908 near-impact of an meteorite. On June the 30th, 1908, a large meteorite exploded 5-10km above Tunguska in western Siberia (60 N , 101 E). The blast is thought to have started forest fires, and photographic evidence shows that a large area ($\sim$ 2,000 km^2) of trees was uprooted (Vasilyev (1998)). At this latitude a HadSM3 grid box covers an area of approximately 55,000 km^2. The Tunguska perturbation therefore corresponds to a near-instantaneous reduction of fractional coverage of 4 %.

Given the site's obvious cosmological value the site has been repeatedly visited, however scientific literature on the Tunguska meteorite is usually cosmological, and often in Russian language (see Jones (2002), Svetsov (2002)). Detailed information on the fractional coverage of the disturbance is unavailable (T.P. Jones *pers. com.* 2003). Photographic evidence suggests, however, that the disturbance region had been re-colonised by 1990, which is taken here to show a timescale for the recovery of 80 years.

HadSM3 predicts dense needleleaf forest at the Tunguska grid box, which matches the observed swampy forest at the Tunguska site. The Tunguska grid box is then represented in the simple model as entirely needleleaf tree, and the Tunguska meteorite event as an instantaneous reduction if needleaf fractional coverage by 4 %. Figure 3.10 shows the predicted response of the grid box

fractional coverage of needleleaf trees to this perturbation.

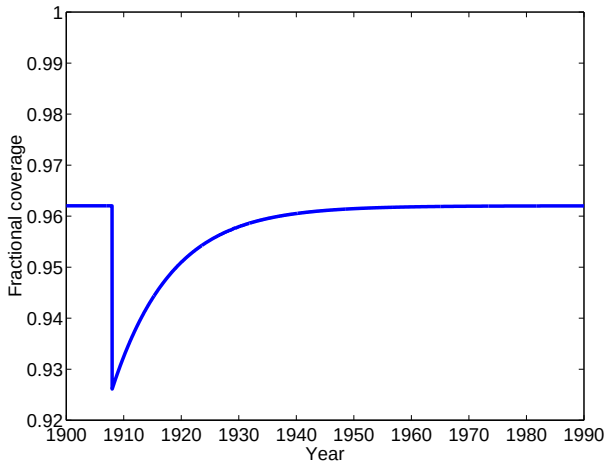

Figure 3.10 *Simulated re-growth of needleleaf tree PFT from the effect of the Tunguska meteorite in 1908. Values of NPP = 1.1*$\times 10^{-7}$ *kg C m*$^{-2}$ *s*$^{-1}$, α *= 4.12*$\times 10^{-9}$ *s*$^{-1}$ *were used. These values were chosen as they produced a re-growth from bare soil time of 125 years for needleleaf tree.*

Figure 3.10 shows that the simplified model predicts a full re-growth of needleleaf tree coverage by the mid 1990's, and is in agreement with what is know of the Tunguska site. Figure 3.10 also illustrates an important feature of the simplified model (and hence the full model). If instead of modelling the entire grid box the simplified model had been used to simulate vegetation re-growth only in the region of disturbed trees, the re-growth would have followed the same pattern as is shown in fig. 3.5, and the re-growth would have taken much longer (125 years).

3.11 Conclusions

The aim of this chapter was to investigate the properties of the population model relevant to properties of the vegetation-climate system in the TRIFFID model, and in order to perform this a simplified version of TRIFFID was developed and analysed.

The approximations made in developing the simplified form of the TRIFFID equations appear to have minimal effect. The assumption of a single plant functional type has been shown to be reasonable for the majority of global vegetation, but obviously constrains the model to simulating the dominant plant functional type. The assumption of constant litterfall and disturbance rates means that appropriate constants must be chosen to match the vegetation dynamics of the full model, but once this is done the simplified model captures the variability of the model. The main limitation is that the photosynthesis model was not coded explicitly into the model. The photosynthesis model, however, simply acts to translate climatic conditions into net primary productivity, and has been discussed elsewhere (see chapter 2). The net primary productivity has therefore been either specified, or set to a constant value with stochastic variability. Huntingford *et al.* (2000) present a simplified terrestrial carbon cycle which does simulate photosynthesis rates, and including this feature into the simplified model would only increase the model complexity without adding anything new.

Analysis of the TRIFFID equations suggests that the TRIFFID model parameters allow for stable coexistence. The fact that competing vegetation types are seen to be approximately mutually exclusive suggests that the plant functional types exist in a largely exclusive climatological niche. Analysis of TRIFFID equations predicts that the transition between plant functional types is smooth, rather than discrete (see Svirezhev (2000)). From the simplified TRIFFID model it can be seen that the fractional coverage is the slowest component of the TRIFFID system. Figure 3.5 shows that for tree PFTs, the carbon density has reached a steady state after 10 years, whilst fractional coverage takes 125 years to reach a steady state.

Data sets of net primary production and the vegetation structure were calculated in the full complexity surface energy scheme. Grid boxes where the dominant vegetation type was C4 type grass were chosen. Grass shows the largest variability in structure, and is therefore the most stringent test for the simplified model. The generated datasets of NPP were used to drive the simplified model, and the predicted vegetation structure was compared to that simulated by the full complexity model. Given the reduction in sophistication associated with assuming a single plant functional type, and constant litterfall parameters, the simplified model captures the

behaviour of the full complexity model surprisingly well.

Equations governing the steady state of the vegetation structure have been derived. They show the existence of a threshold value of NPP, below which vegetation coverage is zero. These equations also show that the steady state vegetation structure is insensitive to further increases in NPP as NPP becomes large. This insensitivity is due to the assumption that vegetation fractional coverage can be modelled using a logistic curve (see fig. 3.5(a)).

The initial growth rate and the maximum growth rate have been diagnosed. Both rates are dependent on the NPP. The initial growth rate is equivalent to the intrinsic growth rate, and is the reciprocal of the vegetation structure response time. The fractional coverage response time is the most important timescale (and hence the general response time) as it is the slowest response time of the TRIFFID model. This response time acts as a climate integrator, smoothing the effects of climate on the fractional coverage, and filtering out climate variability at frequencies above the response time. The response time also acts to provide a vegetation memory, perturbations to the vegetation structure decay at the response time of the vegetation. Further work is required to investigate how this affects the atmospheric variability. The results described here suggest that vegetation structure will change a white noise spectrum to red noise.

The population model exhibits convergence, even when forced with stochastic NPP, which means that the model is stable. It can therefore be concluded that the model is not a source of chaos. The simulated variability in grass structure (*e.g.* fig. 3.4) is therefore driven by variability in the meteorological conditions (potentially with feedbacks from the vegetation), rather than internal model variability. However the response time which is an internal feature of TRIFFID determines how much the stochastic meteorological signal is damped, and hence provides some internal control over the observed variability.

The timescales of response have been tested against observations of a well dated perturbation, on the spatial scale of an atmospheric grid box. The timescale of response predicted by the model

is similar to that observed. The discussion of the response to a small perturbation shows that the behaviour of the dynamic vegetation is scale dependent.

In the next chapters a GCM experiment using the HadSM3 model is presented where vegetation is allowed to re-grow from global desert conditions. Vegetation interactions with the atmosphere are included. This experiment is designed to perturb the global vegetation far from a steady state, in order to investigate the dynamical properties of the vegetation model. The results presented in this chapter will be used to interpret the results from the GCM experiment described in the next chapters.

CHAPTER 4

Transient GCM experiment

4.1 Introduction

In the previous chapter the dynamical properties of the vegetation model were investigated in isolation from the atmospheric model. A logical extension to this work is to investigate the dynamical properties of the vegetation interacting with the atmosphere. One way to do this is to investigate how vegetation behaves when it is far from a steady state with the atmosphere. In order to perturb the terrestrial carbon cycle far from the pre-agricultural steady state, vegetation coverage is set instantaneously to global desert conditions and vegetation is allowed to re-grow. There is an established precedent for using global bare soil conditions in order to assess the maximum effect of vegetation (see Betts (1999), Kleidon *et al.* (2000), Renssen *et al.* (2003b), Sitch *et al.* (2003)). The effect of a large perturbation will also be more easy to detect in the modelled climate system.

The type of behaviour to be expected from the dynamic vegetation model was described by Woodward and Beerling (1997). These include the ability to model recovery from disturbances and simulation of successional cycles, where vegetation types are replaced by other vegetation types (by definition). From the previous chapter it should be understood that both of these behaviours in TRIFFID are dominated by the same timescales, and are linked to the re-growth of vegetation from bare soil conditions.

Little has been said about the response of climate in mediating these behaviours. For the first time, this experiment uses a coupled climate-vegetation model to investigate the role of climate feedbacks in large-scale vegetation dynamics. This experiment therefore provides information about the response of terrestrial vegetation to disturbances, and the successional cycle, allowing for atmosphere-vegetation interactions. The importance of these feedbacks is reflected in the fact

that chapter 5 is dedicated to investigating and interpreting them.

4.2 Experimental setup

The HadSM3 GCM is used for this experiment (HadSM3 is described in detail in chapter 2). HadSM3 includes the MOSES2 surface exchange scheme, with the dynamic vegetation component, TRIFFID. The thermodynamic slab ocean model uses horizontal heat convergences consistent with modern sea surface temperatures. Atmospheric resolution is 3.75^o longitude by 2.5^o latitude. The atmosphere is in a pre-agricultural steady state at the start of the experiment. Atmospheric CO_2 is held constant throughout the experiment, at 287 ppmv.

At the start of the experiment the global distribution of vegetation is set to global desert. The term global desert is used here to denote specifying vegetation fractional coverages set to zero. The soil carbon pool is not cleared, and starts the experiment with pre-agricultural distributions of soil carbon. In the model soil carbon does not affect vegetation structure or soil physics, and since atmospheric CO_2 is not simulated interactively soil carbon concentration only affects itself.

The climate state associated with global desert conditions was discussed in chapter 2. When the land surface is held at global desert conditions the air temperature 1.5 m above the land surface is around 8^oC warmer over tropical continents, and approximately 6^oC cooler over boreal continents. There is almost universally less precipitation over land with global bare soil conditions. There is an especially strong decrease in precipitation over the Amazon basin associated with the global bare soil conditions (2 mm day^{-1}).

HadSM3 is then integrated, simulating 300 years of the response of the climate system to this perturbation. During these 300 years atmospheric CO_2 is held constant, so that only biophysical climate feedbacks are considered.

4.3 Pre-agricultural Vegetation Distributions

Vegetation fractional coverages consistent with the pre-agricultural atmosphere (the initial atmospheric conditions) are shown in fig. 4.1 (these conditions are similar to the CTL equilibrium experiment described in chapter 2). HadSM3 simulates both the tropical broadleaf forests, and the boreal needleleaf forests. There is substantial C4 type grass coverage over Australia and on the Sahara-Sahel boundary. C3 type grass mainly exists in boreal regions. Shrub coverage is predicted in various regions globally. The regions where some shrub is not present correspond to arid regions, or regions dominated by trees. Comparing these distributions with those predicted by Betts *et al.* (2003) with an fully dynamic ocean model (reproduced in chapter 2) we see a general agreement between the two sets of distributions. The simulation by Betts *et al.* (2003) predicts more broadleaf tree in the tropics than the pre-agricultural simulation presented here. The dominance hierarchy in TRIFFID means that the under-prediction of tropical broadleaf tree allows shrubs to cover larger regions in the experiment presented here, relative to the simulation discussed in Betts *et al.* (2003). In the simulation by Betts *et al.* (2003) there was predicted a region of grassland in North-East Amazonia which does not agree with observations (Betts *et al.* (2003)). This region of grassland is not predicted in the control simulation presented here. In the simulation presented here broadleaf tree exists in larger proportions in boreal regions than the simulation by Betts *et al.* (2003). Pre-agricultural land surfaces do not include the effect of agriculture in changing vegetation distributions to crop (typically assumed to be C4 type vegetation).

Figure 4.2 shows where in climate space each PFT is predicted large fractional coverage. The term climate space will be used to refer to the 1.5m air temperature and precipitation at a grid box. Figure 4.2 shows that each PFT exists in a relatively unique region of climate space. The steady state analysis of the simplified model, presented in chapter 3 implies that high fractional coverage is caused by relatively high NPP, and also corresponds to relatively high vegetation carbon densities. Broadleaf tree PFT is most abundant in warm and wet conditions. Needleleaf tree PFT is most abundant between -5 and 0 ^{o}C. C4 grass is most suited for warm, dry climates. C3 type grass PFT is found over a large amount of the climate space, however it is most abundant at very cold and dry conditions. Shrub PFT is most abundant between 0 and 10 ^{o}C. Shrub PFT is

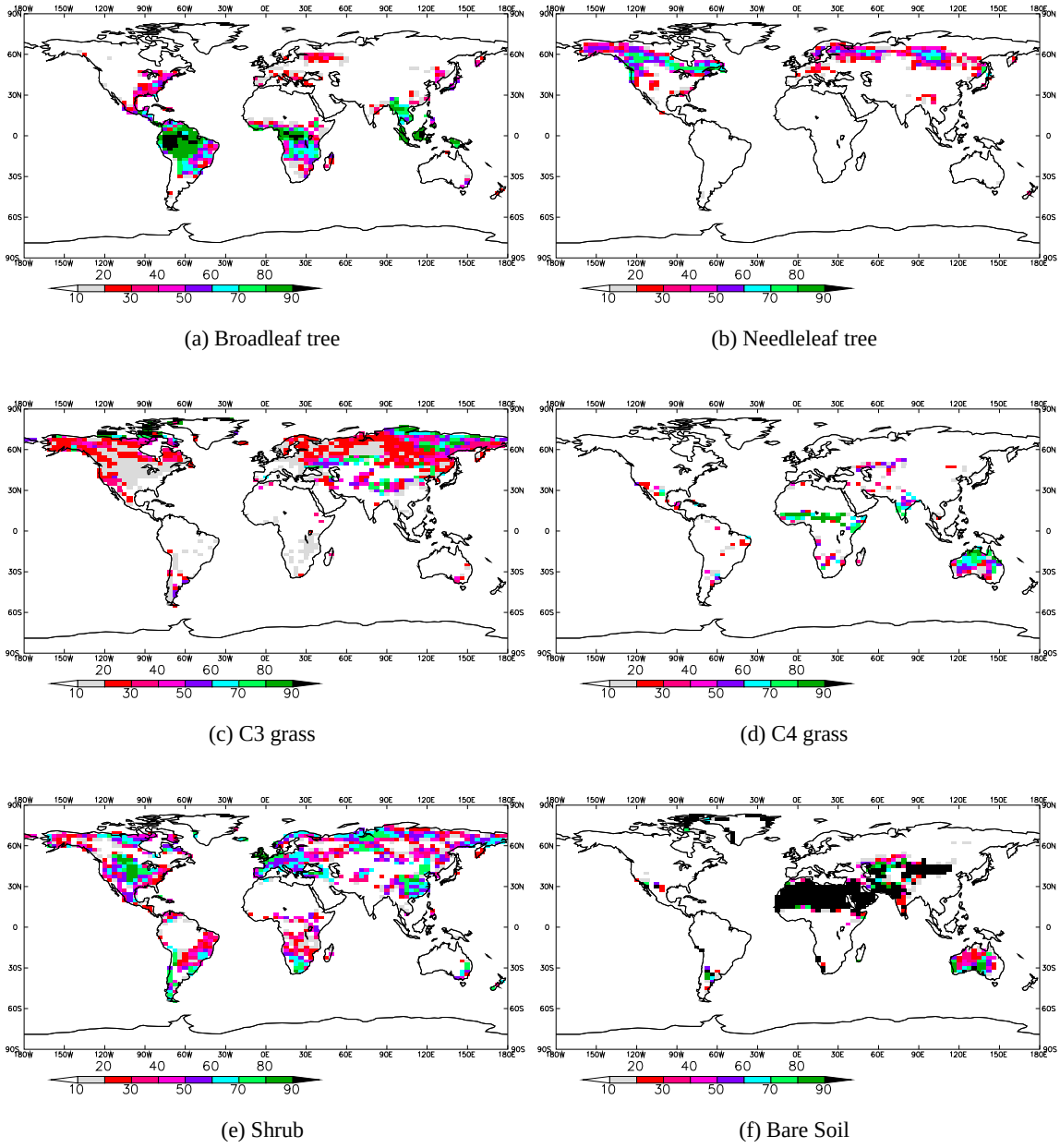

(a) Broadleaf tree

(b) Needleleaf tree

(c) C3 grass

(d) C4 grass

(e) Shrub

(f) Bare Soil

Figure 4.1 *The annual mean predicted PFT distributions of fractional coverage for the pre-industrial steady state, simulated using HadSM3.*

also less clustered in climate space than the tree PFTs or C4 type grass PFT. These environmental niches can also be identified in fig. 4.1. The environmental niches of shrub, C3 grass and C4 grass PFTs are in part determined by the environmental niches of the tree PFTs.

Figure 4.2 shows the climate tolerances of the PFTs but it is important to note that an additional parameter is CO_2. Under climate change it might be expected that a shift in environmental niches is driven by the varying level of CO_2. From the photosynthesis equations described in chapter 2 it is clear that changing CO_2 levels changes the PFT response to the hydrological cycle, but quantifying this effect requires further experimentation.

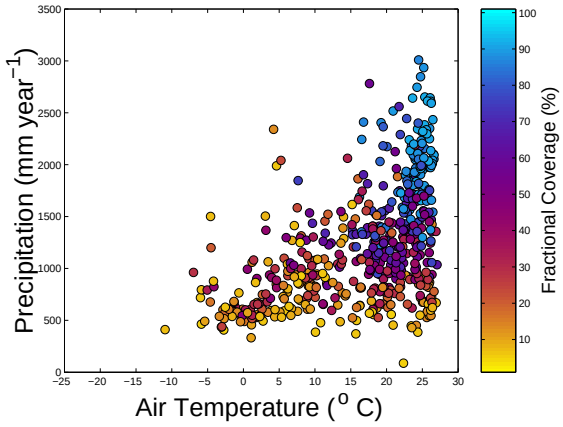

(a) Broadleaf tree

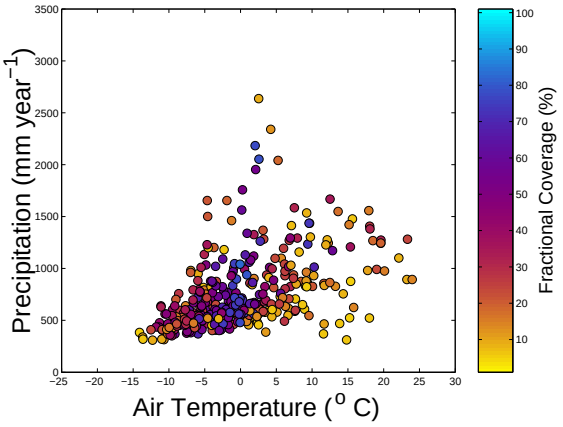

(b) Needleleaf tree

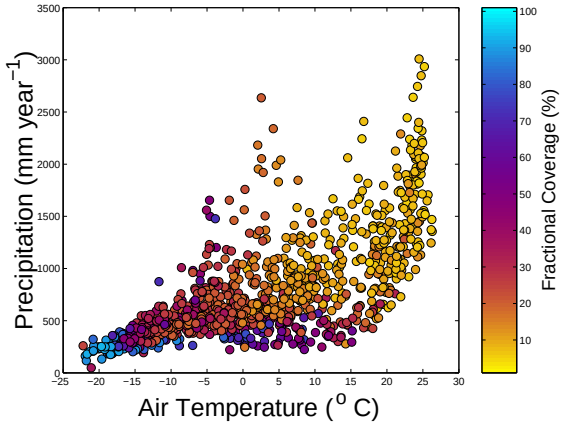

(c) C3 grass

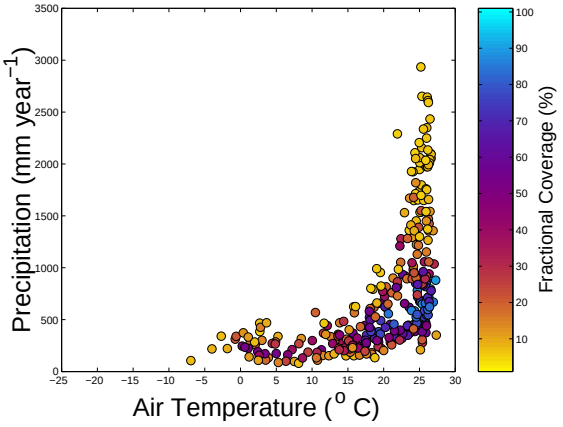

(d) C4 grass

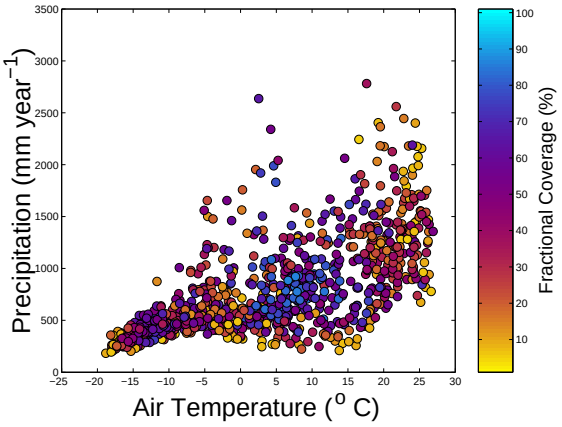

(e) Shrub

Figure 4.2 *Vegetation distributions within climate space (in terms of annual mean air temperature and precipitation). Each point represents the annual mean temperature and precipitation values where the functional coverage of the PFT is $> 5\%$. The colouring shows the fractional coverage. The maximum fractional coverages of the different PFTs are a): 92%, b): 82%, c): 92%, d): 89%, and e): 86%.*

4.4 Global Vegetation behaviour

Figure 4.3 shows the global mean vegetation fractions during the 300 years. Figure 4.3 shows that different vegetation PFTs grow at different rates. Within the first 20 years C3 and C4 type grasses have re-grown, covering a combined 70 % of the land surface (C3 grass = 50 %, C4 grass = 20 %). The fractional coverage of grass PFT are reduced as shrub re-grows. After 100 years shrub coverage has reached 45 % global coverage, displacing some of the grass coverage. By the end of the 300 years broadleaf trees have re-grown substantially, displacing more than 10 % of the shrub coverage. Needleleaf trees do not increase to more than 2 % global coverage throughout the entire 300 years. Markers positioned on the right-hand axis of fig. 4.3 show the pre-agricultural vegetation fractions. From fig. 4.3 it can be seen that by the end of the 300 years broadleaf trees are close to the pre-agricultural fractional coverage. Needleleaf forest coverage is not close to its pre-agricultural fractional coverage. Figure 4.4 shows the vegetation fractions at the end of the simulation. The boreal trees are almost completely absent (both needleleaf and

broadleaf). In the tropics broadleaf tree has mostly re-grown to pre-agricultural distributions, though pre-agricultural tropical broadleaf tree coverage is still larger. These differences in tree PFT distributions results in larger coverage of boreal shrub PFT, and the presence of shrub PFT in the Amazon basin.

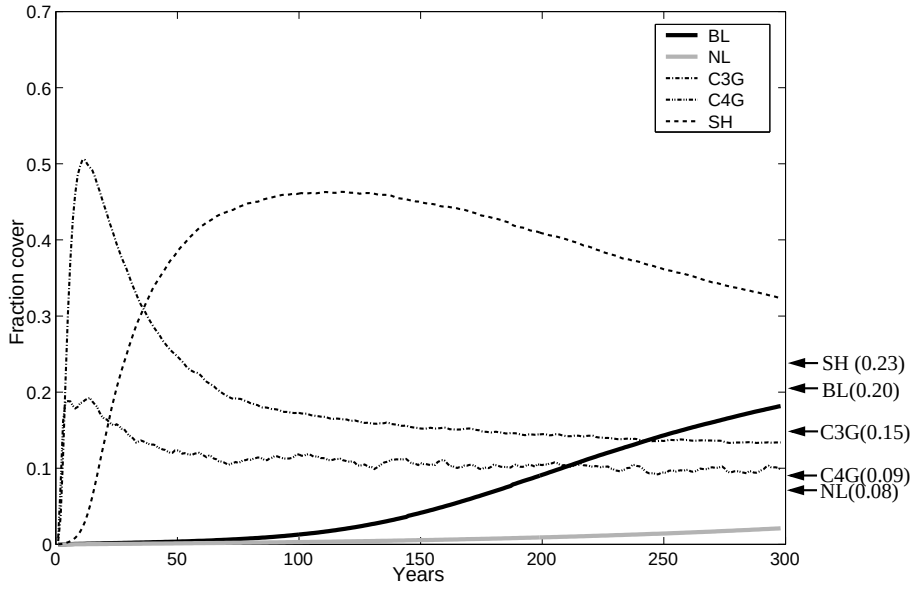

Figure 4.3 *Global mean vegetation fractions throughout the simulation. The mean does not include Antarctic or Greenland regions. BL=broadleaf tree, NL=Needleleaf tree, C3G=C3 grass, C4G=C4 grass, SH=Shrub. Bare soil is the residual fractional coverage. Markers on the right hand side of the axis indicate the pre-industrial control fractional coverages of the corresponding plant functional types.*

Vegetation distributions are not homogeneous, as is clear from figs. 4.1 and 4.4, and it will be useful to describe the vegetation behaviour regionally. The choice of how to divide the land surface was made to bound regions of similar vegetation behaviour, for pre-agricultural vegetation distributions.

Figure 4.3 shows that vegetation may take some time to come to equilibrium with climate. This long lag between climate and vegetation dynamics has implications for 'snap shot' climate

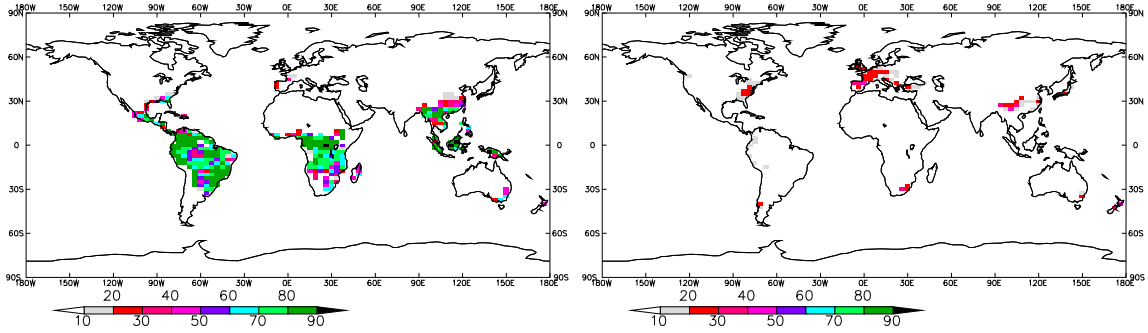

(a) Broadleaf tree

(b) Needleleaf tree

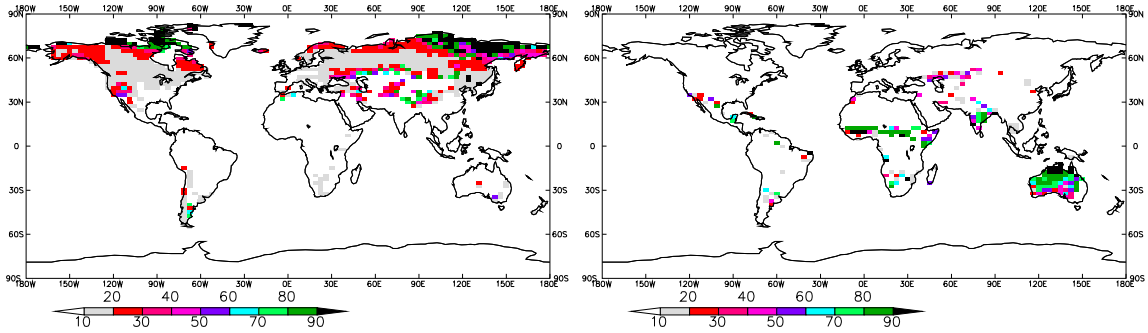

(c) C3 grass

(d) C4 grass

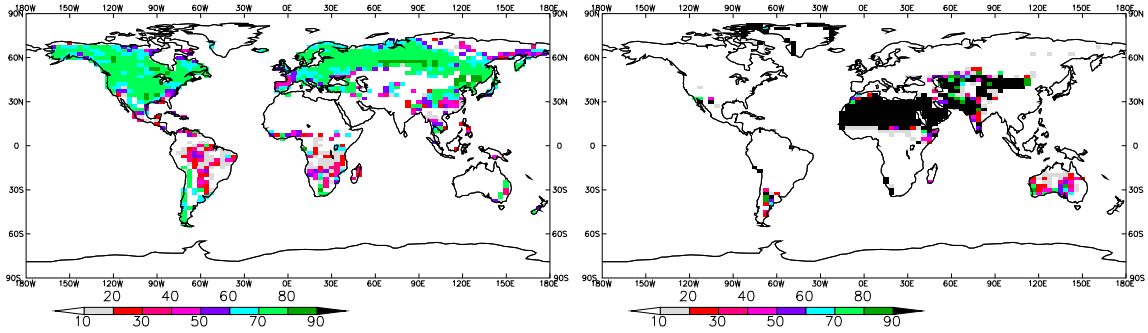

(e) Shrub

(f) Bare Soil

Figure 4.4 *Vegetation fractional coverages at the end of the 300 year GCM experiment. These fractional coverages are the average vegetation fractions for the final 10 years.*

simulations, which typically only simulate several decades, and assume that the vegetation is in equilibrium with the climate. It also highlights the long timescales imposed by vegetation. Frequently, century-scale natural climate variability is discussed in terms of the ocean only.

4.5 Regional Vegetation behaviour

By dividing the land surface into regions, several different land surface regimes can be investigated. The choice of regions is shown in fig. 4.5. These regions will be discussed in groups, linking similar behaviour.

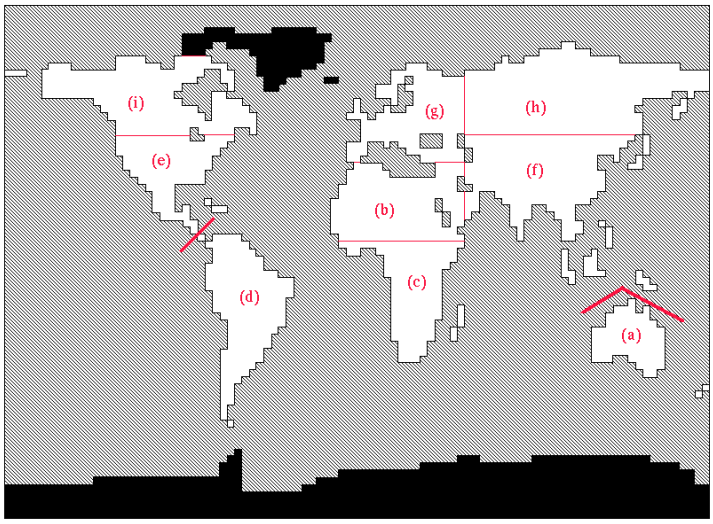

Figure 4.5 *The division of the land surface in regions. a) Australia. b) North Africa. c) South Africa. d) South America. e) Southern North America. f) South Asia. g) Europe. h) North Asia. i) Northern North America. References to regions will be taken to refer to the regions defined in this figure, rather than absolute geographical definitions.*

Australia and North Africa (regions 'a' and 'b' in fig. 4.5) are both desert-grass dominated. The

fractional coverages of vegetation over these two regions are summarised in figs. 4.6(a) and 4.6(b). In both regions C4 type grass quickly establishes itself as the dominant vegetation type. C4 grass is characterised by rapid fluctuations in vegetation structure, on the timescale of a year. The amplitude of variations in C4 type grass is similar to that seen by Sitch *et al.* (2003), who simulate variations of 30 % fractional coverage in similar environments (this amplitude is not shown in fig. 4.6(b), where the Sahara desert dominates the land surface coverage, however at the Sahara-Shael boundary this amplitude is observed). The rapid fluctuations in C4 grass implies rapid fluctuations in land surface properties (*e.g.* the roughness length and albedo). Alteration of land surface properties is a key process by which monsoon dynamics may be enhanced (Charney *et al.* (1975), Joussaume *et al.* (1999)), and Renssen *et al.* (2003a) show that the standard deviation of vegetation fluctuations in fractional coverage may be an important component of monsoon dynamics. We will discuss the role of climate in those fluctuations in the next chapter.

South Africa and South America (regions 'c' and 'd' in fig. 4.5) are both characterised by tropical forest, under pre-agricultural conditions (see fig. 4.1). Both regions show similar patterns of re-growth from the initial bare soil conditions. The fractional coverage of these regions throughout the 300 years are shown in figs. 4.6(c) and 4.6(d). Initially C3 and C4 type grass grow to dominance, in approximately equal magnitudes. After 30 years shrubs replace grasses as the dominant vegetation type. Shrubs reach their maximum fractional coverages after 75 years, when shrub covers 60 % of South Africa, and around 75 % of South America. After 75 years shrub fractional coverage declines, as the re-growth of broadleaf trees displace shrubs in both regions. In both regions the regional mean coverage of broadleaf trees is close to its pre-agricultural value by the end of the simulation. Broadleaf trees take the entire 300 years to reach these coverages.

Northern Hemisphere, sub-tropical and temperate vegetation is shown in Southern North America and South Asia regions (regions 'e' and 'f' in fig. 4.5). In both regions C3 type grass grows to dominance in the first few decades. Shrub displaces C3 grass after 30 years, and after 150 years the re-growth of broadleaf trees reduces the fractional coverage of shrub, although shrub remains the dominant plant function type. By the end of the 300 years, regional mean fractional coverages in South Asia are close to pre-agricultural state. In Southern North America regional

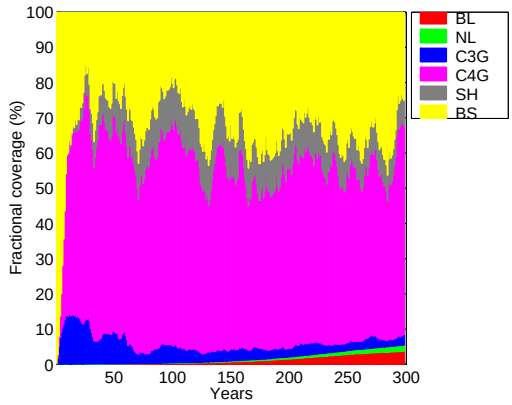

(a) Australian (4%,1%,3%,45%,9%)

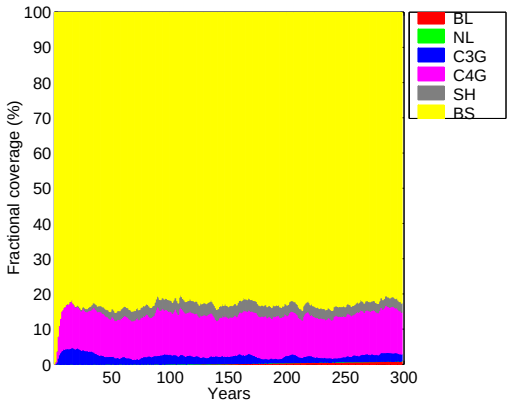

(b) North Africa (3%,0%,2%,13%,2%)

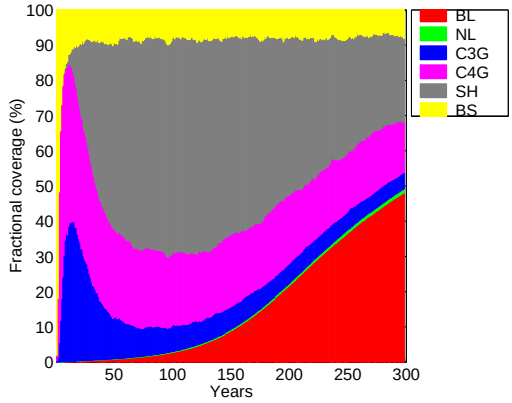

(c) South Africa (48%,0%,8%,14%,23%)

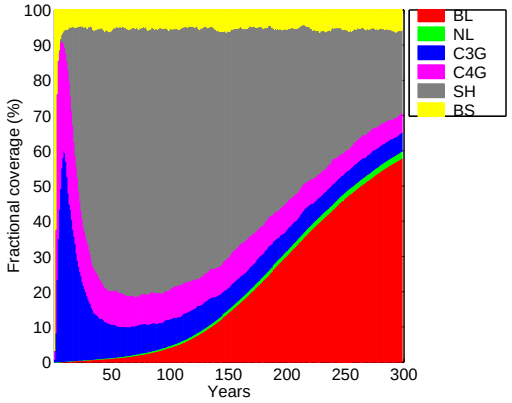

(d) South America (57%,0%,8%,6%,23%)

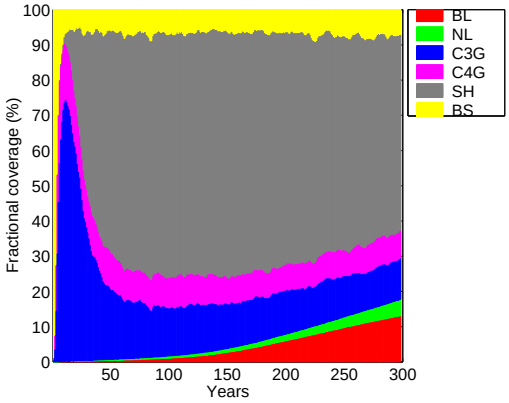

(e) S. North America (21%,10%,13%,8%,41%)

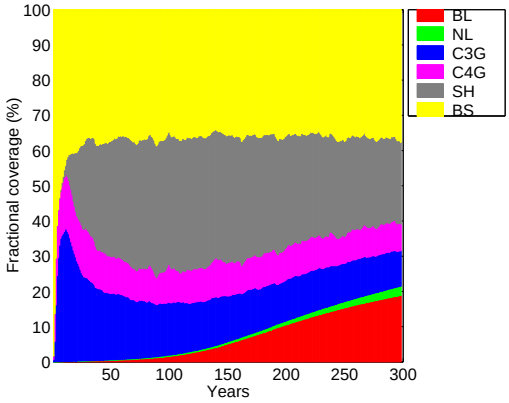

(f) South Asian (21%,2%,14%,7%,19%)

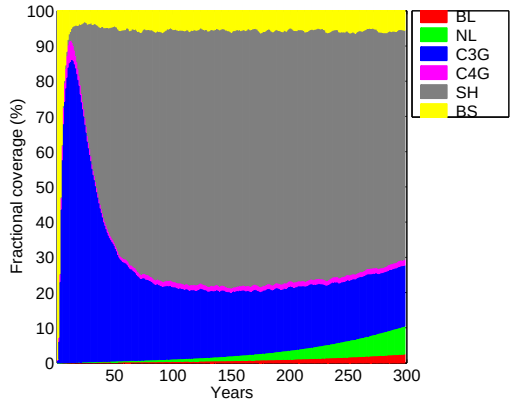

(g) Europe (11%,14%,22%,2%,46%)

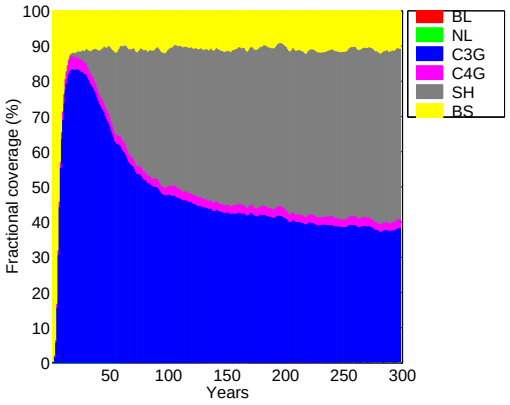

(h) North Asian (2%,16%,37%,3%,31%)

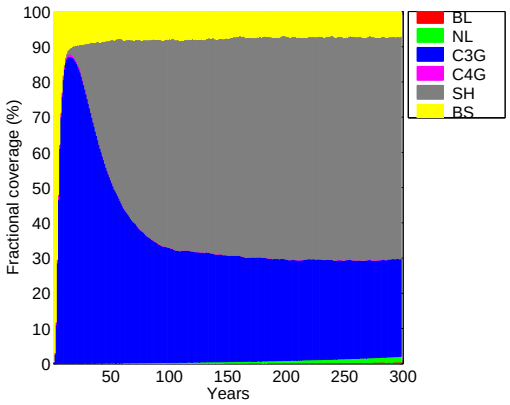

(i) N. North America (2%,35%,29%,0%,26%)

Figure 4.6 *Area averaged fractional coverage of each plant functional type. BL=broadleaf tree, NL=Needleleaf tree, C3G=C3 grass, C4G=C4 grass, SH=Shrub, BS= bare soil. The regions are defined in fig. 4.5. The pre-agricultural fractional coverages of different PFTs are given for each region in the sub-figure caption, in the order: BL, NL, C3, C4, SH.*

mean broadleaf forest cover is about 8 % less than the pre-agricultural state.

Europe, North Asia, and Northern North America cover land over approximately the same range of latitudes (regions 'g', 'h', and 'i' in fig. 4.5), and summarise the vegetation behaviour in the boreal regions. The behaviour of vegetation in these regions are shown in figs. 4.6(g), 4.6(h), and 4.6(i). In all regions C3 grass grows to over 80% coverage, within 30 years of the start of the simulation. Shrub replaces C3 grass at different times for the different regions, after 50 years in Europe, 60 years in Northern North America, and after 140 years in North Asia. It was shown in chapter 3 that the re-growth time is dependent on the levels of photosynthesis, and the differences in the time taken for shrub to reach dominance therefore reflects the differences in local climate.

The recovery of forest coverage in Northern Hemisphere boreal regions is slow, and forest coverage does not return to the pre-agricultural distributions by the end of the experiment. In Europe needleleaf forest has reached 9 % after 300 years, however the pre-agricultural coverage of needleleaf trees is 14 %, and broadleaf trees have not re-grown either. Northern Asia and Northern North America regions under pre-agricultural climate are covered by needleleaf trees (16 % and 35 % respectively) and neither show signs of the needleleaf forest re-growing after initialization from bare soil. Either the change in boreal climate associated with the experiment is such that the trees cannot re-grow in this experiment, (Bonan *et al.* (1992)), or the re-growth of boreal trees is very slow. This is in contrast to Brovkin *et al.* (2003), who found no alternative equilibrium. In chapter 3 it was shown that the TRIFFID model includes a threshold NPP value, below which fractional coverage does not remains at the minimum fractional coverage. However even above this NPP threshold value the practical check of a steady state is that the object of measurement does not change over a reasonable amount of time, and so the division between a secondary steady state or slow recovery is somewhat arbitrary, as the choice of a "reasonable amount" of time is subjective.

This discussion of the individual regions is sufficient to demonstrate the variety in land surface distributions. Regions dominated by grass undergo rapid alterations in land surface properties. This is consistent with the results presented in chapter 3, where it was shown that the internal

timescale of vegetation altered how much of the environmental variability is translated into variations in vegetation structure. From the figures considered here and in the previous section it is clear that grass has a much smaller timescale of response, and therefore undergoes much more variability in structure.

The regional analysis of vegetation distributions shows that boreal, needleleaf trees re-grow much slower than the broadleaf trees if they re-grow at all. This reflects the less favourable conditions for photosynthesis in which the needleleaf trees are growing (implying reduced photosynthesis rates). In the previous chapter (specifically fig. 3.5) it was shown that both types of trees have approximately the same rate of expansion, given the same photosynthesis rates. The regional analysis also crudely illustrates the division in climate space between broadleaf and needleleaf trees. In the hot tropical desert environments of Australia and North Africa C4 grass dominates over C3 type grass. What little amount of tree that can grow (in pre-agricultural climate) is broadleaf. Broadleaf tree also dominates the tropical forest regions. In these regions C3 and C4 grass exist in approximately equal proportions (at the regional or continental scale, not at the grid box scale). In sub-tropical regions both grass types exist, with C3 grass significantly more successful. Trees are still predominantly broadleaf. In the boreal regions only C3 grass exist in any significant amounts (*i.e.* there is little C4 grass). The majority of trees would be needleleaf under pre-agricultural climate, but it is impossible to test whether needleleaf tree will out-grow broadleaf tree at boreal latitudes as they did not re-grow by the end of the simulation.

4.6 Timescale quantification

In order to quantify the re-growth timescales associated with vegetation types it is assumed that the initial growth period can be reasonably modelled by solutions of the logistic eqn.:

$$\nu(t) = \frac{1}{1 + be^{-t/\tau}} \tag{4.1}$$

ν is the fractional coverage of plant functional type. b is a constant, and τ is the characteristic timescale of re-growth (in years) of ν, and is also assumed to be a constant (in eqn. 4.1) for each

dataset of fractional coverage re-growth, *i.e.* that the variable re-growth rate can be approximated by a single re-growth rate (the average rate). t is the time after the beginning of the simulation, also in years. Assuming that vegetation re-growth is logistic is justified because the dynamic vegetation equations, as described in chapter 3 also assume that the vegetation expansion follows the logistic curve, in the absence of competition.

The characteristic timescales of a PFT can only be directly estimated when the PFT grows from a small fractional coverage, and is the dominant PFT. It was shown in chapter 3, and in section 4.3 that PFTs on the same dominance level (*e.g.* C3 and C4 type grass) largely exist in different regions of climate space. Therefore this experiment is ideally suited for estimating the characteristic timescales of the vegetation PFTs.

The characteristic expansion rate is the rate at which PFTs expand when unrestricted. This rate, was shown in chapter 3 not to be a constant, but rather is dependent on the predicted rate of net carbon sequestration from the atmosphere. Environmental conditions may act to reduce the expansion rates via their effects on carbon sequestration, and the characteristic expansion rates calculated here include the effects of environmental conditions on vegetation expansion rates. The characteristic expansion rate is proportional to the time taken to re-grow from small fractional coverage. The precise relationship between these two timescales is defined in chapter 3.

A standard least squares method was used to estimate values of b and τ to fit eqn. 4.1 to the initial growth period of ν values from the full complexity model (see, for example Berthouex and Brown (1994)). Regions which supported more than 5% fractional coverage of the PFT after a reasonable recovery time were selected to estimate the τ value for that PFT. These grid boxes were selected on the 10th year for the grasses, after 50 years for shrub and at the end of the simulation for trees. Grass τ values were estimated from the first 3 years of re-growth, shrub timescales were estimated from the first 50 years and tree τ values from the whole 300 years. The short length of analysis for grasses means that estimates of the characteristic re-growth timescales for grasses are less reliable. By calculating the mean climate for time periods of 0-10 year, 0-50 years, and 0-300 years, the τ values can be plotted in climate space.

A period of 10 years for the grasses was chosen rather than 3 years in order to provide a more robust estimate of climate. The τ values are plotted in fig. 4.7, in terms of their local environment.

The τ values plotted in fig. 4.7 cluster in similar regions of climate space as the steady state fractional coverages do (fig. 4.2). This is because τ could only be estimated when the PFT re-grew, and as fig. 4.2 shows, each PFT inhabits a particular environmental niche. The number of points in fig. 4.7 is less than in figure 4.2, and the regions are therefore less well defined. The mean values of τ, and the standard deviation in τ, for all PFTs are given in table 4.1. Shrubs have a typical timescale of 8 year, grasses have a typical timescale of 0.5 years. Broadleaf trees have a mean characteristic timescale of 60 years, whilst needleleaf trees typically have a timescale of 70 years.

Figure 4.2 shows the steady state fractional coverage, which also implies relatively high or low rates of NPP. The τ values for broadleaf tree PFT, fig. 4.7(a), shows a clear relationship between implied NPP trends and the τ value, when compared to fig. 4.2(a). For the other PFT's the pattern is less clear but an overall trend of faster growth rate with higher NPP is apparent.

The different timescales associated with each PFT implies that the response timescale of a grid box will vary as a function of vegetation, and that the time spectra characteristics of a grid box will change as vegetation structure changes. Cyclic climate variability significantly lower than the characteristic period will not affect the vegetation structure. However the critical period is dependent on the properties, and hence on the climate itself. Above this critical period, vegetation structure will vary in response to the cyclic forcing, affecting the land surface properties, and possibly amplifying the climatic variability.

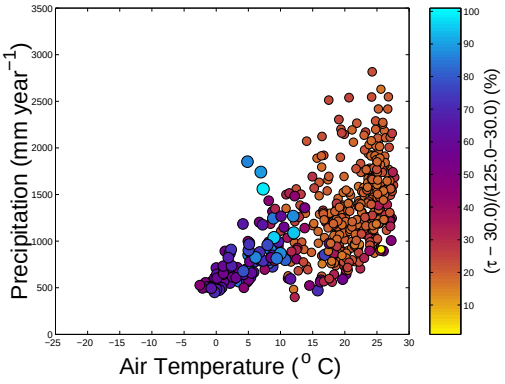

(a) Broadleaf tree

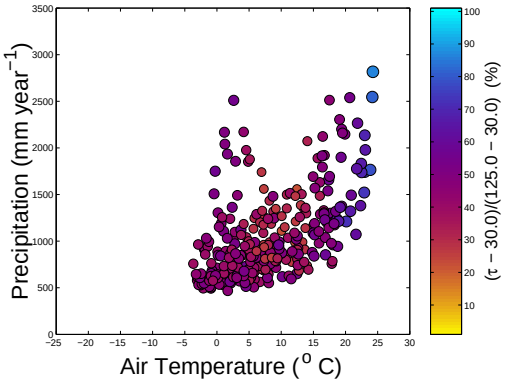

(b) Needleleaf tree

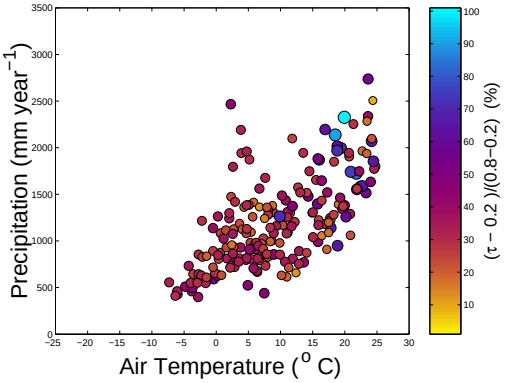

(c) C3 grass

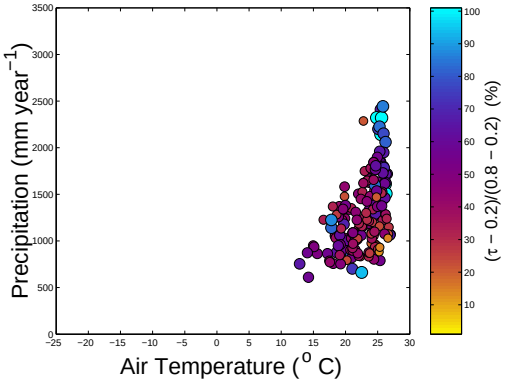

(d) C4 grass

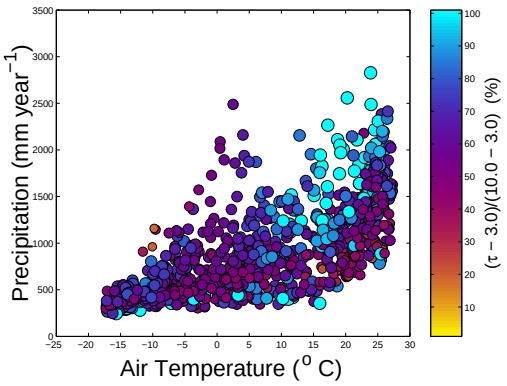

(e) Shrub

Figure 4.7 *τ values plotted in climate space. Tree τ values are scaled between 30 and 125 years. Shrub τ values are scaled between 3 and 10 years. Grass τ values are scaled between 0.4 and 0.8 years.*

PFT	No. grid points	No. years over which τ is calculated	Mean τ (year)	Standard Deviation in τ (year)
Shrub	1000	50	7.6	2.6
C3 grass	205	3	0.5	0.1
C4 grass	192	3	0.6	0.1
Broadleaf tree	444	300	59.6	19.0
Needleleaf tree	305	300	70.8	10.2

Table 4.1 *Mean τ for each PFT, as calculated from the data shown in fig. 4.7. the standard deviation of τ values are also given, along with details of the number of points used for each PFT.*

4.7 Carbon Cycle

Vegetation re-growth during the HadSM3-TRIFFID experiment is a useful example of the behaviour of the carbon cycle away from a steady state. As discussed in chapter 1, the vegetative state of the land surface is a central part of the terrestrial carbon cycle, and the transient behaviour

of the vegetation is an important component of the transient behaviour of the terrestrial carbon cycle. The strength of the coupling between vegetation and the terrestrial carbon cycle is emphasised in this section, where changes in the terrestrial carbon pool are related to changes in the vegetation state, and to the timescales of changes in the vegetation state. In particular the CO_2 source to sink properties of the terrestrial carbon cycle are discussed.

The magnitude of the terrestrial carbon pool is determined by the balance between net primary productivity (NPP) and soil microbe respiration. Net primary productivity is the balance between the gross canopy photosynthesis and the total plant respiration (*e.g.* Cox (2001)), and is the rate of carbon sequestration by vegetation per unit area. When NPP is greater than the emission of CO_2 from the soil the land surface is a sink of CO_2. When NPP is less than the emission of CO_2 from the soil, the land surface is a source of CO_2. If the vegetation re-growth timescales can influence the grid box NPP, they may also influence the timing of source to sink transitions. In the TRIFFID model soil emissions of CO_2 are calculated as a function of soil temperature, soil moisture, and soil carbon content, as was described in chapter 2. In the current version of the model the terrestrial carbon cycle is allowed to vary its carbon content, as if it were taking in carbon from the atmosphere, however the atmospheric CO_2 concentration is held constant.

4.7.1 Global terrestrial carbon pool

The rate of change of the global terrestrial carbon content is shown in fig. 4.8(a). Negative rates of change imply that the terrestrial carbon cycle is a potential source of CO_2. When the initial conditions are applied, soil carbon is at pre-agricultural distributions and the large negative rate of change of the terrestrial carbon pool is associated with soil respiration in the absence of photosynthesis. As grasses re-grow the land surface becomes a potential sink of CO_2. The displacement of grasses by shrubs after 30 years of simulation (fig. 4.3) corresponds to a sink to source transition in fig. 4.8(a). After 100 years tropical broadleaf trees have substantially re-grown and the land surface changes to a potential sink of CO_2.

In the following sub-sections the terrestrial carbon cycle of two very different environments is investigated during the simulation. In discussing these regions, the behaviour of the terrestrial carbon cycle will be linked to the behaviour of specific vegetation types.

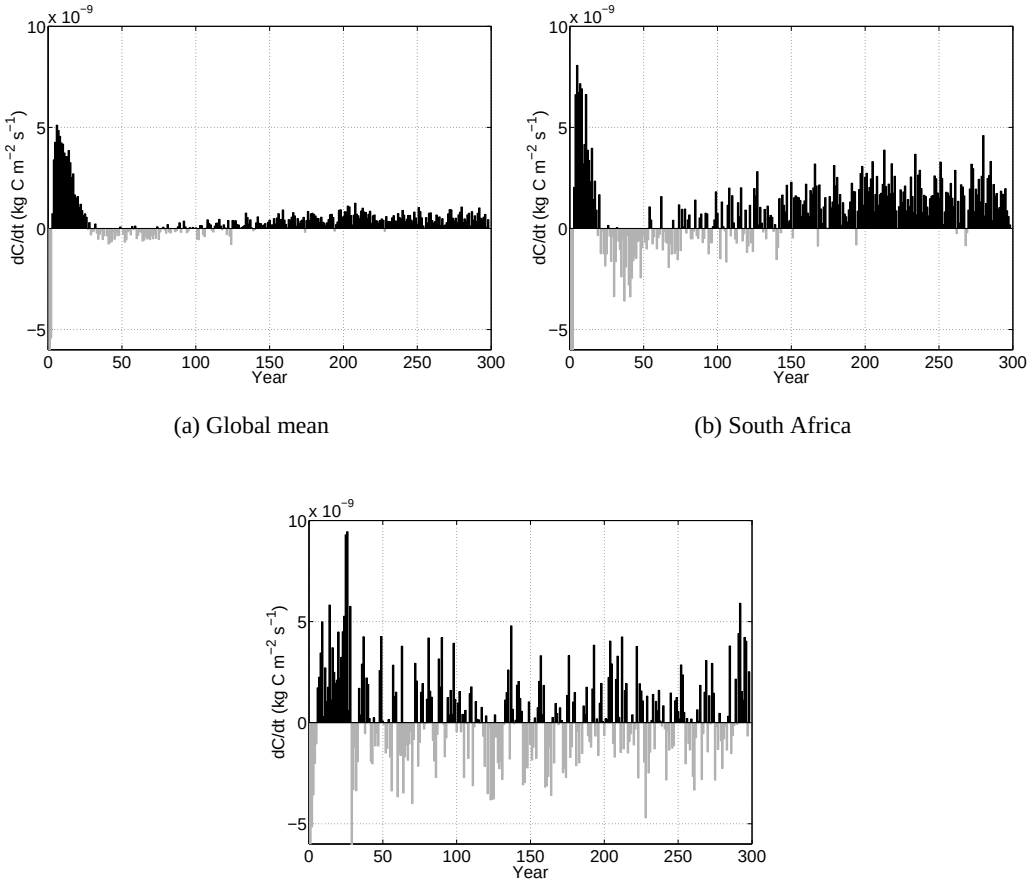

(a) Global mean

(b) South Africa

(c) Australia

Figure 4.8 *Rates of change of the terrestrial carbon content, during the 300 year re-growth from the global desert perturbation. Positive rates of change are plotted in black, whilst negative values are plotted in grey. All regions are plotted on the same axis range.*

4.7.2 Tropical Forest region

The rate of change of the terrestrial carbon pool, averaged over South Africa (region 'c' in fig. 4.5) is shown in fig. 4.8(b). Initially the rate of change of the terrestrial carbon pool is negative, resulting from the initial bare soil perturbation. As the grass grows, the South African region becomes a potential CO_2 sink. When grass is replaced by shrub coverage, fig. 4.6(c), the South African region becomes a potential source of CO_2. Broadleaf tree reaches significant fractional coverages after 100 years of simulation. Associated with the re-growth of broadleaf tree the South African region becomes a potential sink of CO_2.

The change from sink to source of CO_2 associated with the displacement of grasses by shrub appears to be driven by changes in the grid box NPP. When shrub displaces grass the NPP is reduced (as much as 50% on the continental scale). The reduced NPP is unable to balance the soil respiration of CO_2, and the terrestrial carbon cycle therefore loses CO_2 until a balance is found against the lower NPP level. This is seen in analysis of the soil carbon content. When grass is displaced by shrub the soil carbon content is reduced. This change must be driven either by a change in the soil properties (which isn't supported by analysis of the simulation) or a reduction in the amount of carbon passed via litterfall into the soil. The litterfall input of carbon to soil is dependent on NPP (eqn. 3.23 shows that litterfall is dependent on the carbon content of vegetation, eqn. 3.18 shows the dependency on NPP of the carbon content, and eqn. 3.29 shows that the steady state carbon content is dependent on NPP). A reduction in NPP therefore leads to a reduction in litterfall. The maximum rate of photosynthesis (V_m) is larger from grass PFTs than any other PFT, above 0^oC (see fig. 2.1). This means that the transition from a source to a sink of CO_2 is dependent on the assumed form of V_m. Assuming that the behaviour of the V_m function is qualitatively correct, the main sources of uncertainties of the source to sink transition result are the correct specification of environmental temperature tolerances (T_{upp} and T_{low} in eqn. 2.23) and the leaf nitrogen concentration.

Independent of whether the sink to source behaviour predicted is correct for the transition of grass to shrub coverage, the discussion of the sink to source transitions shows that when a PFT is

replaced by another PFT with a lower mean NPP the result will be a period where the terrestrial carbon cycle is a source of CO_2 until the terrestrial carbon balance comes into equilibrium with the new level of NPP.

4.7.3 Desert-Grass region

Figure 4.8(b) shows the rate of change of the terrestrial carbon pool during the HadSM3-TRIFFID experiment, averaged over Australia (this region is defined as region 'a' in fig. 4.5). The Australian carbon pool exhibits no apparent trend. This is consistent with the fact that the Australian region is dominated by C4 grass, fig. 4.6(a). Throughout the experiment the Australian region fluctuates rapidly between being a potential source and sink of CO_2, associated with the C4 grass fluctuations.

4.8 Conclusions

The HadSM3-TRIFFID experiment presented here shows that vegetation in the TRIFFID model changes its fractional coverage on long timescales. Long vegetation timescales mean that the terrestrial carbon cycle is slow to come to steady state, relative to the atmosphere. This has an important implication for the initial length of "spin up" integration required for those model integrations which include dynamic vegetation. This will particularly effect palaeoclimate simulations where there are larger uncertainties in reconstructed distributions of vegetation from palaeorecords, as with greater uncertainty in the vegetation distributions the climate system is further from a climate-vegetation equilibrium, and the time taken to reach equilibrium increases.

The characteristic timescales of different PFTs are also important for the timing of successional transitions between PFTs. During climate change a region of the land surface may become inhabitable, or uninhabitable for a particular PFT. The timescale of the dominant vegetation type to grow in a region is crucial for estimates of the state of the land surface, and the terrestrial

carbon cycle, and this is governed by the characteristic timescale. In another GCM experiment, using the same GCM, but with a dynamic ocean model and a fully coupled carbon cycle (Cox *et al.* (2001)) it was observed that a die-back of the Amazon rain forest and global increase in soil respiration changed the terrestrial carbon cycle from a net sink of CO_2 into a net source of CO_2. The recovery from this state in the model, if it occurred at all, would be dominated by the timescales investigated here.

The estimated timescales for each vegetation type are similar to the timescale of tree re-growth, and therefore appear reasonable, but rigourous evaluation of the model results against observations is difficult given the length of observations required (Woodward and Beerling (1997)). The TRIFFID model predicts an ecosystem type response, whilst ecological data is primarily individual based. An individual pine tree species, for example, may propagate horizontally through dispersion of seeds, however TRIFFID simulates the re-growth of forests, grass lands and other ecosystems, rather than individual vegetation species and may well operate on a different timescale (Delcourt *et al.* (1983)). TRIFFID does not represent the time needed for the horizontal dispersion of seeds, and assumes that there are sufficient seeds corresponding to a particular PFT (see chapter 6 for further discussion of this issue).

A continental scale perturbation to vegetation is unethical, impossible, and monitoring the re-growth might take centuries. Moreover given the importance of understanding the behaviour of the carbon cycle now, other methods must be sought to validate the behaviour of the land surface model. Observations of small scale deforestation and re-growth provide some data on the timescales involved in ecosystem recovery, but these studies do not account for large scale changes to the atmospheric circulation. Scaling results from small scale observations to global scale predictions may not be a reliable source of validation of the dynamics of global vegetation.

Another approach is to investigate the variability of existing vegetation. The spectral analysis presented in chapter 3 showed that TRIFFID attenuates atmospheric variability at frequencies above the characteristic timescale for re-growth. However testing the variability of global vegetation using this approach would require datasets at least 1,000 years in length (for the tree

PFTs). It may be possible in the future to use datasets of atmospheric CO_2 to infer the behaviour of the biosphere. However to do this would require very high resolution ($\Delta < 10$ years), and about 1,000 years in length. Such a dataset of CO_2 levels is not currently available. Even if such a dataset did exist the extent to which CO_2 variations were due to the ocean carbon cycle would require investigation.

If it were possible to validate the rapid PFTs against observations then predictions of the behaviour of the slow PFTs could be considered more reliable. An ideal location over which to investigate the behaviour of grass is Australia. Satellite observations are not available for the length of time required, however aerial photography may provide the data with which to validate the dynamics of the vegetation (see Fensham and Fairfax (2002), Kadmon and Harari-Kremer (1999)). However any comparison between photographic data and the PFTs predicted in TRIFFID would be a major project, and will not be investigated further here. From validation studies such as is included in Betts *et al.* (2003) it is seen that correct simulation of grass dynamics will require the simulation of grass-fire dynamics.

In chapter 3 it was shown that the re-growth rate of a PFT is dependent on the photosynthesis rate. This dependency is illustrated here, where the different estimates of τ correspond to different local climates, and large τ has been shown to be approximately inversely proportional to NPP. As was shown in chapter 3 the value of τ in the logistic equation determines the time taken to re-grow from any size perturbation, however when the atmosphere is included any perturbation to the land surface large enough to make significant changes to climate will alter the effective τ value.

The impact of the characteristic timescale (τ) values on the terrestrial carbon cycle has been investigated, and the characteristic PFT timescale has been shown to be important for the behaviour of the terrestrial carbon cycle. The effect of atmospheric conditions on the re-growth of vegetation will be investigated further in the next chapter.

CHAPTER 5

The atmosphere during regrowth

5.1 Introduction

In chapter 4 an experiment was discussed that illustrated large time lags in the vegetation structure. The large response time in terrestrial vegetation was also shown to be important for the terrestrial carbon cycle. However, the changes in climate were not discussed, or the potential interactions between climate and vegetation. We will investigate these aspects in this chapter.

Changes in the structure of vegetation result in changes in the surface conditions. Betts (1999) showed that the presence of vegetation in the HadCM2 model can alter the climate enough to be significantly self-beneficial, and affects the equilibrium vegetation structure. HadCM2 does not use the MOSES2 scheme, though Betts (1999) uses TRIFFID to predict equilibrium vegetation distributions. As was shown in chapter 3, the response time of vegetation can vary as a function of photosynthesis (and hence environmental conditions). It is therefore important to test this result in the full GCM model, and to quantify the importance of environmental conditions on the transient behaviour of the vegetation. In the previous chapter the characteristic response timescales of the PFTs were estimated from a long GCM experiment. Analysis of the timescales response to climate supported the results from the simplified model developed in chapter 3. However a more controlled investigation is required to test the dependency of PFT timescales on changes in the climate.

In section 5.2 the evolution of the global surface climate, in the GCM simulation is described. Section 5.3 continues this analysis, describing regional climatology throughout the GCM simulation using the same regions as in the previous chapter. In section 5.4 the effects of the the induced change in climate on the re-growth of vegetation is investigated. This requires the

decoupling of vegetation and the atmosphere, and uses an offline version of the surface exchange scheme. This offline model also allows a detailed investigation into the mechanism that alters the rate of re-growth in the Amazonian region. Finally, in section 5.5 the effect of atmospheric feedbacks on the behaviour of the terrestrial carbon cycle is discussed for global vegetation.

5.2 Global Climate summary

Figure 4.3 shows the behaviour of the global coverage of PFTs throughout the 300 year GCM experiment. Grass re-grows within the first 15 years. Shrubs re-grow to dominance after 50 years. Broadleaf tree PFT has nearly fully re-grown after 300 years. Needleleaf trees are substantially less than the pre-agricultural coverages at the end of the 300 year integration. In this section the climate during the simulation is investigated.

The global land surface climate during the experiment is shown in fig. 5.1, in terms of global mean air temperature at 1.5 m above the land surface and global mean precipitation over land. Initially global surface air temperature over land drops by more than 2.0^o C. Global precipitation is also reduced, by approximately 100 mm year^{-1}. The pre-agricultural global mean land surface albedo is 24.6 % (using eqn. 2.5). The global mean land surface albedo of the bare soil condition is 25.2 %. This difference in surface albedo predicts an increase in the amount of shortwave radiation reflected and probably causes the drop in temperature and the reduction in precipitation (by reducing global evaporation). After 10 years of the simulation C3 and C4 grass have re-grown in some areas, but shrub has not. The surface albedo at this time is 26.6 %, implying a further drop in land surface air temperature, which is seen in fig. 5.1(a). As shrubs re-grow the global mean surface albedo drops by 0.2 %, and this corresponds to a simulated increase in global temperature of 1.0 ^{o} C, although it is not clear from this description that the change is driven by surface albedo changes. As the tropical trees re-grow the global mean land surface albedo drops by 1.5 %. The effect of increasing the global roughness length is to increase surface fluxes of momentum, moisture and heat and will also be important in determining the changes in climate. The re-growth of broadleaf tree does not correspond to a further increase in temperature, but an

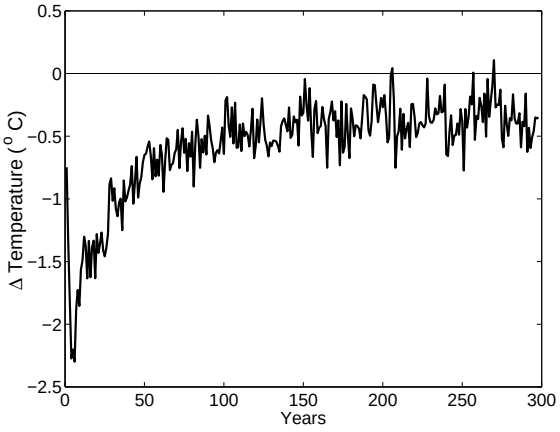

(a)

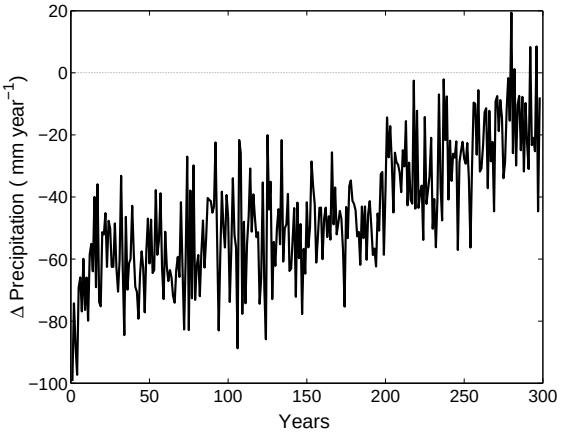

(b)

Figure 5.1 *Changes in the global annual mean land surface climate, in terms of a) 1.5 m air temperature and b) precipitation, throughout the 300 year GCM experiment, differenced against the pre-agricultural control steady state simulation. Pre-agriculture mean values are 6.5^o C, and 709 mm year^{-1}.*

increase in precipitation over land of about 50 mm year^{-1}. At the end of the simulation the land surface albedo is still 0.8 % higher than the pre-agricultural control simulation and the 1.5 m air temperature over land is 0.4 ^{o} C cooler than the pre-agricultural simulation. This difference in surface albedo is most likely due to the absence of the boreal forests.

Considering the global mean values of 1.5m air temperature and precipitation does not investigate which regions produce particular features of the observed trend in global surface temperature and precipitation. More detailed investigation is required to understand the mechanism driving the observed changes. Consideration of only the global mean state also hides the fact that vegetation in one region may significantly alter the climate that another region of vegetation is growing in. Therefore we will concentrate our analysis of the causes on specific regions. In choosing regions to average the climate, those previously used to summarise vegetation behaviour in chapter 4 have been used; this approach allows comparison with the observed changes in the land surface structure, and divides the land surface into regions of similar vegetation types.

5.3 Regional atmospheric change

5.3.1 Desert-Grass atmosphere

Figures 5.2(a), 5.2(b), 5.3(a), and 5.3(b) show the mean air temperature and precipitation rates over the Australia and North Africa land surfaces. Both North Africa and Australia are dominated by bare soil and C4 grass. The interannual variation in fractional coverage of C4 grass is large (around 30 % fractional coverage over Australia), leading to rapid changes in the land surface properties. The average surface albedo over the Australia region is 22.6% (discarding the first 20 years of the simulation). The standard deviation in the mean Australian surface albedo is 0.4 %. The mean Australian roughness length is 0.08 m, and the standard deviation in this value is 0.01 m. The 1.5 m air temperature over Australia is close to the pre-agricultural air temperature thoughout the simulation, though there is inter-annual variability with an amplitude of 0.5^o C. The North Africa region is cooler than the pre-agricultural control ($\sim 0.5^o$ C) thoughout the simulation, though by the end of the simulation this region has warmed. This change is on the same timescale as the re-growth of the tropical tree coverage. The fact that the North Africa region is affected by the re-growth of the tropical broadleaf tree PFT, whilst no broadleaf tree grows in the region illustrates the ability of vegetation to affect the non-local climate, and

highlights the importance of the vegetation response timescales.

The mean precipitation over these regions also shows considerable interannual variability (approximately 25 % in both regions). It is unclear what drives the variability in climate over these regions, *i.e.* what contribution the variability of land surface properties makes. The results presented in chapter 3 show that variability in the vegetation fractional coverage is driven by variability in the environmental conditions. However previous studies of the mechanisms of monsoon dynamics highlight the importance of vegetation in modifying the land surface properties (see chapter 1). This is one region that the dynamical properties of the land surface may strongly influence the dynamics of climate. The characteristic timescale of C4 grass was estimated to be 0.6 $\pm$ 0.1 years in the previous chapter. As this timescale is similar to the monsoon cycle, vegetation attenuation of the environmental variability may be important. Mechanisms altering the timescales of vegetation response will therefore affect the ability of vegetation to response to climatic variability and the feedback strength of vegetation.

5.3.2 Tropical Forest Atmosphere

During the re-growth experiment the climate over South America and South Africa follow similar patterns. The mean temperatures (annual means, averaged over the regions) are shown in figs. 5.2(c) and 5.2(d). During the first years both regions are warmer than the pre-agricultural control climate (approximately 1^o C warmer). As the grasses re-grow the mean temperatures fall below the pre-agricultural control climate (-0.5^o C in South Africa and -1.0^o C in South America). As the shrub PFT re-grows the average temperatures increase above the pre-agricultural control (approximately 0.5^o C). Finally as the tree PFTs re-grow the average temperatures are reduced. By the end of the simulation the average temperature is close to the pre-agricultural control climate. Precipitation during the simulation also follows a similar pattern in the two regions. Initially both regions experience between 150 and 300 mm year^{-1} less precipitation than the pre-agricultural control climate. There is not a clear impact of the grass and shrub re-growth. However there is a clear increase in precipitation in the last 150 years associated with the re-growth of tree PFTs.

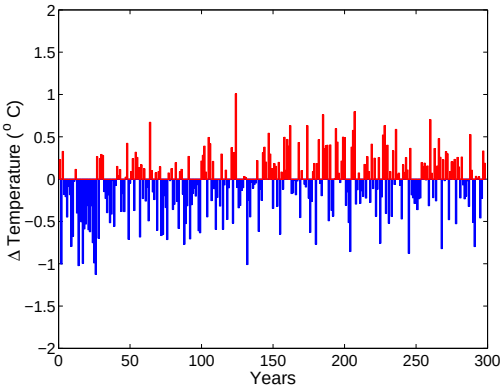

(a) Australian region (19.1^o C)

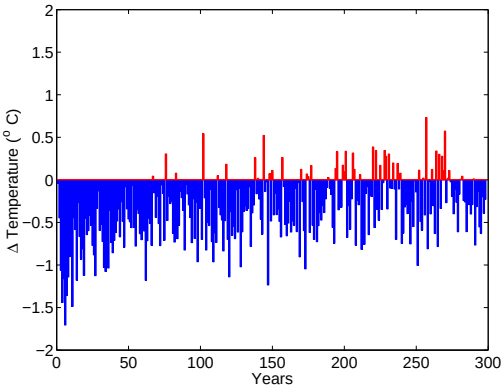

(b) North Africa region (21.8^o C)

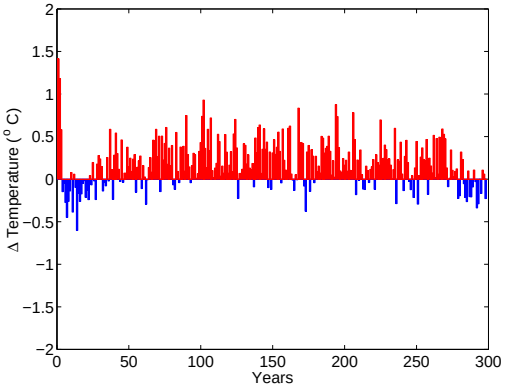

(c) South Africa region (21.2^o C)

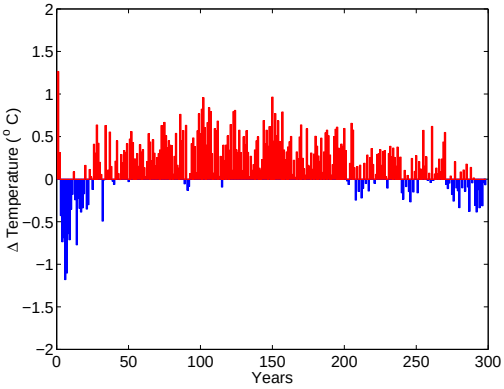

(d) South America region (20.7^o C)

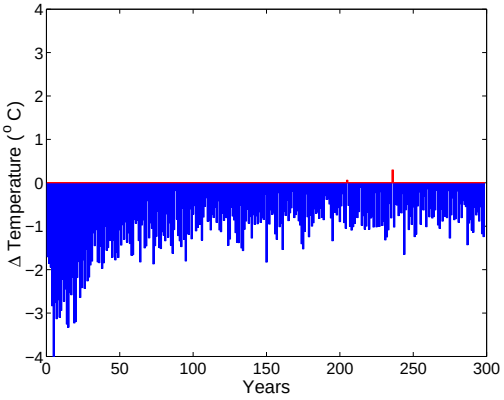

(e) Southern North America (13.4^o C)

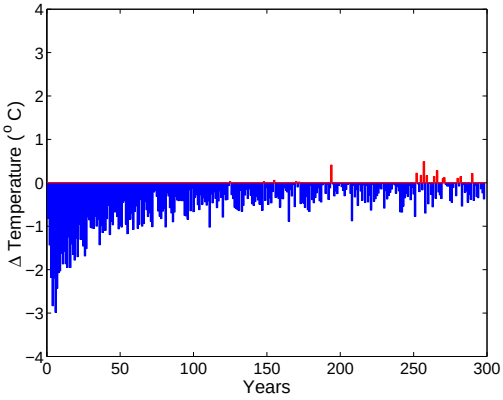

(f) South Asian region (11.8^o C)

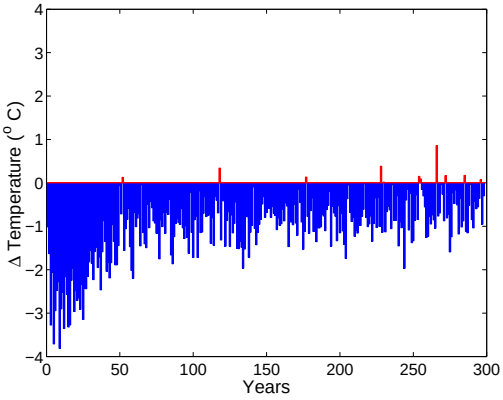

(g) Europe region (5.2^o C)

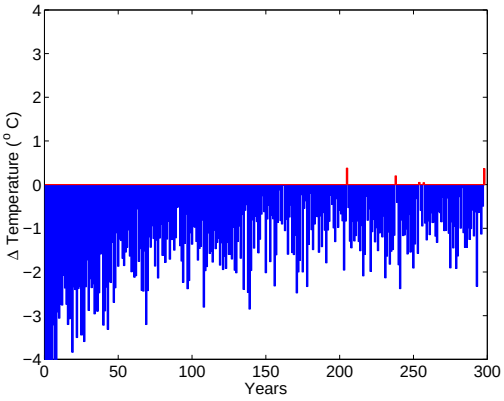

(h) Northern North America (-5.0^o C)

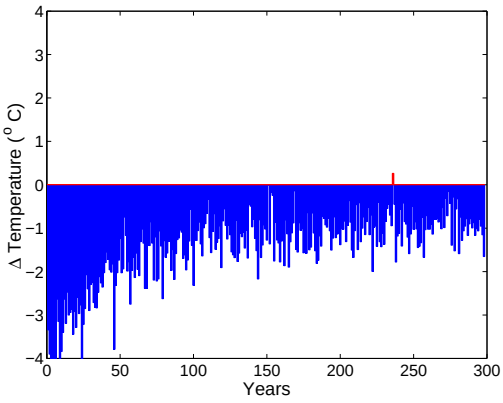

(i) North Asian region (-7.5^o C)

Figure 5.2 *Changes in the annual mean regional 1.5 m air temperature, throughout the 300 year GCM experiment. Air temperatures are plotted as the difference with the pre-agricultural control simulations, for the different regions. The pre-agricultural mean temperatures are given in the sub-figure captions.*

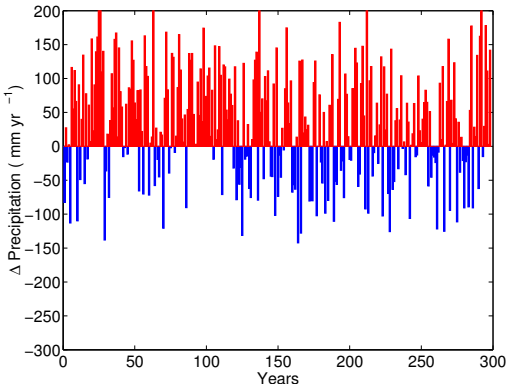

(a) Australian region (408 mm yr^{-1})

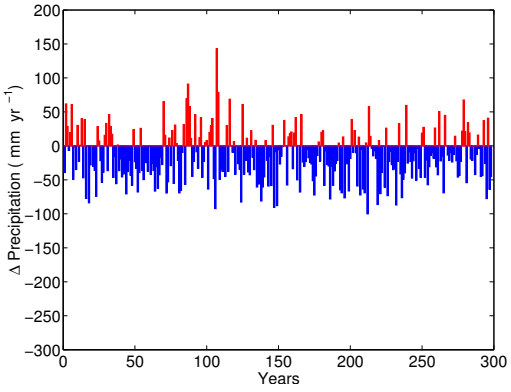

(b) North Africa region (198 mm yr^{-1})

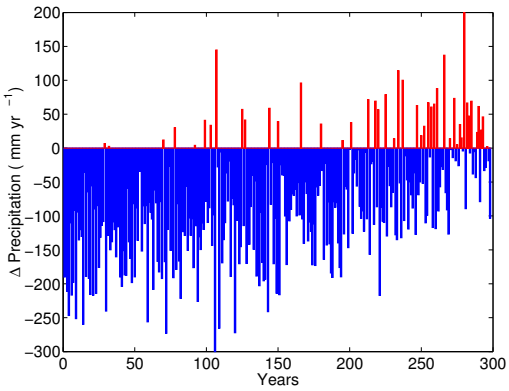

(c) South Africa region (1101 mm yr^{-1})

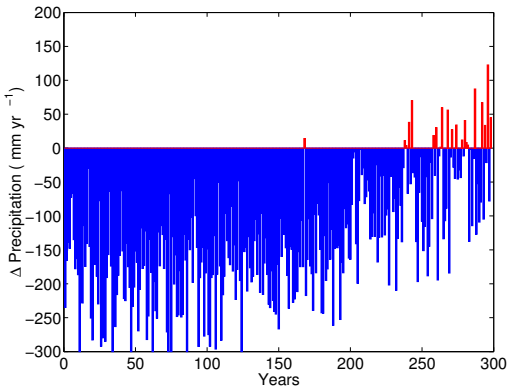

(d) South America region (1556 mm yr^{-1})

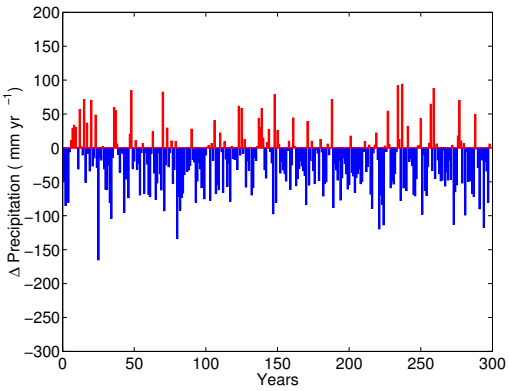

(e) Southern North America (861 mm yr^{-1})

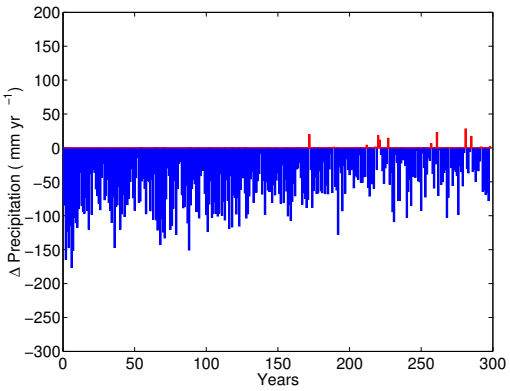

(f) South Asian region (809 mm yr^{-1})

Analysis of the mechanisms involved in the changes in tropical climate is limited to retrospective descriptions. However it is useful to understand the changes in more detail. The observed cooling

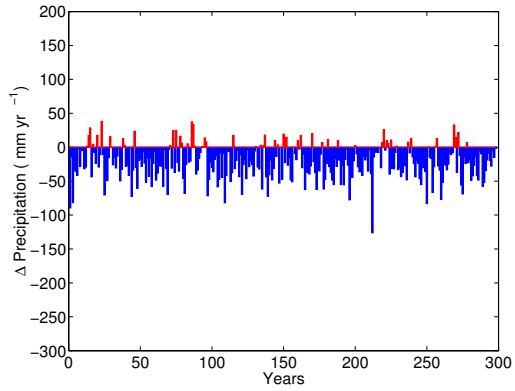

(g) Europe region (688 mm yr^{-1})

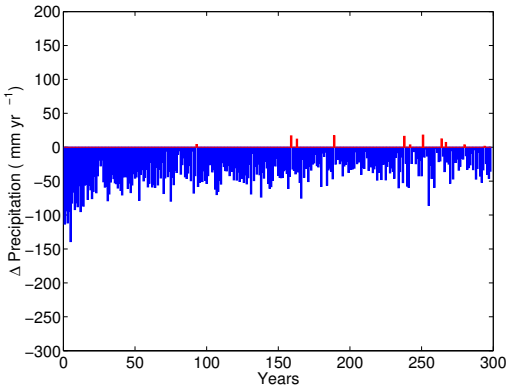

(h) Northern North America (671 mm yr^{-1})

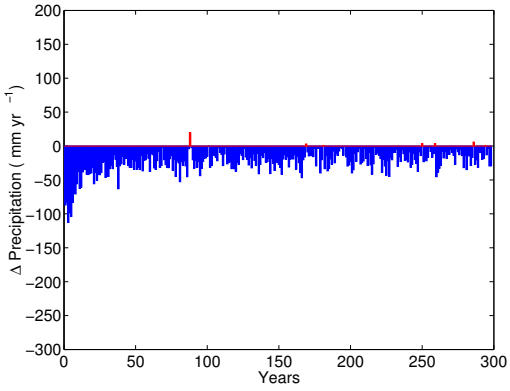

(i) North Asian region (429 mm yr^{-1})

Figure 5.3 *Changes in the annual mean regional precipitation rates, throughout the 300 year GCM experiment, compared to the precipitation rates simulated by the pre-agricultural control simulation, for the different regions. The pre-agricultural climate values are given in brackets in the caption of each sub-figure.*

and increased precipitation associated with the introduction of tropical tree PFTs is similar to that observed by Osborne *et al.* (2003). Osborne *et al.* (2003) used HadAM3 (prescribed SSTs) and prescribed vegetation distributions to quantify the equilibrium impact of tropical vegetation removal. The simulations described by Osborne *et al.* (2003) demonstrate that tropical vegetation cools the land surface by enhancing latent heat fluxes. The effects of vegetation on the local climate have been investigated in detail for the Amazon region in previous studies. Zeng *et al.* (1996) review simulations of the response of the climate to deforestation of the Amazon basin including 13 modelling studies (in this case deforestation is the removal of trees and replacement by grassland). This review shows that Amazon trees act to cool the local climate (on average 1.3^o C), increase the evaporative flux of moisture (by 248 mm year^{-1} on average), and increase precipitation (by 326 mm year^{-1}).

In the current experiment the re-growth of tree PFTs result in a decreases of the surface albedo by 4.5% (averaged over the South America and South Africa regions), and increases the average roughness length from 0.25 m to 0.70 m by the end of the simulation. The increased roughness length enhances surface fluxes of momentum and moisture. With the re-growth of tree PFTs in South America and South Africa the surface wind magnitude decreases by 0.4 m s^{-1} (17 % of the final wind strength). The surface evaporation increases by 150 mm year^{-1}. This increase in evaporation from the surface is compensated for by increased precipitation (approximately 150 mm year^{-1} also), and the mean soil moisture content over South America and South Africa increases by 5 kg m^{-2} during the period of tree PFT re-growth. The average moisture convergence (P-E) is largely unaltered by the re-growth of trees in the two regions as the increase in precipitation and evaporation approximately balance, but the increase in soil moisture suggests enhanced moisture convergence.

5.3.3 Sub-tropical Forest Atmosphere

Figures 5.2(e) and 5.2(f) show the mean 1.5m air temperatures for the Southern North America and South Asia regions. In both regions there is an initial decrease in air temperature ($\sim$ 1-2 ^{o} C), followed by a recovery, on the same timescales as the re-growth of the shrub PFT, see figs.

4.6(e) and 4.6(f). As the shrub PFT re-grows the mean air temperature in these regions increases by 1.0^oC. After this increase in temperature (which occurs in the first 75 years) the local climate remains 0.7^o C cooler than the pre-agricultural control climate in Southern North America. In South Asia there is a slight warming by the end of the simulation.

Figures 5.3(e) and 5.3(f) show the evolution of precipitation rates throughout the simulation, for the Southern North America and South Asia regions. The Southern North American precipitation rate is trend-free throughout the simulation, and is less than, but close to the pre-agricultural rate. In the South Asia region broadleaf trees re-grow during the simulation, fig. 4.6(f), enhancing precipitation rates, which are initially around 150 mm yr^{-1} less than the control simulation, but after 300 years the precipitation rate is close to the pre-agricultural rate.

5.3.4 Boreal regions Atmosphere

Vegetation succession in Europe, Northern North America, and North Asia are characterised initially by a re-growth of C3 type grass, which is then displaced by shrub. Shrub re-growth is fastest in Europe (after 30 years), then Northern North America (after 60 years), with the slowest re-growth of shrub in North Asia (after 140 years; figs. 4.6(g), 4.6(i), and 4.6(h)).

Figures 5.2(g), 5.2(h), and 5.2(i) show the 1.5m air temperatures for Europe, North Asia, and Northern North America. All regions remain colder than the pre-agricultural air temperatures throughout the simulation. The temperature plots are characterised by the initially rapid warming, $\sim 2^o$ C, followed by a more gradual rise in air temperature. The initial rise in air temperatures is fastest in Europe, then North Asia, and Northern North America recovers most slowly, corresponding to the different re-growth timescales of the shrub PFT, figs. 4.6(g), 4.6(i), and 4.6(h).

Figures 5.3(g), 5.3(h), and 5.3(i) show the precipitation rates for Europe, North Asia, and Northern North America. The recovery from the initial bare soil conditions act to restore the

pre-agricultural precipitation rate. Europe recovers quickest, then North Asia, and Northern North America recovers towards the pre-agricultural state slowest. This corresponds to the times taken for shrubs to re-grow. Averaged over the three regions the roughness length is 0.30 m less than the pre-agricultural equilibrium surface roughness length at the end of the simulation, and the surface albedo is 2.1 % greater than the pre-agriculture equilibrium albedo. It is almost certain that the reduced surface fluxes of moisture and momentum and the reduced absorbed surface radiation result in the observed differences in the surface climatology.

Previous studies have also demonstrated the warming effect of the boreal forest. Studies such as Bonan *et al.* (1992), Foley *et al.* (1994), and Betts (2000) show that the change in surface albedo associated with the presence boreal forests act to warm the climate in these regions (see chapter 1).

5.4 Offline Land surface experiments

In the HadSM3-TRIFFID experiment, the atmosphere is significantly altered by the changing land surface properties (see sections 5.2 and 5.3). From the previous discussion it might be hypothesised that this alters photosynthesis rates, changing the rates of vegetation growth; this is supported in fig. 4.7, which shows a spread of τ values, and the related variability of local climates in temperature and precipitation. The environmental dependency of τ was also predicted in chapter 3. It is therefore important to investigate further the sensitivity of growth rates to changing land surface properties.

In order to investigate the importance of the effect of vegetation on it's own re-growth timescales, an offline, single grid box version of the MOSES2 scheme (containing the TRIFFID model) was forced with pre-agricultural surface datasets of net downward shortwave and longwave radiation, precipitation, horizontal wind components, 1.5m air temperature, specific humidity and surface pressure. For a description of the offline version of the surface exchange scheme see Essery *et al.* (2001). Tropical forest was selected for this investigation because a tree PFT dominated region has the longest response time. Also, tropical forest had largely re-grown by the end of the 300

year GCM experiment. Boreal forest had not fully re-grown, so tropical forest is more suitable for comparison. A tropical forest region was also preferable to a boreal forest region because of the clear effect of tropical forest re-growth on the atmosphere, increasing equatorial precipitation (section 5.3). The particular grid box was chosen to be located in central Amazonian because of the hypothesised die-back of the Amazon forest area (White *et al.* (1999), Cramer *et al.* (2001), Cox *et al.* (2001), Betts *et al.* (2003)). The grid point is located at 56.25^o W, 7.50^o S and covers a region of 3.75^o longitude by 2.50^o latitude. The forcing dataset is 20 years long with 30 minute temporal resolution, but was repeated to produce 300 years of data. This method is similar to the approach used by Sitch *et al.* (2003), who model re-growth from bare soil of the terrestrial carbon cycle, ignoring vegetation-atmosphere feedbacks. Using the offline model, vegetation was initialised as bare soil and then allowed to re-grow, mimicking the original HadSM3-TRIFFID experiment (which will be referred to as the GCM experiment in the following sections). The forcing data is firstly derived from the pre-agriculture GCM simulation, and hence does not include vegetation feedbacks. This offline experiment will be referred to as the CTL experiment. Comparing the re-growth timescales from this pre-agricultural offline simulation to the original experiment quantifies the feedback effect of vegetation on it's own timescales. The offline model was also forced with a dataset derived from a global bare soil GCM simulation, as simulated by the HadSM3 model, and this will be referred to as the BS experiment.

Figure 5.4 shows how the broadleaf tree PFT re-grows in the BS and CTL experiments, and compares it to the fully interactive GCM simulation. In the CTL experiment the broadleaf tree re-grows fully by the end of the simulation. At this grid box the broadleaf tree had not fully re-grown during the GCM simulation, reaching 60 % coverage after 300 years. In the BS experiment the broadleaf tree re-grows more slowly, only reaching 24 % coverage by the end of the 300 years. This shows that the re-growth of tropical broadleaf tree is quickest during the CTL experiment, and that the effect of the bare soil perturbation is to reduce the speed of broadleaf PFT response. A key property of the TRIFFID vegetation model is that the photosynthesis model is directly coupled to the population model which predicts the rates of expansion (see chapter 3). In the CTL experiment the mean broadleaf net primary productivity (NPP) is 3.4×10^{-8} kg C m^{-2} s^{-1}. During the GCM experiment, the mean NPP of the broadleaf tree is 2.1×10^{-8} kg C m^{-2} s^{-1}. During the BS experiment the mean NPP of the broadleaf tree is 1.7×10^{-8} kg C m^{-2} s^{-1}.

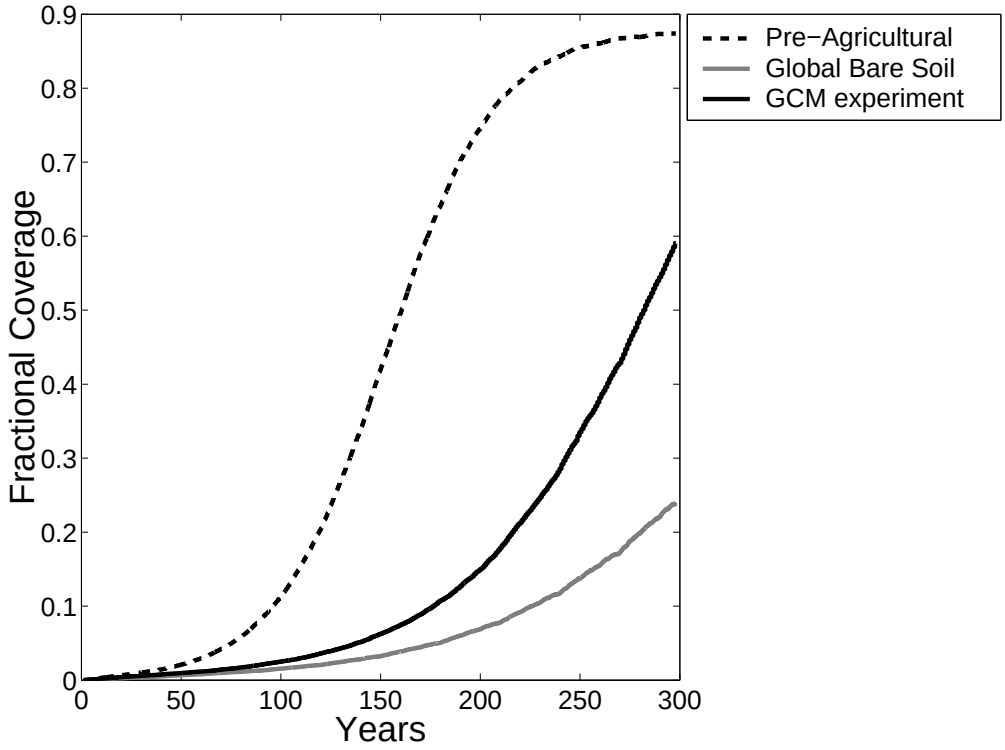

Figure 5.4 *Simulations for the Amazon region using the offline surface exchange TRIFFID scheme simulating re-growth of broadleaf tree fractional coverage under pre-agricultural climate(CTL experiment) and atmospheric conditions consistent with global deforestation conditions (BS experiment). Also included is the fractional coverage of broadleaf tree throughout the GCM experiment.*

Comparing the CTL and BS offline re-growth experiments shows that vegetation-atmospheric feedbacks not only act to increase the possible amount of vegetation supported (shown by Betts (1999)), but that, at least in the Amazon region, vegetation feedbacks act to increase the speed of response of the broadleaf tree PFT.

The simplified model described in chapter 3 is used to validate the hypothesis that the reduced values of NPP cause the reduced rates of recovery. The simple model was constrained to re-grow at approximately the same rate as the re-growth under pre-agricultural climate (CTL) when NPP is set to 3.4×10^{-8} kg C m^{-2} s^{-1} ($\overline{NPP}$ during the pre-agricultural re-growth, from the offline model). Without changing any other model parameter the simple model was re-run for the two

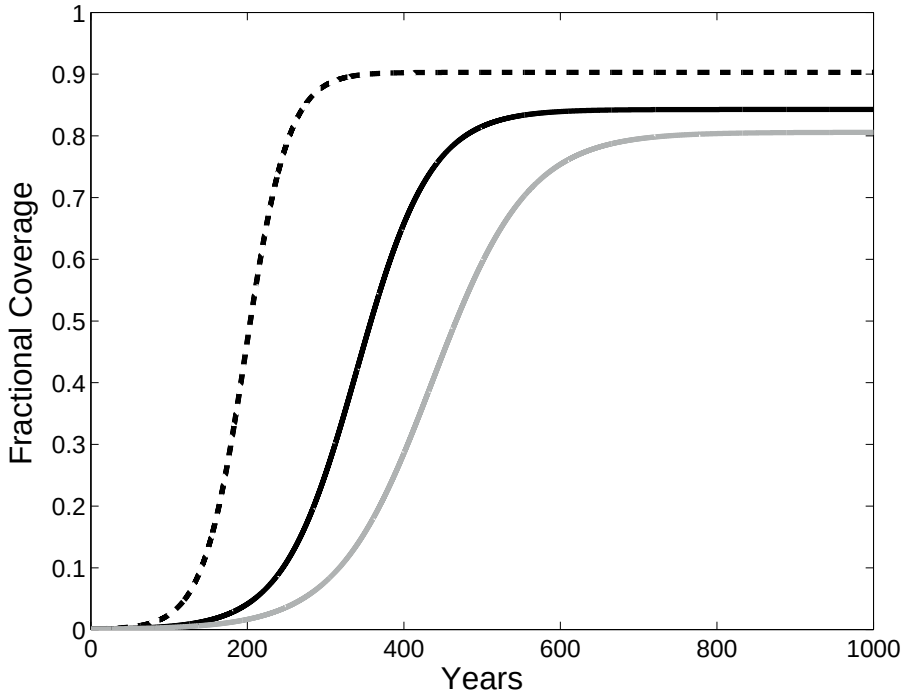

Figure 5.5 *The offline test reproduced with the simple model developed in chapter 3. Re-growth when the model is forced by pre-agricultural forcing is shown as the dashed black line. The GCM experiment re-growth is shown with the solid black line. Re-growth under global bare soil conditions (BS) is shown with the solid grey line. The simple model was constrained to fit the re-growth of broadleaf tree under pre-agricultural climate (CTL). The other runs were obtained by setting the NPP value to that of the mean NPP simulated in the more complex experiments (BS and GCM experiments).*

other values of $\overline{NPP}$, corresponding to $\overline{NPP}$ from the GCM experiment and from the BS offline experiment. These three runs of the simplified model are shown in fig. 5.5. Figure 5.5 shows that the reduced NPP does cause the reduced rates of recovery. The final steady state of fractional coverages also decreases with decreasing NPP, which is consistent with the steady state analysis of the simplified model in chapter 3, and with the general self-beneficial behaviour of vegetation simulated by Betts (1999). This analysis clearly shows that the simplified model of chapter 3 has successfully distilled the essential processes of TRIFFID, and highlights the dominant role that NPP plays.

It has now been shown that the re-growth of vegetation is sensitive to environmental conditions. By running the offline models it was shown that the re-growth of broadleaf tree in the GCM experiment is slower than in the CTL experiment, and faster than under global desert climate, due to the induced changes in the climate. The mean NPP values presented show decreasing NPP values with increasing re-growth rates which is consistent with the analysis of the simplified model presented in chapter 3. This mechanism was then reproduced using the simplified model. The next stage is to investigate the cause of the reduction in NPP.

The offline surface exchange scheme, which includes the vegetation model, is forced with 8 environmental variables : shortwave radiation flux, longwave radiation flux, precipitation, air temperature at 1.5 m, horizontal wind components at 1.5 m, surface pressure, and the atmospheric humidity content at 1.5 m height. The state of the different climates are summarised for the three experiments in table 5.1. The soil moisture profiles in table 5.1 show the soil moisture profiles in the original climate simulations that generated the forcing data (and therefore which affect the physical state of the surface energy balance). The soil moisture profiles calculated during the offline experiments are shown in table 5.2, because these soil moisture values directly modulate photosynthesis values (see section 2.2.3). The choice of means in summarising the climate in CTL and BS experiments is a reasonable first approximation of the climates, as neither experiments exhibit significant trends. As was discussed in section 5.3, and shown in fig. 5.2(d), the 1.5m air temperature exhibits an initial warming of the order of 1 ^{o} C, and a systematic cooling of the order of 0.5 ^{o} C during the last 150 years of simulation over the South America region. The South American region also experiences a substantial increase in precipitation (around 200 mm yr^{-1}) in the last 150 years, as shown in fig. 5.3(d). These changes in climate show that there are substantial trends in the climate dataset, and the mean climate is a less representative measure of the state of the atmosphere during the GCM experiment.

The climate values shown in table 5.1 reflect the variation in photosynthesis values (NPP$_{CTL}$ $>$ NPP$_{GCM}$ $>$ NPP$_{BS}$). The precipitation is least during the BS experiment and most for the CTL experiment. A similar trend is observed in air temperature, where the BS experiment

Variable	CTL	GCM	BS
Net shortwave flux (W m^{-2})	188.9	187.7	201.0
Net longwave flux (W m^{-2})	48.6	58.1	82.9
Precipitation (mm yr^{-1})	2071	1534	1462
Air Temp (^oC)	24.8	27.4	30.1
Horizontal wind magnitude (m s^{-1})	0.82	2.09	3.73
Surface Pressure (mb)	1008	1003	1007
Latent heat flux (W m^{-2})	113.0	89.4	73.4
Soil moisture 0.10 m (kg m^{-3})	330.4	296.4	195.0
Soil moisture 0.25 m (kg m^{-3})	326.8	282.4	188.9
Soil moisture 0.65 m (kg m^{-3})	317.8	285.0	266.1
Soil moisture 2.00 m (kg m^{-3})	310.4	306.1	276.1

Table 5.1 *The mean climatic forcing conditions for the surface exchange scheme at the single Amazon grid box. CTL is the pre-agricultural offline dataset. BS is the global desert forcing dataset, and GCM are the conditions from the GCM re-growth experiment. Soil levels are arranged in order of proximity to the surface, the distances are the thickness of the layer. The soil moisture values correspond to those predicted in the original climate simulations, and only affect the physical environment, as the offline model recalulates the soil moisture content. Air temperatures are very similar ($< 0.2\ ^o$ C difference) to the surface temperatures.*

is the hottest and CTL is the coolest. The soil moisture content and the latent heat flux from the surface also follow the same trend as the precipitation values. Wind strength increases such that BS $>$ GCM $>$ CTL, which is consistent with the fact that the roughness length is least in this experiment. The differences in net longwave radiation flux relect differences in the surface temperature (which is approximately equal to the air temperature). The net shortwave flux is also greatest during the BS experiment, and is probably related to changes in the surface albedo.

Comparing tables 5.1 and 5.2 for the BS experiment shows that the presence of vegetation acts to increase the amount of water retained in the soil. The CTL experiment soil moisture values

Variable	CTL	BS
Soil moisture 0.10 m (kg m^{-3})	347.0	267.0
Soil moisture 0.25 m (kg m^{-3})	348.4	293.2
Soil moisture 0.65 m (kg m^{-3})	353.7	297.4
Soil moisture 2.00 m (kg m^{-3})	366.4	340.6

Table 5.2 *The mean soil moisture properties as calculated in the offline model. These values influence the vegetation photosynthesis estimates, whilst those in the previous table influence the physical environment.*

in tables 5.1 and 5.2 shows that because vegetation is re-growing in the CTL offline experiment, and is already established in the original experiment soil moisture content is reduced.

The association of trends in the climate variables does not imply causality. One possible interpretation of the values presented in table 5.1 would be that the changes are largely driven by changes in the precipitation associated with changes in the land surface properties (both local and remote), and that the photosynthesis changes are dominated by changes in the surface hydrology. A full investigation of the mechanisms involved in these changes to the environment will not be presented here, however it is clear that the environment does change, and whilst table 5.1 is qualitatively in agreement with the photosynthesis values it will be useful to investigate the photosynthesis mechanisms in detail. Investigating the mechanisms driving the changes in environment in detail would require further offline studies, and would involve repeating the 300 year GCM experiment, storing the forcing conditions for the offline model at each timestep (allowing multiple re-runs of the surface state).

Table 5.3 shows diagnostics from the terrestrial carbon cycle. Values from all PFTs have been included to demonstrate the variability of diagnostics, and to show the behaviour of the total land surface. The carbon balance of broadleaf tree is the primary focus, however. The mean photosynthesis rate (GPP) increases for all PFTs such that $\text{GPP}_{BS} < \text{GPP}_{GCM} < \text{GPP}_{CTL}$. The mean photorespiration (plant respiration) is maximum during the GCM experiment, though plant

Variable	BL	NL	C3	C4	SH
BS experiment					
GPP (Kg C m^{-2} s^{-1})	5.0×10^{-8}	1.8×10^{-8}	5.4×10^{-8}	8.9×10^{-8}	2.8×10^{-8}
Plant respiration (Kg C m^{-2} s^{-1})	3.4×10^{-8}	1.1×10^{-8}	3.7×10^{-8}	3.4×10^{-8}	1.6×10^{-8}
NPP (Kg C m^{-2} s^{-1})	1.7×10^{-8}	6.4×10^{-9}	1.7×10^{-8}	5.5×10^{-8}	1.2×10^{-8}
Plant turnover rate ($year^{-1}$)	2.5×10^{-1}	2.5×10^{-1}	2.5×10^{-1}	2.5×10^{-1}	2.5×10^{-1}
GCM experiment					
GPP (Kg C m^{-2} s^{-1})	6.4×10^{-8}	2.4×10^{-8}	7.9×10^{-8}	1.2×10^{-7}	3.9×10^{-8}
Plant respiration (Kg C m^{-2} s^{-1})	4.3×10^{-8}	2.0×10^{-8}	5.3×10^{-8}	4.3×10^{-8}	2.3×10^{-8}
NPP (Kg C m^{-2} s^{-1})	2.1×10^{-8}	4.4×10^{-9}	2.6×10^{-8}	8.0×10^{-8}	1.6×10^{-8}
Plant turnover rate ($year^{-1}$)	2.5×10^{-1}	2.5×10^{-1}	2.5×10^{-1}	2.5×10^{-1}	2.5×10^{-1}
CTL experiment					
GPP (Kg C m^{-2} s^{-1})	7.6×10^{-8}	3.5×10^{-8}	9.0×10^{-8}	1.2×10^{-7}	4.9×10^{-8}
Plant respiration (Kg C m^{-2} s^{-1})	4.2×10^{-8}	1.8×10^{-8}	5.0×10^{-8}	4.3×10^{-8}	2.3×10^{-8}
NPP (Kg C m^{-2} s^{-1})	3.4×10^{-8}	1.6×10^{-8}	4.0×10^{-8}	8.1×10^{-8}	2.6×10^{-8}
Plant turnover rate ($year^{-1}$)	2.5×10^{-1}	2.5×10^{-1}	2.5×10^{-1}	2.5×10^{-1}	2.5×10^{-1}

Table 5.3 *Vegetation structure variables for BS, CTL, and GCM experiments at the single Amazon grid box. GPP is the gross primary productivity, and is the mean photosynthesis. Plant respiration is the mean photorespiration. NPP is the net primary productivity, and is the difference between photosynthesis and photorespiration. The plant turnover rate determines the rate of loss of carbon from the plant carbon pool. BL is broadleaf tree. NL is needleleaf tree. C3 is C3 type grass. C4 is C4 type grass. SH is shrub.*

respiration is greater in CTL than in the BS experiment. The balance between photosynthesis and photorespiration (NPP) is such that $\text{NPP}_{BS} < \text{NPP}_{GCM} < \text{NPP}_{CTL}$ for all PFTs other than needleleaf trees, where although the maximum NPP is during the CTL experiment, $\text{NPP}_{BS} > \text{NPP}_{GCM}$ (the difference is 2.0×10^{-9} kg C m^{-2} s^{-1}). This fact, in connection with the simple model run shown in fig. 5.5 suggests that needleleaf PFT coverage (which is small at these latitudes) would take longer to re-grow in the GCM experiment than in the BS experiment, this is consistent with the fact that needleleaf trees grow in colder environments. Table 5.3

therefore shows that the photosynthesis increased in the order BS to GCM, to CTL, and although photorespiration also increased this still resulted in an increased NPP, and hence an increased re-growth timescale. Table 5.3 also shows that the leaf turnover rate is equal to the minimum turnover rate, γ_o in Cox (2001), which is a constant value. This shows that increased turnover rates due to the phenological model are not important during these experiments. Photorespiration is a function of temperature and is proportional to Vm, which was described in chapter 2, fig. 2.1.

In chapter 2 the photosynthesis scheme was described. The photosynthesis rate is the minimum of three terms, limitation by the photosynthetic enzyme system (Wc), by the rate at which photosynthetic products can be exported, or PEP enzyme limited (We), and light limited (Wl). It is possible to extract these three terms from the offline simulations, BS and CTL. Estimates of the individual terms are not available from the GCM experiment. Tables 5.4 and 5.5 summarise the different terms for the BS and CTL offline experiments and their mean values. By investigating the individual limiting terms the sensitivity of the photosynthesis model to environmental conditions during the offline experiments can be quantified.

Variable	Wc (%)	We (%)	Wl (%)	$\overline{Wc}$	$\overline{We}$	$\overline{Wl}$	$\overline{Wmin}$
Broadleaf tree	74	0	26	5.9×10^{-6}	1.6×10^{-5}	2.4×10^{-5}	4.8×10^{-6}
Needleleaf tree	82	0	18	2.6×10^{-6}	6.9×10^{-6}	2.0×10^{-5}	2.2×10^{-6}
C3 grass	61	0	39	9.2×10^{-6}	2.4×10^{-5}	2.5×10^{-5}	6.7×10^{-6}
C4 grass	57	2	41	1.8×10^{-5}	6.6×10^{-5}	2.9×10^{-5}	1.4×10^{-5}
Shrub	78	0	22	4.5×10^{-6}	1.2×10^{-5}	2.4×10^{-5}	3.7×10^{-6}

Table 5.4 *The fractions of the simulation for which each limiting factor was the minimum, for the BS Amazon offline re-growth experiment, and the mean values for the different photosynthesis values (kg C m^{-2} s^{-1}), including the minimum of the different terms. On average Wc is the dominant limiting term for 70 % of the simulation. Wl is the dominant limiting term for the remaining 30 % of the simulation.*

Although the photosynthesis model is light saturated at around 150 W m^{-2} (see chapter 2, fig.

Variable	Wc (%)	We (%)	Wl (%)	$\overline{Wc}$	$\overline{We}$	$\overline{Wl}$	$\overline{Wmin}$
Broadleaf tree	69	0	31	7.7×10^{-6}	1.7×10^{-5}	2.8×10^{-5}	6.2×10^{-6}
Needleleaf tree	77	0	23	3.8×10^{-6}	8.7×10^{-6}	2.5×10^{-5}	3.1×10^{-6}
C3 grass	60	0	40	1.2×10^{-5}	2.6×10^{-5}	2.8×10^{-5}	8.7×10^{-6}
C4 grass	60	0	40	1.6×10^{-5}	6.9×10^{-5}	2.6×10^{-5}	1.2×10^{-5}
Shrub	75	0	25	5.8×10^{-6}	1.3×10^{-5}	2.8×10^{-5}	4.8×10^{-6}

Table 5.5 *The fractions of the simulation for which each limiting factor was the minimum, for the CTL Amazon offline re-growth experiment, and the mean values for the different photosynthesis values (kg C m^{-2} s^{-1}), including the minimum of the different terms. On average Wc is the dominant limiting term for 68 % of the simulation. Wl is the dominant limiting term for the remaining 32 % of the simulation. Note: C4 grass is limited by We during 0.002 $\%$ of the simulation.*

2.2(c)), tables 5.4 and 5.5 show that light limitation is an important limiting factor over the simulation. This is associated with the daily variations in shortwave radiation. The importance of the daily cycle in shortwave radiation was validated by re-running the CTL experiment, with the shortwave forcing data replaced with a running mean of the previous 24 hours (48 timesteps). When this is done the vegetation model crashes. This shows the importance of the representation of the daily cycle of shortwave radiation in the photosynthesis model. The We limitation factor is of negligible importance during these experiments. From the photosynthesis eqns. (eqns. 2.20 and 2.21) in chapter 2, it can be shown that light availability becomes the limiting factor when:

$$I_{PAR} < \begin{cases} V_m \frac{c_i - 2\Gamma}{0.681(c_i + K_c(1+\frac{O_a}{K_o}))} & \text{C3 plants} \\ V_m \frac{1}{0.03321} & \text{C4 plants} \end{cases} \tag{5.1}$$

The different variables are defined in chapter 2.

When photosynthesis is dominated by the RuBP enzyme system (Wc), *i.e.* when equality 5.1 is not satisfied, photosynthesis is proportional to the maximum rate of photosynthesis, Vm. Vm is a function of temperature, with an optimum value for broadleaf tree PFT of 32 ^{o} C (see chapter 2). However, from the temperature values in table 5.1 we can see that Vm increases CTL $<$ GCM

$<$ BS, the opposite direction to increases in GPP. This means that the increased GPP observed for the broadleaf tree PFT is not caused by temperature. For C4 type photosynthesis, the Wc limitation term is equal to Vm, and comparing values for C4 Wc photosynthesis for the BS and CTL experiments we see that $\mathrm{Wc}_{(BS)} > \mathrm{Wc}_{(CTL)}$. For all C3 type photosynthesis $\mathrm{Wc}_{(BS)} < \mathrm{Wc}_{(CTL)}$, implying that another environmental variable offsets the increase in Vm. Other than temperature and light, C3 type photosynthesis is also linearly dependent on the canopy level humidity deficit, ΔQ. ΔQ affects the internal CO_2 concentration, this relationship is defined in eqn. 2.25. The humidity deficit values are not available for the GCM experiment, but they are available for the CTL and BS offline experiments. Table 5.6 shows the humidity deficit values for these two offline experiments.

Variable	Broadleaf	Needleleaf	C3 grass	C4 grass	Shrub
BS	12.0	13.3	11.5	10.8	12.0
CTL	4.7	5.8	3.4	3.4	4.2

Table 5.6 *Humidity deficits, ΔQ (g kg^{-1}) for the BS and CTL offline experiments, for each PFT.*

The values of ΔQ in table 5.6 show that BS photosynthesis is uniformly more limited by ΔQ than experiment CTL. Equation 2.25 shows that as ΔQ increases the internal CO_2 pressure decreases, reducing C3 type photosynthesis. The cause of the variation of growth timescales is therefore dependent on the canopy humidity deficit, which is a function of the surface hydrology. In order to test this dependency the CTL offline experiment was repeated, with the 1.5 m humidity content reduced by 5%. When this experiment is performed the rate of re-growth of broadleaf tree is reduced, and only reaches 4.5% coverage after 300 years, thus demonstrating that the re-growth is highly sensitive to the surface hydrology.

In order to understand the physical mechanism regulating the re-growth of broadleaf tree in the GCM experiment it would be necessary to force the offline model with the boundary layer climate data directly from the GCM experiment. This would allow detailed investigation of the physical mechanism for NPP value predicted in CTL. Unfortunately only the annual means fields were

available from the GCM experiment, due to the length of the simulation. An attempt was made to reconstruct 30 minute resolution climatological datasets by altering the climate datasets from the CTL offline experiment so that the annual means equal those of the GCM experiment. When this is done the predicted re-growth of broadleaf tree is very slow, less than even the BS offline experiment. In this experiment broadleaf tree has re-grown to 8.7% coverage after 300 years. The problem with the approach taken to reconstruct the 30 minute resolution climate datasets is that the physical coupling between the climate fields is not preserved.

5.5 Large scale variations in timescales

In the previous section it was shown that τ decreases with increasing NPP. This relationship can then be used to qualitatively investigate global τ values on the global scale in the 300 year GCM experiment. Figure 5.6 shows the difference between the average NPP during the GCM experiment and the pre-agricultural control. The patterns of NPP are associated with global differences in surface climatology. The global mean NPP over land (ignoring permanent ice regions) increases uniformly, such that $\text{NPP}_{GCM} < \text{NPP}_{CTL}$, for each PFT. The global mean NPP values over land not covered by permanent land ice, for each PFT are: 7.3×10^{-10} kg C m^{-2} s^{-1} for broadleaf tree, 8.7×10^{-10} kg C m^{-2} s^{-1} for needleleaf tree, 1.6×10^{-9} kg C m^{-2} s^{-1} for C3 type grass, 1.4×10^{-9} kg C m^{-2} s^{-1} for C4 type grass, and 9.8×10^{-10} kg C m^{-2} s^{-1} for the shrub PFT. As the average NPP values are larger in the control simulation, it follows from the previous section that the average characteristic timescale for each PFT should be smaller in the control simulation, than during the 300 year GCM experiment. Figure 5.6 also shows, however, that in some regions $\text{NPP}_{GCM} > \text{NPP}_{CTL}$. In those regions the re-growth from bare soil would take longer under pre-agricultural climate, than during the 300 year GCM experiment. Considering the steady state vegetation distributions under pre-agricultural climate, as shown in fig. 4.1 it is clear that those regions where $\text{NPP}_{GCM} > \text{NPP}_{CTL}$ correspond to the bare soil regions under pre-agricultural climate.

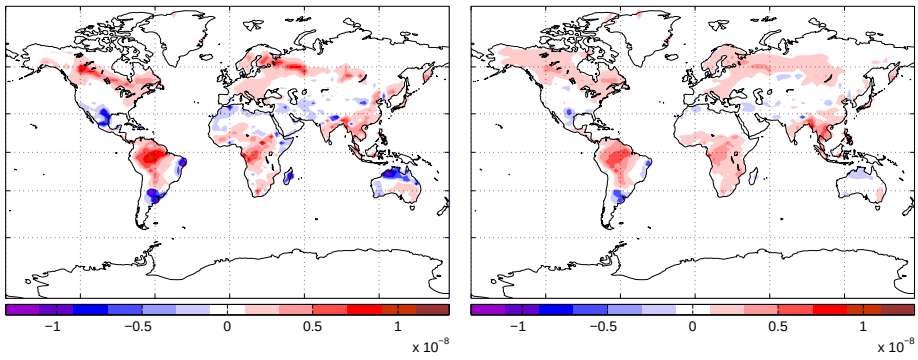

(a) Broadleaf tree

(b) Needleleaf tree

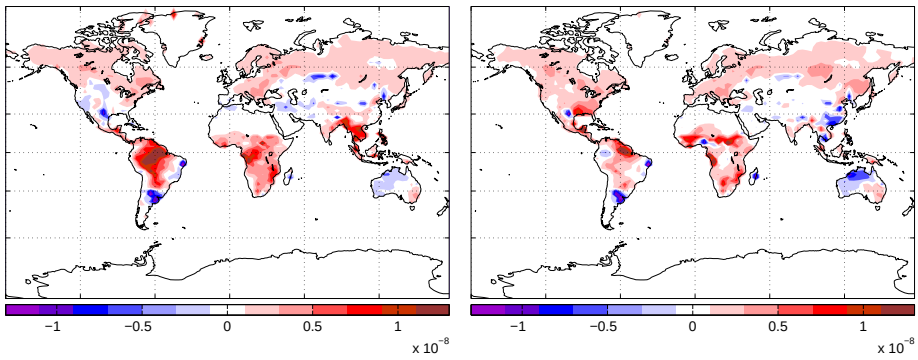

(c) C3 type grass

(d) C4 type grass

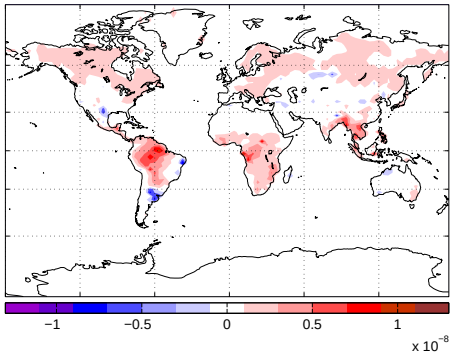

(e) Shrub

Figure 5.6 *Changes in NPP (kg C m^{-2} s^{-1}) for each PFT. The fields plotted are pre-agricultural control minus the average NPP during the 300 year GCM re-growth experiment.*

5.6 Conclusions

In the previous chapter the re-growth of the terrestrial biosphere was simulated using the HadSM3 GCM, which includes the TRIFFID DGVM. In this chapter analysis of this experiment is extended. The surface climatology throughout the simulation is investigated. The most noticeable effect is an increase in tropical precipitation, associated with the re-growth of the tropical forests. Although it is not possible to deduce a causal mechanism, it seems likely that this increase in precipitation causes (rather than is driven by) a reduction in air temperature. In general, by analysing regional changes in the near-surface climatology the link between climate trends and the composition of land surface vegetation has been established. The importance of vegetation re-growth timescales for atmospheric change has been demonstrated.

From the growth timescale analysis presented in chapter 3 it was hypothesised that changes in the atmosphere induced by the initial land surface perturbation could affect the re-growth timescales of vegetation. As these timescales have been shown to have an important effect on the atmosphere it was important to quantify this effect.

Vegetation in an offline, single grid box model was allowed to re-grow from bare soil conditions. When the re-growth of broadleaf tree at the single grid box is compared for these three experiments a large change in the re-growth timescales is observed. These experiments show that the broadleaf tree re-growth timescale was slower in the GCM experiment than under pre-agricultural control climate, but in both of these experiments, the re-growth of broadleaf tree was more rapid than when the offline model was forced with climate datasets in the bare soil experiment. This trend in timescales is reflected in the fact the mean NPP during these experiments are inversely proportional to the observed re-growth timescale, as was predicted in chapter 3. Using the simple model developed in chapter 3 the link between NPP and re-growth timescales was tested. This test also highlights the result that relatively slow re-growth also corresponds to reduced equilibrium coverage of broadleaf tree (also predicted in chapter 3).

Having established that changes in NPP caused the variation in re-growth timescales a more

detailed investigation of the physical cause of the change in NPP was presented. It was shown that the different growth timescales were dominated by changes in the canopy humidity deficit. A sensitivity experiment confirmed this result, and highlighted the importance of the atmospheric humidity content.

The effect of vegetation-atmosphere feedbacks on the re-growth of vegetation has not been investigated before in climatology (see, for example Sitch *et al.* (2003)). The offline model is only run at a single grid box, and the applicability of the results to the global scale requires further experiments. However the investigations presented here show that substantial variations in the growth timescales are possible, and in the particular case of the re-growth of Amazon broadleaf tree PFT, diagnose the physical cause of this variation. As the link between NPP and re-growth timescale has been established by analysing the NPP fields directly, timescales under pre-agricultural control climate and during the 300 year GCM experiment can be quantitatively investigated.

CHAPTER 6

Summary and Future Reseach

6.1 Summary

In this thesis the behaviour of the dynamic vegetation model in the HadSM3 GCM has been investigated. HadSM3 uses a relatively new approach to modelling global vegetation. The Hadley Centre climate models (HadAM3, HadSM3, and HadCM3) are important climate models in current climate research, and so it is vital to be aware of the full effects of including this form of dynamic vegetation into these GCMs, as vegetation has been demonstrated to have an important influence on the behaviour of the climate models.

In analysing the behaviour of vegetation in HadSM3 a hierarchy of 3 models was used. The most simple model only includes the central mathematical components of the dynamic vegetation model. The full GCM, HadSM3 was used to simulate the response of the atmosphere allowing the behaviour of the dynamic vegetation to be investigated within the climate system. An existing offline version of the surface exchange scheme was also used to include realistic representation of the surface processes and to investigate results from the GCM.

In chapter 2 details of the Hadley Centre climate models were reviewed, but also presented in chapter 2 were a series of experiments designed to investigate the sensitivity properties of the GCM. These experiment include two traditional GCM experiments: the response of the GCM to a doubling of atmospheric CO_2, and the effects of imposing global desert land surface conditions. Also presented is an experiment combining both global desert conditions and a doubling of atmospheric CO_2. A pre-agricultural control run was also completed for comparison.

The GCM response to a doubling of atmospheric CO_2 includes a dramatic reduction of Amazonian broadleaf tree PFT. This Amazon die-back has been predicted previously, and was discussed in chapter 1. Previous experiments including the Amazon die-back result were transient predictions of the response of climate to projected anthropogenic emissions using fully coupled dynamic atmosphere-ocean models. Our slab ocean simulation shows that the dynamic behaviour of the ocean is not a key component of the die-back result. This experiment is unique in that it predicts an Amazonian die-back in an idealised doubling of atmospheric CO_2. The fact that the Amazon die-back is captured in the response to a doubling of CO_2 means that when the steady state climate sensitivity to CO_2 is compared with other GCMs sensitivity estimates, the Amazon die-back is included. When the climate response to a doubling of CO_2 is calculated for HadSM3 and compared with other GCMs it is seen that HadSM3 is more sensitive to a doubling of CO_2 than any other GCM. Moreover, by comparing the climatic response to a doubling of CO_2 under global desert conditions it was shown that including vegetation appears to increase the sensitivity of HadSM3 to CO_2. Examination of the spatial contributions to the response to a doubling of CO_2 show that the largest changes in climate are associated with the Amazon die-back. The Amazon die-back result is an example of large-scale rapid restructuring of the terrestrial biosphere, providing motivation for investigating the dynamical behaviour in more detail.

The four GCM experiments discussed in chapter 2 can also be used to investigate the effects of vegetation on climate (control minus global desert) for pre-agricultural CO_2 levels, and also for doubled CO_2 levels. Comparing these two sets of experiments shows that for doubled CO_2 the self-beneficial effect of vegetation (see Betts (1999)) is reduced, apparently due to the Amazon die-back result.

The mathematical properties of the dynamic vegetation model were investigated using a simplified form of the DGVM in chapter 3. The dynamic vegetation model is based on the well-studied Lotka-Volterra equations for competition. Manipulations of the DGVM equations show that the expected transition between different competing PFTs is gradual rather than discrete. By considering the simulated pre-agricultural vegetation distributions it was shown that despite the

prediction of smooth transitions between competing PFTs, under pre-agricultural climate the competing PFTs do not coexist at the same grid box. This is due to different optimum climatic conditions for photosynthesis of the different PFTs, which is further discussed in chapter 4.

By making the assumption that the dominant vegetation behaviour can be modelled by considering only a single PFT, and by simplifying the leaf phenology model a simplified version of the TRIFFID DGVM was derived. This form of TRIFFID was then demonstrated to capture the behaviour of the full complexity TRIFFID model. The simplified model can then be used to elucidate the behaviour of TRIFFID. The initial growth rate, the maximum growth rate, and the intrinsic growth rate were all diagnosed from the simplified TRIFFID equations. The intrinsic growth rate is the growth rate independent of the fractional coverage. The actual growth rate is dependent on the fractional coverage. The actual growth rate is slowest when the fractional coverage is smallest (the initial growth rate), and largest when the fractional coverage is half the maximum coverage (the maximum growth rate), however both of these are determined by the intrinsic growth rate. In the simple model the intrinsic growth rate depends linearly on NPP. The steady state solutions of vegetation structure (carbon density and fractional coverage) were derived. Steady state fractional coverage and vegetation carbon density both increase non-linearly with increasing NPP. The steady state fractional coverage dependency also introduces a threshold effect, and below a critical level of NPP fractional coverage tends to zero. It was also possible to demonstrate the global stability of the TRIFFID model. Global stability is important in that it shows that vegetation does not generate noise.

By reacting to environmental variability TRIFFID may increase the climatic variability relative to a static vegetation structure model. Spectral analysis of the simplified model shows that when TRIFFID is forced with white noise (equal variability over all timescales) the variation in vegetation structure is red noise (the variability decreases with increasing frequency).

A preliminary validation of the timescales involved in the TRIFFID model was attempted by simulating the recovery of needleleaf tree PFT from the 1908 Tunguska meteorite event. The TRIFFID response time to a Tunguska-like reduction of needleleaf fractional coverage of 4%

was shown to be consistent with observations. The observational record for the recovery of forest cover however is poor due to the remote location of the site.

The vegetation distributions under a pre-agricultural climate steady state are presented in chapter 4 and discussed. By plotting functional coverage in climate space the environmental niches of each PFT are described. After analysing the behaviour of the dynamic vegetation model in isolation from the atmosphere in the previous chapter, chapter 4 introduces an experiment using HadSM3 designed to investigate the behaviour of the vegetation model when it interacts with the atmosphere. The experiment sets vegetation cover to global desert land surface conditions. Specifying global desert land surface conditions is a standard experiment designed to investigate the maximum possible effects of vegetation on climate.

In this model simulation the vegetation is allowed to re-grow for 300 years, interacting with the atmosphere. After the 300 years vegetation has not returned to pre-agricultural distributions. This experiment demonstrates the potential for long time lags in the vegetation-atmosphere system (as represented in the HadSM3 model). These timescales are also shown to dominate the terrestrial carbon cycle, controlling the transition from a source of CO_2 into the atmosphere to a sink of CO_2. Considering the predicted Amazon die-back, it is to be expected that using this model to simulate the recovery from Amazon die-back conditions, a similar pattern of source to sink transitions would be simulated.

By fitting the observed re-growth of PFTs to a logistic equation the intrinsic timescale of each vegetation PFT is estimated. In chapter 3 it was shown that this timescale is dependent on the rate of photosynthesis and hence the surface climate. The analysis in chapter 3 did not estimate the range of timescales possible for each PFT. The timescales estimated for each PFT are plotted as a function of the climate in which the PFT re-grows. The distribution of re-growth timescales is shown to be related to the predicted rate of photosynthesis in climate space, supporting the idealised analysis in chapter 3.

After describing the re-growth of vegetation in the previous chapter, in chapter 5 the effects of vegetation-atmosphere interactions on vegetation re-growth timescales is further investigated. To do this an offline version of the surface exchange scheme is used. This allows vegetation to re-grow under pre-agricultural climatic conditions, testing the impact of the global desert perturbation on the re-growth behaviour. The offline model is run at a single grid box. The grid box was chosen to represent central Amazon forest coverage. The offline model was forced with climatology from a previous pre-agricultural control simulation (CTL), and also a steady state global desert land surface conditions simulation (BS). The re-growth of broadleaf tree simulated in the CTL experiment is faster than during the interactive GCM simulation. In the BS offline experiment the re-growth of broadleaf tree is slower than during the interactive GCM simulation. This shows that changes in climate do alter the re-growth rates and the effect can be significant under reasonable changes in climate. The two offline model runs also provide a means of investigating the physical mechanism involved in the change in re-growth timescale. The different limiting mechanisms are investigated, illustrating the importance of light limitation, and limitation by RuBP. The physical mechanism driving the reduced rates of re-growth is shown to be due to increased canopy level humidity deficit, and is therefore related to the hydrology of the land surface rather than directly to temperature (though obviously the two are coupled). Increased steady state vegetation fractional coverage is linked to increased re-growth timescales, as was predicted in chapter 3. This result is consistent with the work of Betts (1999) who showed that vegetation-atmosphere feedbacks increased the amount of vegetation supported by the climate. The global effect of climate on the re-growth timescale is qualitatively investigated by calculating the difference in the global field of NPP during the 300 GCM experiment and the pre-agricultural control simulation. Doing this shows that in most regions NPP (and hence the intrinsic growth rate) is greater under pre-agricultural climate than in the transient GCM re-growth experiment.

6.2 Future research direction

As well as the more general research directions discussed in section 6.3, there are several phenomena which if included into the land surface representation in HadSM3 would increase the realism. The two phenomena discussed here are seed dispersal limitation of forest coverage and

forest fire simulation. Other phenomena that could be considered are the nitrogen limitation of photosynthesis, interactive dust cycling, peat bog formation, and the methane cycle.

6.2.1 Wild fire prediction

After climate and soil properties, wild fire is one of the most important determinants of global vegetation distributions. Woodward and Beerling (1997) categorise the ability to simulate wild fire dynamics as an important benefit of using a DGVM. The Hadley Centre DGVM is currently without a fire component, though work is underway to develop the ability to include the effects of wild fire.

The probability of the occurrence of a wild fire is dependent on the trade off between available fuel (vegetation carbon) and soil moisture. Wild fire probability also increases as a function of atmospheric oxygen content (Beerling and Woodward (2001)). Fire models calibrated against current observations are unlikely to perform well for past-climate simulations where atmospheric oxygen concentrations are different to present day concentrations. Soil moisture is important because a wild fire must evaporate the surface water before woody material can burn; however vegetation requires sufficient moisture to successfully photosynthesise (produce fuel), and the combination of these two effects means that a substantial wildfire requires neither too dry nor too wet conditions (Ricklefs (1997)). Malamud *et al.* (1998) investigate the interactions between fuel and fire extent, using a simple computer model. Malamud *et al.* (1998) show that a reduction in the frequency of fires (either by natural variability or by anthropogenic suppression of wild fires) can lead to a build up of available vegetation carbon. When a wild fire does occur, the area burnt is much larger. It is suggested by Malamud *et al.* (1998) that this effect links the unusually severe forest fires in Yellowstone park in 1988 with the previous policy of fire suppression, causing the build up of fuel. Quinlan *et al.* (2003) investigate the impact of fire frequency in a real ecological system, highlighting the variability in plant species response to burning. Thonicke *et al.* (2001) attempt to model fire within the LPJ-DGVM model. Thonicke *et al.* (2001) ignore the explicit effects of fuel availability, and model the probability of a fire occurring (p) in a particular grid box, on a particular day, as a function of the dead fuel moisture concentration, m ($m \geq 0$), using

eqn. 6.1.

$$p(m) = e^{-\pi(\frac{m}{m_c})^2} \tag{6.1}$$

m_c is the critical value of m above which fire is considered to be absent. The grid box fraction burnt by fire is then assumed to increase exponentially with time. Thonicke *et al.* (2001) suggest that neglecting the effects of fuel-fire dynamics reduces the ability of the model to accurately simulate vegetation in arid regions.

Fire can also be an important component of the global carbon cycle. Page *et al.* (2002) show that wild fires in Indonesia during 1997-1998 doubled the growth rate of atmospheric CO_2. Wild fire also influences the cycling of nutrients (Thonicke *et al.* (2001)). Modelling fire may also provide a valuable method for validating models. Predicted fire disturbances can be validated against satellite observations, for the present day. This method is used by Thonicke *et al.* (2001) to test their global wild fire model. Fire models can also be checked against records of black carbon. Black carbon is a particularly stable form of carbon, produced from incomplete combustion of vegetation and fossil fuels (*e.g.* Schmidt and Noack (2000), Kuhlbusch (1998)). The stability of black carbon means that records of it can provide an important history of fire occurrences, with which to test the DGVM. As has been mentioned, the need for validation of the behaviour of DGVMs is an important focus in the development of DGVMs.

6.2.2 Seed dispersal

The ability for biomes to migrate is an important element of dynamic vegetation modelling (Van Minnen *et al.* (2000)). In TRIFFID it is assumed that at every land-grid box there is a small fraction of each PFT established ($10^{-4}\%$ coverage), *i.e.* it is assumed that vegetation expansion is not limited by population dispersal between grid boxes.

Deglaciation after the ice age left large regions bare and suitable for re-colonisation. In this instance the assumption that each grid box is already seeded with tree PFTs is unrealistic. Paleoecological evidence suggests that the northern hemisphere forests dispersed 1,000 km northward over $10,000$ years (Clark *et al.* (1998)). The results presented in chapter 4 suggest that if a glacial-interglacial experiment were to be run on the existing model the northern forests might be established approximately $8,000$ years sooner than observed; this discrepancy would lead to a significant error in predictions of the state of the land surface for that period. These errors would also translate into errors in the state of the terrestrial carbon cycle. The northward expansion of the forests may also have been limited by the melting of northern permafrost (Hoek (2001)).

To model seed dispersal realistically would require a substantial increase in model complexity. Seeds are dispersed by various mechanisms (see Howe and Westley (1997), p. 268), including wind dispersal. Moreover seed dispersal rates are dominated by extreme events (Clark *et al.* (1998)) making the task of modelling a realistic seed cycle even harder.

Direct simulation of seed redistribution is computationally expensive, and the mechanisms involved in dispersal are still being debated in the ecological literature (Clark *et al.* (1998)). Computational expense is especially problematic when simulations span thousands of years. A more simple option is made possible by assuming that seeds may be separated into 'heavy' and 'light' seed types. The light seeds are assumed to have a slow fall-out rate in the atmosphere, and are quickly redistributed within the atmosphere. This is proposed as a first attempt at moving away from the approach currently included in dynamic global vegetation models. Currently global vegetation models assume that vegetation seeding populations are either uniformly seeded, as is assumed in MOSES2, or that vegetation spatial distributions do not change dynamically (Clark *et al.* (1998)). PFTs with light seeds (*e.g.* the grass PFTs) could be assumed not to be limited by seed dispersal. Heavier seeds fall out of the atmosphere much more rapidly. As a first approximation it could be assumed that only grid boxes adjacent to a vegetated (by that particular heavy-seed PFT) grid box may become seeded for that PFT. This could be accomplished by introducing a mask array into the model. The mask array would have three pseudo-vertical levels, representing broadleaf tree PFT, needleleaf tree PFT, and perhaps shrub

PFT. Inclusion of shrub PFT is dependent on the actual definition of the shrub PFT, and the seed properties of the species included in this PFT. Inactive grid boxes (set to '0') are unable to re-grow the particular PFT, and the PFT coverage is held at near-zero coverage. The distribution of active cells in the mask is updated by considering the neighbouring grid box states (the quantity of source seeds) of each inactive grid box, and the local surface environment (the conditions for germination). Under prolonged extreme climate an active grid box may also become inactive. The division of seeds into 'heavy' and 'light' is an extreme form of the observation that seed size is inversely proportional to the dispersal distance (Roff and Fairbairn (2001)).

As it is formulated here the seed model assumes timescales for re-seeding an area. The time step for updating the mask array, and the rate at which a grid box becomes active when surrounding active grid boxes must be assumed. The seed dispersal model must include some general conditions required for the germination of seeds. By introducing this model a better representation of the land surface properties, and the terrestrial carbon cycle over the glacial-interglacial cycle may be achieved. Updating the active mask region as a function of the previous active region, introduces the potential for the unrealistic extinction of a PFT. This could be avoided by randomly activating a suitable (*i.e.* within specified climatic bounds) grid box at a prescribed rate. The approach of a mask and update rules makes use of concepts from spatial ecology which are commonly used to simulate spatial interactions (see Tilman and Kareiva (1997)).

6.3 Discussion

This thesis has used the HadSM3 climate model. This version of the Hadley Centre climate model uses a thermodynamic, slab model representation of the ocean. In HadSM3 the terrestrial carbon cycle is not coupled to the global carbon cycle either. Modelling the interactions of the terrestrial carbon cycle would require the ocean carbon cycle to be represented, which would in turn require ocean dynamics to be simulated (*i.e.* we would be using the HadCM3 model). This would substantially increase the computational expense involved in such long term simulations as this thesis suggests are required to study the behaviour of the terrestrial vegetation.

Understanding vegetation-atmosphere interactions motivates the inclusion of more processes. With increased model complexity there will always be an increase in the ability to constrain the models to what is expected, and it is reasonable to try to reduce the complexity of cycles to what are considered to be reasonable general principles (*e.g.* that vegetation cannot increase it's biomass indefinitely, or that that vegetation biomass is dependent on NPP). However it may be the case that ignoring certain systems or processes means that the climate model is too crude a representation to capture the behaviour of the real Earth system.

It is perhaps by simulating the global carbon cycle interactively that models of the terrestrial carbon cycle may best be validated. Testing the carbon cycle response to ENSO in HadCM3 allowed Jones *et al.* (2001) to validate interactions between climate and the carbon cycle component. Simulating the glacial-interglacial cycle in climate and CO_2 may also provide a good way to validate the climate models. The current trend in developing computationally cheap Earth system models of reduced complexity, will provide useful tools for exhaustive testing of global carbon cycle models.

If climate does have the potential to exist in more than one stable state then the behaviour of the climate system in states where climate is between stable states is crucial. An example of this is the study by Renssen *et al.* (2003b) which shows how global vegetation may play a crucial role in the stability of the climate system (see also Higgins *et al.* (2002)). The possibility that the climate is currently in one of these crucial states strengthens the importance of studying the behaviour of the land surface.

The results from this thesis highlight the importance of accurately predicting photosynthesis values. The inter-comparison study by Cramer *et al.* (2001) forced different global vegetation models with identical climate datasets, and observed the predicted NPP. This study shows that there is significant variation in the predicted NPP between global vegetation models (see chapter 1).

This thesis has shown the importance but also the complexity of the terrestrial carbon cycle. The underlying dynamics of the TRIFFID are based upon some of the most basic theoretic aspects of ecology (logistic growth and competition). The opportunity to develop and apply more complex and advanced ecological models is huge. Given our reliance on global vegetation biomass for most of our sustenance and the changes to the environment driven by anthropogenic emissions, the need for this research is equally large.

References

Andersen, K. and Ditlevsen, P. (1998). Glacial/interglacial variations of meridional transport and washout of dust: A one-dimensional model. *J.Geophys Res - Atmos*, **103**(D8), 8955–8962.

Archer, D., Winguth, A., Lea, D., and Mahowald, N. (2000). What caused the glacial/interglacial atmospheric pco_2 cycles? *Reviews of Geophysics*, **38**(2), 159–189.

Barkstrom, B., Harrison, E., Smith, G., Green, R., Kiber, J., and Cess, R. (1989). Earth radiation budget experiment (erbe) achival and april 1985 results. *Bull. Amer. Meteor. Soc.*, **70**, 1254–1264.

Beerling, D. (1999). New estimates of carbon transfer to terrestrial ecosystems between the last glacial maximum and the holocene. *Terra Nova*, **11**, 162–167.

Beerling, D. and Woodward, F. (2001). *Vegetation and the Terrestrial Carbon Cycle : modelling the first 400 million years*. Cambridge University Press.

Beerling, D., Woodward, F., Lomas, M., and Jenkins, A. (1997). Testing the responses of a dynamic global vegetation model to environmental change: a comparison of observations and predictions. *Global Ecology and Biogeography Letters*, **6**, 439–450.

Beerling, D., Osborne, C., and Chaloner, W. (2001). Evolution of leaf-form in land plants linked to atmospheric CO2 decline in the Late Palaeozoic era. *Nature*, **410**(6826), 352–354.

Berner, R. (1991). A model for atmospheric CO_2 over phanerozoic time. *American Journal of Science*, **291**(4), 339–376.

Berner, R. (1997). The rise of plants and their effect on weathering and atmospheric CO_2 . *Science*, **276**(5312), 544–546.

Berner, W., Oeschger, H., and Stauffer, B. (1980). Information on the CO_2 cycle from ice core studies. *Radiocarbon*, **22**, 227–235.

Berthouex, P. and Brown, L. (1994). *Statistics for Environmental Engineers*. Lewis Publishers, CRC Press, Inc., 2000 Corporate Blvd., N.W., Boca Raton, Florida 33431.

Betts, R. (1999). Self-beneficial effects of vegetation on climate in an Ocean-atmosphere general Circulation Model. *Geophys Res Lett*, **26**(10), 1457–1460.

Betts, R. (2000). Offset of the potential carbon sink from boreal forestation by decreases in surface albedo. *Nature*, **408**, 187–190.

Betts, R., Cox, P., Collins, M., Harris, P., Huntingford, C., and Jones, C. (2003). The role of ecosystem-atmosphere interactions in simulated amazonian precipitation decrease and forest

dieback under global climate warming. *submitted*.

Bonan, G., Pollard, D., and Thompson, S. (1992). Effects of boreal forest vegetation on global climate. *Nature*, **359**, 716–718.

Boyd, P., Watson, A., Law, C., Abraham, E., Trull, T., Murdoch, R., Bakker, D., Bowie, A., Buesseler, K., Chang, H., Charette, M., Croot, P., Downing, K., Frew, R., Gall, M., Hadfield, M., Hall, J., Marvey, M., Jameson, G., LaRoche, J., Liddicoat, M., Ling, R., Maldonado, M., McKay, R., Nodder, S., Pickmere, S., Pridmore, R., Rintoul, S., Safi, K., Sutton, P., Strzepek, R., Tanneberger, K., Turnerm, S., Waite, A., and Zeldis, J. (2000). A mesoscale phytoplankton bloom in the polar southern ocean stimulated by iron fertilization. *Nature*, **407**, 695–702.

Braconnot, P., Joussaume, S., Marti, O., and de Noblet, N. (1999). Synergistic feedbacks from ocean and vegetation on the African monsoon response to mid-Holocene insolation. *Geophys Res Lett*, **26**(16), 2481–2484.

Brovkin, V., Ganopolski, A., and Svirezhev, Y. (1997). A continuous climate-vegetation classification for use in climate-biosphere studies. *Ecological Modelling*, **101**, 251–261.

Brovkin, V., Claussen, M., Petoukhov, V., and Ganopolski, A. (1998). On the stability of the atmosphere-vegetation system in the Sahara/Sahel region. *J.Geophys Res - Atmos*, **103**(D24), 31,613–31,624.

Brovkin, V., Levis, S., Loutre, M., Crucifix, M., Claussen, M., Ganopolski, A., Kubatzki, C., and Petoukhov, V. (2003). Stability analysis of the climate-vegetation system in the northern high latitudes. *Clim. Change*, **57**, 119–138.

Cao, M. and Woodward, F. (1998). Dynamic responses of terrestrial ecosystem carbon cycling to global climate change. *Nature*, **393**, 249–252.

Case, T. (2000). *An illustrated guide to theoretical ecology*. Oxford University Press, Oxford, UK.

Cattle, H. and Crossley, J. (1995). Modelling arctic climate change. *Phil. Trans. R. Soc. Lond. A*, **352**, 201–213.

Cerling, T., Ehleringer, J., and Harris, J. (1998). Carbon dioxide starvation, the development of C4 ecosystems, and mammalian evolution. *Phil. Trans. R. Soc. Lond. B*, **353**, 159–171.

Charney, J. (1975). Dynamics of deserts and drought in the sahel. *Q. J. R. Meteorol. Soc.*, **101**(428), 193–202.

Charney, J., Stone, P., and Quirk, W. (1975). Drought in the Sahara: A biogeophysical feedback

mechanism. *Science*, **187**, 434–435.

Clark, J., Fastie, C., Hurtt, G., Jackson, S., Johnson, C., King, G., Lewis, M., Lynch, J., Pacala, S., Prentice, C., Schupp, E., Webb III, T., and Wyckoff, P. (1998). Reid's paradox of rapid plant migration. *Bioscience*, **48**(1), 13–24.

Claussen, M. (2001). *Global Biogeochemical cycles in the climate system*, chapter 5: Biogeophysical Feedbacks and the Dynamics of Climate. Academic Press, San Diego. Schulze, E., Heimann, M., Harrison, S., Holland, E., Lloyd, J., Prentice, I., and Schimel, D. (eds), pp. 416.

Claussen, M. and Gayler, V. (1997). The greening of the Sahara during the mid-Holocene: results from an interactive atmosphere-biome model. *Global Ecology and Biogeography Letters*, **6**, 369–377.

Claussen, M., Kubatzki, C., Brovkin, V., and Ganopolski, A. (1999). Simulation of an abrupt change in Saharan vegetation in the mid-Holocene. *Geophys Res Lett*, **26**(14), 2037–2040.

Claussen, M., Mysak, L., Weaver, A., Crucifix, M., Fichefet, T., Loutre, M., Weber, S., Alcamo, J., Alexeev, V., Berger, A., Calov, R., Ganopolski, A., Goosse, H., Lohmann, G., Lunkeit, F., Mokhov, I., Petoukhov, V., Stone, P., and Wang, Z. (2002). Earth system models of intermediate complexity: closing the gap in the spectrum of climate system models. *Climate Dynamics*, **18**, 579–586.

Claussen, M., Brovkin, V., Ganopolski, A., Kubatzki, C., and Petoukhov, V. (2003). Climate change in Northern Africa: the past is not the future. *Clim. Change*, **57**, 99–118.

Collatz, G., Ball, J., Grivet, C., and Berry, J. (1991). Physiological and environmental regulation of stomatal conductance, photosynthesis and transpiration: a model that includes a laminar boundary layer. *Agricultural and Forest Meteorology*, **54**, 107–136.

Collatz, G., Ribas-Carbo, M., and Berry, J. (1992). Coupled photosynthesis-stomatal conductance model for leaves of c4 plants. *Aust. J. Plant Phsiol.*, **19**, 519–538.

Collins, M., Tett, S., and Cooper, C. (2000). The internal climate variability of HadCM3, a version of the Hadley Centre coupled model without flux adjustments. *Climate Dynamics*, **17**(1), 61–81.

Cox, C. and Moore, P. (1999). *Biogeography : an ecological and evolutionary approach*. Blackwell Science, UK, 6th edition. pp. 312.

Cox, M. (1984). A primative equation, 3 dimensional model of the ocean. GDFL Ocean Group Technical Rep 1. Technical report, Princeton, NJ, USA, 143 pp.

Cox, P. (2001). Description on the TRIFFID Dynamic Global Vegetation Model. Technical Report 24, Hadley Centre, Met Office. Available from www.metoffice.com/research/hadleycentre/pubs/HCTN/index.html.

Cox, P., Huntingford, C., and Harding, R. (1998). A canopy conductance and photosynthesis model for use in a GCM land surface scheme. *Journal of Hydrology*, **213**, 79–94.

Cox, P., Betts, R., Bunton, C., Essery, R., Rowntree, P., and Smith, J. (1999). The impact of new land surface physics on the GCM simulation of climate and climate sensitivity. *Climate Dynamics*, **15**, 183–203.

Cox, P., Betts, R., Jones, C., Spall, S., and Totterdell, I. (2000). Acceleration of global warming due to carbon-cycle feedbacks in a coupled model. *Nature*, **408**, 184–187.

Cox, P., Betts, R., Jones, C., Spall, S., and Totterdell, I. (2001). *Meteorology at the Millennium*, volume 83 of *International Geophysics Series.*, chapter 21: Modelling Vegetation and the Carbon Cycle as Interactive Elements of the Climate system. Academic Press, UK. pp 259-279.

Cramer, W., Bondeau, A., Woodward, F., Prentice, I., Betts, R., Brivkin, V., Cox, P., Fisher, V., Foley, J., Friend, A., Kucharik, C., Smith, B., White, A., and Young-Molling, C. (2001). Global response of terrestrial ecosystem structure and function to CO_2 and climate change: results from six dynamic global vegetation models. *Global Change Biology*, **7**(4), 357–373.

Delcourt, H., Delcourt, P., and Web III, T. (1983). Dynamic plant ecology: The spectrum of vegetation change in space and time. *Quarterly Science Reviews*, **1**, 153–175.

deMenocal, P., Ortiz, J., Guilderson, T., Adkins, J., Sarnthein, M., Baker, L., and Yarusinsky, M. (2000). Abrupt onset and termination of the African Humid period: rapid cliamate responses to gradual insolation forcing. *Quaternary Science Reviews*, **19**, 347–361.

Dickinson, R., Berry, J., Bonan, G., Collatz, G., Field, C., Fung, I., Goulden, M., Hoffmann, W., Jackson, R., Myneni, R., Sellers, P., and Shaikh, M. (2002). Nitrogen controls on climate model evapotranspiration. *J.Climate*, **15**, 278–295.

Edwards, J. and Slingo, A. (1996). Studies with a flexible new radiation code. i: Choosing a configuration for a large-scale model. *Q. J. R. Meteorol. Soc.*, **122**, 689–719.

Ehleringer, J. and Cerling, T. (2001). *Global Biogeochemical Cycles in the Climate System.*, chapter 12: Photosynthetic Pathways and Climate. Academic Press. Schulze, E., Heimann, M., Harrison, S., Holland, E., Lloyd, J., Prentice, I.C., and Schimel, D. (eds).

Essery, R., Best, M., and Cox, P. (2001). Moses 2.2 technical doc-

umentation. Technical Report 30, Hadley Centre. Available from www.metoffice.com/research/hadleycentre/pubs/HCTN/index.html.

Farquhar, G., von Caemmerer, S., and Berry, J. (1980). A Biochemical Model of Photosynthetic CO_2 Assimilation in Leaves of C3 species. *Planta*, **149**, 78–90.

Fensham, R. and Fairfax, R. (2002). Aerial photography for assessing vegetation change: a review of applications and the relevance of findings for Australian vegetation history. *Aust. J. Bot.*, **50**(4), 415–429.

Foley, J., Kutzbach, J., Coe, M., and Levis, S. (1994). Feedbacks between climate and boreal forests during the Holocene epoch. *Nature*, **371**, 52–54.

Foley, J., Prentice, I., Ramankutty, N., Levis, S., Pollard, D., Sitch, S., and Haxeltine, A. (1996). An integrated biosphere model of land surface processes, terrestrial carbon balance and vegetation dynamics. *Global Biogeochemical cycles*.

Friend, A., Stevens, A., Knox, R., and Cannell, M. (1997). A process-based, terrestrial biosphere model of ecosystem dynamics (hybrid v3.0). *Ecological Modelling*, **95**, 249–287.

Gallimore, R. and Kutzbach, J. (1996). Role of orbitally induced changes in tundra area in the onset of glaciation. *Nature*, **381**, 503–505.

Gates, W., Boyle, J., Covey, C., Dease, C., Doutriaux, C., Drach, R., Fiorino, M., Gleckler, P., Hnilo, J., Marlais, S., Phillips, T., Potterm, G., Santer, B., Sperber, K., Taylor, K., and Williams, D. (1999). An overview of the results of the Atmospheric Model Intercomparison Project (AMIP 1). *Bull. Amer. Meteor. Soc.*, **80**(1), 29–55.

Giardina, C. and Ryan, M. (2000). Evidence that decomposition rates of organic carbon in mineral soil do not vary with temperature. *Nature*, **404**, 858–861.

Gitay, H. and Noble, I. (1997). *Plant functional types : their relevance to ecosystem properties and global change*, chapter 1: What are functional types and how should we seek them? Cambridge University Press. Smith T., Shugart H., and Woodward F. (eds), pp. 383.

Gordon, C., Cooper, C., Seniour, C., Banks, H., Gregory, J., Johns, T., Mitchell, J., and Wood, R. (2000). The simulation of SST, sea ice extents and ocean heat transports in a version of the Hadley Centre coupled model without flux adjustments. *Climate Dynamics*, **16**, 147–168.

Gotelli, N. (1998). *A primer of Ecology*. Sinauer Associates, Inc. Publishers, Sunderland, Massachusetts, 2nd edition. pp. 200.

Grace, J. and Rayment, M. (2000). Respiration in the balance. *Nature*, **404**, 819–820.

Graham, N. and Barnett, T. (1987). Sea surface temperature, surface wind divergence, and convection over tropical oceans. *Science*, **238**, 657–659.

Gregory, D. and Rowntree, P. (1990). A mass flux convection scheme with representation of cloud ensemble characteristics and stability-dependant closure. *Am. Met. Soc.*, **118**, 1483–1506.

Gregory, D., Kershaw, R., and Inness, P. (1997). Parametrization of momentum by convection. ii: Tests in single-column and general circulation models. *Q. J. R. Meteorol. Soc.*, **123**, 1153–1183.

Hall, D. and Rao, K. (1994). *Photosynthesis*. Cambridge University Press, Cambridge, UK., 5th edition. pp. 228.

Harding, R., Huntingford, C., and Cox, P. (2000). Modelling long-term transpiration measurments from grassland in southern England. *Agricultural and Forest Meteorology*, **100**, 309–322.

Harris, P., Huntingford, C., Gash, J., Hodnett, M., Cox, P., Malhi, Y., and Araujo, A. (2003). Calibration of a land-surface model using data from primary forest sites in Amazonia. *Theoretical and Applied Climatology*. submitted.

Harrison, S., Kohfeld, K., Roelands, C., and Claquin, T. (2001). The role of dust in climate changes today, at the last glacial maximum and in the future. *Earth-Science Rev.*, **54**(1-3), 43–80.

Hartmann, D. (1994). *Global Physical Climatology.* Number 56 in International Geophysics Series. Academic Press, San Diego. pp. 397.

Henderson-Sellers, A. (1993). Continental vegetation as a dynamic component of a global climate model: a preliminary assessment. *Clim. Change*, **23**, 337–377.

Hewitt, C., Stouffer, R., Broccoli, A., Mitchell, J., and Valdes, P. (2003). The effect of ocean dynamics in a coupled GCM simulation of the Last Glacial Maximum. *Climate Dynamics*, **20**, 203–218.

Higgins, P., Mastrandrea, M., and Schneider, S. (2002). Dynamics of climate and ecosystem coupling: abrupt changes and multiple equilibria. *Phil. Trans. R. Soc. Lond. B*, **357**, 647–655.

Hoek, W. (2001). Vegetation response to the $\sim$ 14.7 and $\sim$ 11.5 ka cal. bp climate transitions: is vegetation lagging climate? *Global and Planetary Change*, **30**, 103–115.

Holdridge, L. (1947). Determination of world plant formations from simple climatic data. *Science*, pages 367–368.

Howe, H. and Westley, L. (1997). *Plant Ecology*, chapter 9: Ecology of pollination and seed dispersal. Blackwell Science, 25 John Street, London WC1N 2BL, 2nd edition. Crawley M.J. (ed), pp. 512.

Huntingford, C., Cox, P., and Lenton, T. (2000). Contrasting responses of a simple ecosystem model to global change. *Ecological Modelling*, **134**, 41–58.

Indermuhle, A., Stocker, T., Joos, F., Fischer, H., Smith, H., Wahlen, M., Deck, B., Mastroianni, D., Tschumi, J., Blunier, T., Meyer, R., and Stauffer, B. (1999). Holocene carbon-cycle dynamics based on CO_2 trapped in ice at Taylor Dome, Antarctica. *Nature*, **398**, 121–126.

Jolly, D., Prentice, I., Bonnefille, R. amd Ballouche, A., Bengo, M., Brenac, P., Buchet, G., Burney, D., Cazet, J., Cheddadi, R., Edorh, T., Elenga, H., Elmoutaki, S., Guiot, J., Laarif, F., Lamb, H., Lezine, A., Maley, J., Mbenza, M., Peyron, O., Reille, M., Reynaud-Farrera, I., Riollet, G., Ritchie, J., Roche, E., Scott, L., Semmanda, I., Straka, H., Umer, M., Campo, E., Vilimumbalo, S., Vincens, A., and Waller, M. (1998). Biome reconstruction from pollen and plant macrofossil data for African and the Arabian peninsula at 0 and 6000 years. *J.Biogeography*, **25**, 1007–1027.

Jones, C. and Cox, P. (2001a). Constraints on the temperature sensitivity of global soil respiration from the observed interannual variability in atmospheric CO_2 . *Atm. Sci. Lett.* doi:10.1006/asle.2000.0041.

Jones, C. and Cox, P. (2001b). Modelling the Volcanic signal in the Atmospheric CO_2 record. *Global Biogeochemical cycles*, **15**(2), 453–465.

Jones, C., Collins, M., Cox, P., and Spall, S. (2001). The carbon cycle response to ENSO: A coupled climate-carbon model study. *J.Climate*, **14**(21), 4113.

Jones, C., Cox, P., Essery, R., Roberts, D., and Woodage, M. (2003). Strong carbon cycle feedbacks in a climate model with interactive CO_2 and sulphate aerosols. *Geophys Res Lett*, **30**(9). 1479, doi:10.1029/2003GL016867.

Jones, P. (1994). Hemispheric surface air temperature variations: a reanalysis and an update to 1993. *J.Climate*, **7**(11), 1794–1802.

Jones, T. (2002). Reply ”Extraterrestrial impacts and wildfires”. *Palaeogeogr. Palaeoclimatol. Palaeoecol.*, **185**(3-4), 407–408.

Joussaume, S., Taylor, K., Braconnot, P., Mitchell, J., Kutzbach, J., Harrison, S., Prentice, I., Broccoli, A., Abe-Ouchi, A., Bartlein, P., Bonfils, C., Dong, B., Guiot, J., Herterich, K., He-

witt, C., Jolly, D., Kim, J., Kislov, A., Kitoh, A., Loutre, M., Masson, V., McAvaney, B., McFarlane, N., de Noblet, N., Peltier, W., Peterschmitt, J., Pollard, D., Rind, D., Royer, J., Schlesinger, M., Syktus, J., Thompson, S., Valdes, P., Vettoretti, G., Webb, R., and Wyputta, U. (1999). Monsoon changes for 6000 years ago: Results of 18 simulations from the Paleoclimate Modelling Intercomparison Project (PMIP). *Geophys Res Lett*, **26**(7), 859–862.

Kadmon, R. and Harari-Kremer, R. (1999). Studying long-term vegetation dynamics using digital processing of historical aerial photographs. *Remote Sensing of Environment*, **68**(2), 164–176.

Keeling, C., Whorf, T., Wahlen, M., and van der Plicht, J. (1995). Interannual extremes in the rate of rise of atmospheric carbon dioxide since 1980. *Nature*, **375**, 666–670.

Kennett, J., Cannariato, K., Hendy, I., and Behl, R. (2002). *Methane Hydrates in Quaternary Climate Change : the Clathrate Gun Hypothesis*. American Geophysical Union, Washington DC. pp. 216.

Khalil, H. (1996). *Nonlinear Systems*. Prentice Hall, Upper Saddle River, 2nd edition. pp. 557.

Killham, K. (1994). *Soil Ecology*. Cambridge University Press. pp. 260.

Kleidon, A., Fraedrich, K., and Heimann, M. (2000). A green planet versus a desert world: Estimating the maximum effect of vegetation on the land surface climate. *Climatic Change*, **44**, 471–493.

Krebs, C. (2001). *Ecology*. Benjamin Cummings, California, USA, 5th edition.

Kucharik, C., Foley, J., Delire, C., Fisher, V., Coe, M., Lenters, J., Young-Molling, C., and Ramankutty, N. (2000). Testing the performance of a dynamic global ecosystem model: water balance, carbon balance, and vegetation structure. *Global Biogeochemical Cycles*, **14**(3), 795–825.

Kuhlbusch, T. (1998). Black carbon and the carbon cycle. *Science*, **280**, 1903–1904.

Kump, L., Kasting, J., and Crane, R. (1999). *The Earth System*. Prentice Hall.

Kutzbach, J., Bonan, G.and Foley, J., and Harrison, S. (1996). Vegetation and soil feedbacks on the response of the African monsoon to orbital forcing in the early to middle Holocene. *Nature*, **384**, 623–626.

Lasaga, A. and Berner, R. (1998). Fundemental aspects of quantitative models for geochemical cycles. *Chemical Geology*, **145**, 161–175.

Legates, D. and Willmott, C. (1990). Mean seasonal and spatial variability in global surface air temperature. *Theoret Appl Climatol*, **41**, 11–21.

Lenton, T. and Betts, R. (1998). *From Urban Air Pollution to Extra-Solar Planets*, volume ERCA Volume 3, chapter : From Daisyworld to GCMs: Using models to understand the regulation of climate, pages 145–167. EDP Sciences, Les Ulis, France. Boutron, C.F. (ed).

Lenton, T. and Lovelock, J. (2001). Daisyworld revisited: quantifying biological effects on planetary self-regulation. *Tellus*, **53B**, 288–305.

Lenton, T. and Wilkinson, D. (2003). Developing the Gaia theory. *Clim. Change*, **58**, 1–12.

LeTreut, H. and McAvaney, B. (2000). A model intercomparison of equilibrium climate change in response to CO_2 doubling. Technical Report Note du Pole de Modelisation de l'IPSL, Number 18, Institut Pierre Simon LaPlace, Paris, France. Available for download from www.ipsl.jussieu.fr/poles/Modelisation/NotesSciences.htm.

Lieth, H. (1978). *Primary Productivity of the Biosphere*, chapter 12 : Modeling the primary productivity of the world. Springer-Verlang. Lieth, H. and Whittaker, R.H., (Eds).

Loveland, T., Reed, B., Brown, J., Ohlen, D., Zhu, Z., Yang, L., and Merchant, J. (2000). Development of a global land cover characteristics database and IGBP DISCover from 1 km AVHRR data. *International j. Remote Sensing*, **21**(6-7), 1303–1330.

Mahowald, N., Kohfeld, K., Hansson, M., Balkanski, Y., Harrison, S., Prentice, I., Schulz, M., and Rodhe, H. (1999). Dust sources and deposition during the last glacial maximum and current climate: A comparison of model results with paleodata from ice cores and marine sediments. *J.Geophys Res - Atmos*, **104**(D13), 15,895–15,916.

Malamud, B., Morein, G., and Turcotte, D. (1998). Forest fires: An example of self-organized critical behaviour. *Science*, **281**, 1840–1842.

Manabe, S. and Stouffer, R. (1988). Two stable equilibria of a coupled ocean-atmosphere model. *J.Climate*, **1**, 841–866.

Manabe, S., Stouffer, R., Spelman, M., and Bryan, K. (1991). Transient Responses of a Coupled Ocean-Atmosphere Model to Gradual Changes of Atmospheric CO_2. Part I: Annual Mean Response. *J.Climate*, **4**(8), 785–818.

Martin, J. (1990). Glacial-Interglacial CO_2 change: the Iron Hypothesis. *Paleoceanography*, **5**(1), 1–13.

Mason, P. (1988). The formation of areally-averaged roughness lengths. *Q. J. R. Meteorol. Soc.*, **114**, 399–420.

May, R. (1976). Simple mathematical models with very complicated dynamics. *Nature*,

261(5560), 459–467.

McElwain, J. (1998). Do fossil plants signal palaeoatmospheric CO_2 concentration in the geological past? *Phil. Trans. R. Soc. Lond. B*, **353**, 83–96.

McGuffie, K. and Henderson-Sellers, A. (1997). *A Climate Modelling Primer*. Wiley, 2nd edition. pp. 268.

Meehl, G. (1992). *Climate System Modelling*, chapter 17: Global coupled models. Cambridge University Press. Trenberth, K.E. (ed).

Mitchell, J. and Karoly, D. (2001). *Detection of Climate Change and Attribution of Causes In:Climate Change 2001: The Scientific Basis*. Cambridge University Press, Cambridge.

Monteith, J. and Unsworth, M. (1990). *Principles of Environmental Physics*. Arnold, 338 Euston Road, London NW1 3BH, UK., 2nd edition.

Mooney, H. and Ehleringer, J. (1997). *Plant Ecology*, chapter 1: Photosynthesis. Blackwell Science, 2nd edition. Crawley, M.J. (ed).

Nevison, C., Gupta, V., and Klinger, L. (1999). Self-sustained temperature oscillations on daisyworld. *Tellus*, **51B**, 806–814.

Nisbet, E. (2002). Have sudden large releases of methane from geological reservoirs occured since the last glacial maximum, and could such releases occur again? *Phil. Trans. R. Soc. Lond. A*, **360**(1793), 581–607.

Oke, T. (1987). *Boundary Layer Climates*. Routledge, 2nd edition.

Osborne, T., Lawrence, D., Slingo, J., Challinor, A., and Wheeler, T. (2003). Influence of vegetation on the local climate and hydrology in the Tropics: Sensitivity to soil parameters. *Submitted*.

Page, S. *et al.* (2002). The amount of carbon released from peat and forest fires in Indonesia during 1997. *Nature*, **420**, 61–65.

Palmer, J. and Totterdell, I. (2001). Production and export in a global ocean ecosystem model. *Deep-Sea Res.*, **48**, 1169–1198.

Parker, D., Folland, C., and Jackson, M. (1995). Marine surface temperature: observed variations and data requirements. *Clim. Change*, **31**, 559–600.

Peixoto, J. and Oort, A. (1992). *Physics of Climate*. American Institute of Physics, New York. pp. 520.

Petit, J., Jouzel, J., Raynaud, D., Barkov, N., Barnola, J., Basile, I., Bender, M., Chappellaz, J.,

Davis, M., Delaygue, G., Delmotte, M., Kotlyakov, V., Legrand, M., Lipenkov, V., Lorius, C., Pepin, L., Titz, C., Saltzman, E., and Stievenard, M. (1999). Climate and atmospheric history of the past 420,000 years from the Vostok ice core, Antarctica. *Nature*, **399**(6735), 429–436.

Petoukhov, V., Ganopolski, A., Brovkin, V., Claussen, M., Eliseev, A., Kubatzki, C., and Rahmstorf, S. (2000). CLIMBER-2: a climate system model of intermediate complexity. Part1: model description and performace for present climate. *Climate Dynamics*, **16**, 1–17.

Pope, V. and Stratton, R. (2002). The processes governing horizontal resolution sensitivity in a climate model. *Climate Dynamics*, **19**, 211–236.

Pope, V., Galani, M., Rowntree, P., and Stratton, R. (2000). The impact of new physical parametrizations in the Hadley Centre climate model: HadAM3. *Climate Dynamics*, **16**, 123–146.

Prentice, I. (2001). *The Carbon Cycle and Atmospheric Carbon Dioxide. In:Climate Change 2001: The Scientific Basis*. Cambridge University Press, Cambridge. Houghton, J.T., Ding, Y., Griggs, D.J., Noguer, M., van der Linden, P.J., Dai, X., Maskell, K., and Johnson, C.A. (eds).

Prentice, I., Cramer, W., Harrison, S., Leemans, R., Monserud, R., and Solomon, A. (1992). A global biome model based on plant physiology and dominance, soil properties and climate. *J.Biogeography*, **19**, 117–134.

Price, M. (1996). *Introducing Groundwater*. Chapman & Hall, 2-6 Boundary Row, London SE1 8HN, UK, 2nd edition.

Quinlan, A., Dale, M., and Gates, C. (2003). Effects of prescribed burning on herbaceous and woody vegetation in northern lowland meadows. *Restoration Ecology*, **11**(3), 343–350.

Ramaswamy, V., Boucher, O., Haigh, J., Hauglustaine, D., Haywood, J., Myhre, G., Nakajima, T., Shi, G., and Solomon, S. (2001). *Radiative forcing of Climate Change. In:Climate Change 2001: The Scientific Basis*. Cambridge University Press, Cambridge. Houghton, J.T. et. al. (eds).

Renssen, H., Brovkin, V. Fichefet, T., and Goose, H. (2003a). Holocene climate instability during the termination of the African Humid Period. *Geophys Res Lett*, **30**(4), 1184,doi:10.1029/2002GL016636.

Renssen, H., Goose, H., and Fichefet, T. (2003b). On the non-linear response of the ocean thermohaline circulation to global deforestation. *Geophys Res Lett*, **30**(2), 1060,doi:10.1029/2002GL016155.

Ricklefs, R. (1997). *The Economy of Nature.* W.H. Freeman and Company, New York, US., fourth edition.

Ridgwell, A. (2002). Dust in the earth system: The biogeochemical linking of land, air, and sea. *Phil. Trans. R. Soc. Lond. A*, **360**, 2905–2924.

Ridgwell, A. (2003). An earth system view of the 'iron hypothesis'. *submitted*.

Roff, D. and Fairbairn, D. (2001). *Dispersal*, chapter 13 : the Genetic basis of dispersal and migration, and its consequences for the evolution of correlated traits, page pp. 452. Oxford University Press. Clobert, J., Danchin, E., Dhondt, A., and Nichols, J. (eds).

Royer, J. (2000). *Numerical Modelling of the Global Atmosphere in the Climate System*, chapter 2: The GCM as a dynamical system. NATO Science Series. Kluwer Academic Publishers, The Netherlands. Mote, P.W. and O'Neill, A. (eds).

Sabins, F. (1996). *Remote Sensing : principles and interpretation*. W.H. Freeman and Company, 3rd edition. pp. 432.

Schellnhuber, H. (1999). 'Earth system' analysis and the second Copernican revolution. *Nature*, **402**, C19–C23.

Schmidt, M. and Noack, A. (2000). Black carbon in soils and sediments: Analysis, distribution, implications, and current challenges. *Global Biogeochemical cycles*, **14**(3), 777–793.

Schneider, S. (1992). *Climate system modelling*, chapter 1: Introduction to climate modelling. Cambridge University Press, Cambridge, UK. Trenberth, K.E. (ed).

Sellers, P., Dickinson, R., Randall, D., Betts, A., Hall, F., Berry, J., Collatz, G., Denning, A., Mooney, H., Nobre, C., Sato, N., Field, C., and Henderson-Sellers, A. (1997). Modelling the exchanges of energy, water, and carbon between continents and the atmosphere. *Science*, **275**, 502–509.

Sitch, S. (2000). *The role of vegetation dynamics in the control of atmopheric CO_2 content*. Ph.D. thesis, Lund University.

Sitch, S., Smith, B., Prentice, I., Arneth, A., Bondeau, A., Cramer, W., Kaplan, J., Levis, S., Lucht, W., Sykes, M., Thonicke, K., and Venevsky, S. (2003). Evaluation of ecosystem dynamics, plant geography and terrestrial carbon cycling in the LPJ dynamic global vegetation model. *Global Change Biology*, **9**, 161–185.

Smith, R. (1993). Unified model documentation paper 24 : subsurface, surface and boundary layer processes. Technical report, Met. Office, UK.

Smith, T., Shugart, H., and Woodward, F., editors (1997). *Plant functional types : their relevance to ecosystem properties and global change.* International Geosphere-Biosphere programme book series. Cambridge University Press.

Stocker, T., Clarke, G., Le Treut, H., Lindzen, R., Meleshko, V., Mugara, R., Palmer, T., Pierrehumbert, R., Sellers, P., Trenberth, K., and Willebrand, J. (2001). *Physical Climate Processes and Feedbacks. In:Climate Change 2001: The Scientific Basis*. Cambridge University Press, Cambridge. Houghton, J., Ding, Y., Griggs, D., Noguer, M., van der Linden, P., Dai, X., Maskell, K., and Johnson, C. (eds).

Stommel, H. (1961). Thermohaline convection with two stable regimes of flow. *Tellus*, **13**(2), 224–230.

Street-Perrott, F., Holmes, J., Waller, M., Allen, M., Barber, N., Fothergill, P., Harkness, D., Ivanovich, M., Kroon, D., and Perrott, R. (2000). Drought and dust deposition in the West African Sahel: a 5500-year record from Kajemarum Oasis, northeastern Nigeria. *The Holocene*, **10**(3), 293–302.

Svetsov, V. (2002). Comment on "extraterrestrial impacts and wildfires". *Palaeogeogr. Palaeoclimatol. Palaeoecol.*, **185**(3-4), 403–405.

Svirezhev, Y. (2000). Lotka-volterra models and the global vegetation pattern. *Ecological Modelling*, **135**, 135–146.

Thomson, W. (1993). *Theory of Vibration with Applications*. Nelson Thornes Ltd, Cheltenham, UK., 5th edition. pp. 560.

Thonicke, K., Venevsky, S., Sitch, S., and Cramer, W. (2001). The role of fire disturbance for global vegetation dynamics : coupling fire into a dynamic global vegetation model. *Global Ecology and Biogeography*, **10**(6), 661–677.

Tilman, D. and Kareiva, P., editors (1997). *Spatial Ecology*. Monographs in Population Biology 30. Princeton University Press. pp. 382.

Turnpenny, J., Crossley, J., Hulme, M., and Osborn, T. (2002). Air flow influences on local climate: comparison of a regional model with observations over the United Kingdom. *Climate Research*, **20**(3), 189–202.

van Gardingen, P., Foody, G., and Curran, P., editors (1997). *Scaling-up : from cell to landscape*. Cambridge University Press. pp. 400.

Van Minnen, J., Leemans, R., and Ihle, F. (2000). Defining the importance of including transient

ecosystem responses to simulate C-cycle dynamics in a global change model. *Global Change Biology*, **6**, 595–611.

Vasilyev, N. (1998). The tunguska meteorite problem today. *Planetary and Space Science*, **46**(2-3), 129–150.

Visbeck, M., Marshall, J., Haine, T., and Spall, M. (1997). On the specification of eddy transfer coefficients in coarse resolution ocean circulation models. *J Phys Oceanogr*, **27**, 381–402.

Vonder Haar, T. and Kidder, S. (1995). *Satellite Meteorology : an introduction*. Academic Press. pp. 506.

Watson, A. and Lovelock, J. (1983). Biological homeostasis of the global environment: the parable of Daisyworld. *Tellus*, **35B**(4), 284–289.

Watson, A., Bakker, D., Ridgwell, A., Boyd, P., and Law, C. (2000). Effect of iron supply on southern ocean CO_2 uptake and implications for glacial atmospheric CO_2 . *Nature*, **407**, 730–733.

White, A., Cannell, M., and Friend, A. (1999). Climate change impacts on ecosystems and the terrestrial carbon sink: a new assessment. *Global Environmental Change-Human and Policy Dimensions*, **9**, S21–S30.

Williams, K., Keen, A., Crossley, J., Seniour, C., and Hewitt, C. (1999). Unified model documentation paper 58 : the slab model. Technical report, Met. Office, UK.

Williams, K., Senior, C., and Mitchell, J. (2001). Transient Climate Change in the Hadley Centre Models: The role of Physical Processes. *J.Climate*, **14**, 2659–2674.

Wilson, M. and Henderson-Sellers, A. (1985). A global archive of land cover and soils data for use in general circulation climate models. *J.Climatology*, **5**, 119–143.

Woodward, F. (1987). *Climate and Plant Distribution*. Cambridge University Press, cambridge, UK. pp. 190.

Woodward, F. and Beerling, D. (1997). The dynamics of vegetation change: health warnings for equilibrium 'dodo' models. *Global Ecology and Biogeography Letters*, **6**, 413–418.

Woodward, F. and Cramer, W. (1996). Plant functional types and climatic changes: Introduction. *Journal of Vegetation Science*, **7**(3), 306–308.

Woodward, F. and Diament, A. (1991). Functional approaches to predicting ecological effects of global change. *Functional Ecology*, **5**, 202–212.

Woodward, F., Lomas, M., and Betts, R. (1998). Vegetation-climate feedbacks in a greenhouse

world. *Phil. Trans. R. Soc. Lond. B*, **353**, 29–39.

Xue, Y. and Shukla, J. (1993). The influence of land surface properties on Sahel climate. part i: desertification. *J.Climate*, **6**, 2232–2245.

Zeng, N., Dickinson, R., and Zeng, X. (1996). Climatic impact of Amazon deforestation - a mechanistic model study. *J.Climate*, **9**, 859–883.

Zheng, X. and Eltahir, E. (1998). The role of vegetation in the dynamics of west African monsoons. *J.Climate*, **11**, 2078–2096.